AGH University of Science and Technology
Faculty of Physics and Applied Computer Science

Doctoral thesis

Grzegorz Gach

Measurement of Exclusive Diffractive Dijet Production in Deep Inelastic Scattering at ZEUS Experiment.

Supervisors: **prof. dr hab. Danuta Kisielewska**
dr inż. Leszek Adamczyk

Cracow, 2013

Declaration of the author of this dissertation:

Aware of legal responsibility for making untrue statements I hereby declare that I have written this dissertation myself and all the contents of the dissertation have been obtained by legal means.

Declaration of the thesis Supervisor:

This dissertation is ready to be reviewed.

$\mathcal{T}o \quad \sim$

Streszczenie

Ta rozprawa doktorska przedstawia badania nad ekskluzywną dyfrakcyjną produkcją par dżetów w głęboko nieelastycznym rozpraszaniu lepton-proton. Dane wykorzystane w analizie zostały zgromadzone przez eksperyment ZEUS.

Kształt rozkładu kąta azymutalnego dżetów w układzie środka masy wirtualnego fotonu i pomeronu, pozwala stwierdzić w wyniku działania jakiego mechanizmu powstały dżety. W przypadku fuzji fotonowo-gluonowej (wymiana pojedynczego gluonu) rozkład jest wklęsły w przedziale $(0, \pi)$, a w wyniku wymiany dwóch gluonów rozkład jest wypukły. Określenie mechanizmu produkcji dżetów zweryfikuje część modeli teoretycznych opisujących dyfrakcję oraz pozwoli określić naturę cząstki pośredniczącej w oddziaływaniu. Procesy zachodzące w obszarze małych wartości x, do których zalicza się dyfrakcja, charakteryzują się tym, że parton biorący udział w oddziaływaniu unosi tylko mały fragment pędu protonu. Takie oddziaływania łączą w sobie procesy opisywalne przy pomocy rachunku zaburzeń z tymi, które opisywane są tylko modelami fenomenologicznymi. Badania nad tego typu procesami pozwalają lepiej zrozumieć w którym miejscu rachunek zaburzeń załamuje się oraz w jaki sposób można ekstrapolować modele do nieperturbacyjnego regionu.

Dane poddane analizie pochodzą ze zderzeń elektronów(pozytonów) z protonami, których energia w układzie środka masy wynosiła $\sqrt{s} = 318$ GeV. Leptony i protony były rozpędzane przez akcelerator HERA, po jego przebudowie w latach 2000–2002. Akcelerator działał od 2003 do 2007 roku. W tym czasie detektor ZEUS zarejestrował dane o całkowitej świetlności wynoszącej około 350 pb^{-1}. Analiza przedstawiona w tej rozprawie została wykonana w następującym obszarze kinematycznym: $90\ \mathrm{GeV} < W < 250\ \mathrm{GeV}; 25\ \mathrm{GeV}^2 < Q^2; x_{\mathbb{P}} < 0{,}01; 0{,}5 < \beta < 0{,}7; 2\ \mathrm{GeV} < p_{t,jet}$. W tym obszarze powinny dominować przypadki dwudżetowe powstałe z pary partonów pochodzących z poprzecznie spolaryzowanego wirtualnego fotonu. Dżety zrekonstruowano przy użyciu ekskluzywnego algorytmu k_t popularnie zwanego algorytmem Durham.

Pierwszy rozdział rozprawy stanowi ogólny wstęp do zagadnienia prezentowanego w pracy. W drugim rozdziale pokrótce omówione jest analizowane zagadnienie od strony teoretycznej. Układ pomiarowy przedstawiony jest w trzecim rozdziale, natomiast wykorzystane w analizie próbki Monte Carlo opisane są w rozdziale czwartym. Rozdziały piąty, szósty i siódmy zawierają opis przeprowadzonej analizy. Zaczynając od metod wykorzystanych w rekonstrukcji wielkości kinematycznych (w tym dżetów), poprzez selekcję przypadków, kończąc na pomiarze rozkładu kąta azymutalnego na poziomie hadronowym. Wnioski przedstawione są w rozdziale ósmym. Dodatek A zawiera spis symboli, natomiast dodatek B zawiera dane przedstawione na wykresach zamieszczonych w pracy.

Kształt rozkładu kąta azymutalnego zmierzony w tej analizie dla dużych wartości β nie zgadza się z przewidywaniami uzyskanymi w przypadku wymiany jednego gluonu. Analiza nie daje podstaw, aby odrzucić przewidywania zakładające wymianę dwóch gluonów. Potwierdza, to teoretyczne oczekiwania, że proces ekskluzywnej dyfrakcyjnej produkcji par dżetów pozwala wyodrębnić "twarde" oddziaływania, czyli takie w których występuje duża skala i które są w pełni opisywalne przez teorie bazujące na rachunku zaburzeń jak chromodynamika kwantowa.

Analiza offline przedstawiona w rozdziałach 6 i 7 jest samodzielną pracą autora tej rozprawy. Analiza efektów promieniowania QED przedstawiona w rozdziale 5.7 również jest efektem w pełni samodzielnej pracy autora.

Contents

1 Introduction **1**

2 Theoretical Framework **3**
2.1 Neutral current lepton - proton interaction . . . 3
2.1.1 Kinematics of lepton - proton interaction . . . 3
2.2 Deep Inelastic Scattering (DIS) . . . 8
2.3 Diffraction . . . 8
2.3.1 Introduction . . . 8
2.3.2 Soft Diffraction . . . 9
2.3.3 Hard Diffraction . . . 11
2.3.4 Diffractive Deep Inelastic Scattering (DDIS) . . . 11
2.4 Diffractive Dijet Production in DIS . . . 12
2.4.1 Boson Gluon Fusion (BGF) . . . 13
2.4.2 Two Gluon Exchange . . . 16
2.5 Aim of the Analysis . . . 20

3 Experimental Setup **21**
3.1 HERA Accelerator . . . 21
3.2 ZEUS Detector . . . 22
3.2.1 Uranium Calorimeter . . . 24
3.2.2 Tracking detectors . . . 25
3.2.3 Luminosity Monitor . . . 26
3.2.4 Trigger . . . 26

4 Monte Carlo Samples **29**
4.1 Diffractive Samples . . . 29
4.2 Non-diffractive Sample . . . 30
4.3 QED Radiation Simulation . . . 30
4.4 Detector Simulation . . . 30

5 Event Reconstruction **31**
5.1 Hadronic Final State Reconstruction . . . 31
5.1.1 Cell Islands . . . 31
5.1.2 Cone Islands . . . 32
5.1.3 Cone island position reconstruction . . . 33
5.1.4 EFO Reconstruction . . . 34
5.1.5 EFO momentum reconstruction . . . 34
5.1.6 Muon corrections . . . 35
5.2 Scattered Lepton Identification and Reconstruction . . . 35
5.3 Kinematics Reconstruction . . . 36

5.3.1 Electron Method . . . 36
5.3.2 Jacquet-Blondel Method . . . 37
5.3.3 Double-Angle Method . . . 38
5.4 Reconstruction of Diffractive Variables . . . 39
5.5 Jet Reconstruction . . . 41
5.5.1 Durham Jet Algorithm . . . 41
5.5.2 Input and Jet Resolution Parameter . . . 42
5.6 Resolutions . . . 43
5.7 QED Radiation . . . 43
5.7.1 Effects of ISR and FSR . . . 45
5.7.2 Radiation Tagged Events . . . 46

6 Data Sample and Signal Selection 49
6.1 Data Sample . . . 49
6.2 Online Selection . . . 49
6.2.1 Trigger Efficiency . . . 51
6.3 DIS Selection . . . 53
6.4 Event Selection . . . 55
6.5 Diffractive Selection . . . 55
6.6 Kinematic Region . . . 57
6.7 Jet Selection . . . 59
6.8 Background Estimation . . . 61

7 Cross Section Measurement and Discussion 63
7.1 Unfolding . . . 63
7.1.1 2D Unfolding . . . 65
7.2 Systematic Uncertainties . . . 66
7.3 Hadron Level Distributions . . . 74
7.4 Hadron Level Cross Sections . . . 77

8 Summary and Conclusions 83

Acknowledgements 85

Appendices 92

A Tables 95
A.1 Reconstruction . . . 95
A.2 Signal Selection . . . 103
A.3 Systematic Uncertainties . . . 111
A.4 Hadron Level Distributions . . . 116
A.5 Hadron Level Cross Sections . . . 116

B Nomenclature 117
B.1 General . . . 117
B.2 Particles . . . 117
B.3 Four-momenta . . . 118
B.4 Variables . . . 118
B.5 Constants . . . 119
B.6 Acronyms . . . 119
B.7 Miscellaneous . . . 120

List of Figures

2.1 Schema of lepton - proton neutral current interaction. 3
2.2 Naive quark parton model schema of deep inelastic scattering (DIS). 6
2.3 Diffractive interactions presented from left to right: elastic scattering $a + b \to a' + b'$, single diffractive dissociation $a + b \to a' + Y$, double diffractive dissociation $a + b \to X + Y$. 9
2.4 Schematic illustration of region devoid of particles due to interaction mediated by a particle that carries no charge. 10
2.5 Definition of azimuthal angle in virtual photon-pomeron centre of mass system with Z axis along the virtual photon momentum and XZ plane spanned by the incoming and scattered lepton. The angle of interest is angle between lepton and parton plane. 13
2.6 Schematic illustration of dijet production in photon-gluon fusion channel $\gamma^* + g \to q + \overline{q}$. 14
2.7 Schematic illustration of dijet production in resolved pomeron model via photon-gluon fusion. 15
2.8 Resolution of azimuthal and polar angles of quark or antiquark reconstructed with exclusive jet. 15
2.9 Diffractive deep inelastic scattering in proton rest frame. In this frame the photon fluctuates into hadronic state. In the left graph the photon fluctuates into $q\overline{q}$ system, in the right graph into $q\overline{q}g$ system. 17
2.10 Diagrams contributing to dijet production via two-gluon exchange. 17
2.11 Taken from [1]. Distribution of β for fixed $x_{\mathbb{P}} = 0.001$ with BEKW model parameters fit to the ZEUS 1994 data. Upper solid line shows F_2^{D}, dashed line - $F_{q\overline{q}}^T$, dotted line - $F_{q\overline{q}g}^T$, dashed-dotted line - $Flqq$, lower solid line - $\Delta F_{q\overline{q}}^T$. 19
2.12 Taken from [2]. Distributions of azimuthal angle of parton originating from $q\overline{q}$ system. Distributions are calculated in kinematic region of $Q^2 = 100$ GeV and $p_{t,q}^2 > 5$ GeV^2. Left hand graph shows distribution for $\beta = 1/3$, right hand graph for $\beta = 2/3$. Solid line shows distribution obtained with two gluon exchange, dashed line shows distribution obtained with photon-gluon fusion (single gluon exchange). 19

3.1 Integrated luminosity delivered by the HERA accelerator. HERA II luminosity is split to electron and positron contributions. 22
3.2 A schema of HERA accelerator and position of experiments. 23
3.3 Coordinate system used in the ZEUS collaboration. 23
3.4 Schema of the ZEUS detector XY cross section. 24
3.5 Schema of the ZEUS detector XZ cross section. 25

4.1 Feynman diagrams describing the leading order QED corrections from left to right are: initial state radiation, final state radiation, vertex correction, self-energy correction. 30

5.1 Definition of nearest neighbours of a cell. Cells in corners are not considered as nearest neighbours. 32

5.2 Example of cell clustering with cell island clustering algorithm. 32

5.3 Connection weight as a function of angular separation. Dashed line shows connection weight between hadronic clusters, solid line shows connection weight between hadronic and electromagnetic clusters as well as between electromagnetic clusters. 33

5.4 Distributions of relative differences between reconstructed and generated, values of kinematic variables estimated with SATRAP. Distributions of Bjorken scaling variable (on the left) and inelasticity (on the right) are presented in the upper row. Distributions of virtuality (on the left) and boson-proton centre of mass energy (on the right) are presented in the lower row. Dotted histograms show relative differences for kinematic variables reconstructed with electron method, dashed histograms show relative differences for kinematic variables reconstructed with Jacquet-Blondel method, solid histograms show relative differences for kinematic variables reconstructed with double-angle method. 40

5.5 Distributions of relative differences between reconstructed, with double-angle method, and generated values of diffractive variables estimated with SATRAP. In the left graph distribution of fraction of incoming proton momentum carried by pomeron is shown. In the right graph distribution of fraction of pomeron momentum carried by interacting parton is shown. 41

5.6 Display of event 1554 of run 61588. Green arrows represent energy flow objects. Yellow arrow shows EFO identified as scattered lepton. Size of red rectangles is proportional to energy deposited in calorimeter cell. In lower left corner of the calorimeter, isolated EFO with low energy is visible. If it were present on jet algorithm particles input list, it would create a fake jet. 42

5.7 Distribution of separations, in pseudorapidity and azimuthal angle, of EFO with energy smaller than 400 MeV from EFOs with energy greater than 400 MeV. Solid lines corresponds to events with well reconstructed jets ($|\Delta p_{t,jet}/p_{t,jet}| < 0.1$) and dashed line corresponds to events with badly reconstructed jets ($\Delta p_{t,jet}/p_{t,jet} > 0.4$). 43

5.8 Distribution of differences of jet azimuthal angle reconstructed on detector and hadron level as a function of detector jet azimuthal angle (on the left) and detector jet transverse momentum (on the right). Markers show mean value of the distribution of differences for a given interval of detector jet azimuthal angle. Error bars show standard deviation of the distribution of differences for a given interval of detector jet azimuthal angle. 44

5.9 Distribution of differences of jet transverse momentum reconstructed on detector and hadron level in function of detector jet azimuthal angle. Markers show mean value of the distribution of differences for a given interval of detector jet azimuthal angle. Error bars show standard deviation of the distribution of differences for a given interval of detector jet azimuthal angle. 44

5.10 Azimuthal angular distribution of jets reconstructed on hadron level. SATRAP 2006 electron sample was used. Events were requiered to pass the following selection criteria: $\beta > 0.45, x_{I\!P} < 0.01, 100\ \text{GeV} < W < 300\ \text{GeV}, p_{t,jet} > 2\ \text{GeV}$. Solid histogram shows distribution calculated with correct virtual photon, dashed histogram shows distribution reconstructed with virtual photon four-momentum calculated as the difference between incoming and scattered lepton, which does not take into account ISR and FSR. 45

5.11 Jet azimuthal angle resolution obtained using MC containing ISR and FSR. In the left graph a distribution of differences between jet azimuthal angle reconstructed on detector and hadron level in function of hadron jet azimuthal angle is presented. In the right graph distribution of differences between jet azimuthal angle reconstructed on detector and hadron level for hadron jet azimuthal angles between 1.55 and 1.95 is presented. 46

5.12 Jet azimuthal angle resolution obtained using MC without ISR nor FSR. In the left graph distribution of differences between jet azimuthal angle reconstructed on detector and hadron level in function of hadron jet azimuthal angle is presented. In the right graph distribution of differences between jet azimuthal angle reconstructed on detector and hadron level for hadron jet azimuthal angles between 1.2 and 1.6 is presented. 47

5.13 Distribution of differences in inelasticity reconstructed with electron and Jacquet-Blondel methods. Figure shows the differences obtained with data and SATRAP MC after the standard selection criteria described in ch. 6 on page 49. Black points show distribution of data as well as statistical errors. Black histogram shows SATRAP distribution. Dashed histogram shows distribution of MC events without ISR or FSR. 47

5.14 Jet azimuthal angular distribution in virtual photon-pomeron centre of mass frame, after the standard selection criteria described in ch. 6 on page 49. Solid histogram shows distribution of events with $y_{\text{El}} - y_{\text{JB}} < 0.005$ i.e. with negligible impact of initial or final state radiation, dashed histogram shows distribution of events with $y_{\text{El}} - y_{\text{JB}} > 0.2$ i.e. with dominating effects of ISR or FSR. 48

6.1 Integrated luminosity gated by the ZEUS detector in years 2002 - 2007 split into periods of data taking. Figure taken from [3] 50

6.2 Taken from [4]. View from the interaction point of the FCAL trigger regions and trigger towers. 52

6.3 Trigger efficiency as a function of jet azimuthal angle. Black points show distribution of trigger efficiency calculated with data and statistical uncertainties. Histogram shows trigger efficiency calculated with MC. 52

6.4 Control distributions of scattered lepton energy reconstructed with double-angle method (on the left) and distance separating scattered lepton energy deposit in calorimeter from extrapolated track associated with it (on the right). Black points show distribution of data with statistical uncertainties. Black histograms show SATRAP distributions. Dashed lines show cut values. 54

6.5 Scattered lepton reconstructed position (black solid line shows the TLT box cut). 54

6.6 Control distributions of vertex position along the beam pipe (on the left) and number of tracks associated with the vertex (on the right) are shown in the upper row. Control distributions of number of EFOs in diffractive final state (on the left) and fraction of total energy deposited in hadronic calorimeter (on the right) are presented in the lower row. Black points show distribution of data with statistical uncertainties. Black histograms show SATRAP distributions. Dashed lines show cut values. 56

6.7 Control distribution showing energy-momentum along the beam pipe balance. Black points show distribution of data with statistical uncertainties. Black histograms show SATRAP distributions. Dashed lines show cut values. 57

6.8 Control distributions of maximal pseudorapidity of EFOs with energy greater than 400 MeV (on the left) and reconstructed fraction of incoming proton momentum carried by the pomeron (on the right) are shown in the upper row. Control distributions of invariant mass of diffractive system (on the left) and fraction of pomeron momentum carried by the interacting parton (on the right) are shown in the lower row. Dashed histogram shows number of three parton events ($q\bar{q}g$), dotted — two parton events ($q\bar{q}$). Black points show distribution of data with statistical uncertainties. Black histograms show SATRAP distributions. Dashed lines show cut values. 58

6.9 Control distributions of photon virtuality reconstructed with double-angle method (on the left) and photon-proton invariant mass reconstructed with double-angle method (on the right) are presented in the upper row. Below, a control distribution of inelasticity reconstructed with electron method is shown. Black points show distribution of data with statistical uncertainties. Black histograms show SATRAP distributions. Dashed lines show cut values. 60

6.10 Control distribution showing jet transverse momentum in virtual photon-pomeron centre of mass system. Black points show distribution of data with statistical uncertainties. Black histograms show SATRAP distributions. Dashed lines show cut values. 61

7.1 Two dimensional distribution of jet azimuthal angle and transverse momentum. Jet azimuthal angular distribution is measured in 32 bins of equal size covering range of $\phi_{jet} \in [-\pi, \pi]$. Vertical dashed lines separate transverse momentum bins. The following edges of transverse momentum bins in GeV are used: 0, 1, 2, 10. This means that the distribution before the first dashed line corresponds to transverse momentum between 0 GeV and 1 GeV, the distribution between the first and second dashed line corresponds to transverse momentum from 1 GeV to 2 GeV and between the second and third dashed line corresponds to transverse momentum from 2 GeV to 10 GeV. Dashed histogram shows contribution from events that lay outside of the studied kinematic region (eq. 7.9 to eq. 7.14 on page 64). 65

7.2 Two dimensional distribution of virtuality reconstructed with double-angle method and transverse momentum. Photon virtuality distribution consists of 12 bins corresponding to the following virtualities in GeV^2): [25, 45), [45, 65), [65, 85), [85, 105), [105, 125), [125, 145), [145, 165), [165, 185), [185, 205), [205, 225), [225, 245), [245, 295). Vertical dashed lines separate transverse momentum bins. The following edges of transverse momentum bins in GeV are used: 0, 1, 2, 10. This means that the distribution before the first dashed line corresponds to transverse momentum between 0 GeV and 1 GeV, the distribution between the first and second dashed line corresponds to transverse momentum from 1 GeV to 2 GeV and between the second and third dashed line corresponds to transverse momentum from 2 GeV to 10 GeV. Dashed histogram shows contribution from events that lay outside of the studied kinematic region (eq. 7.9 to eq. 7.14 on page 64). 66

7.3 Resolutions of kinematic variables estimated with SATRAP as a function of the variables themselves. Resolutions of diffractive system mass (on the left) and inelasticity (on the right) are presented in the upper row. Resolutions of virtuality (on the left) and boson-proton centre of mass energy (on the right) are presented in the lower row. 68

7.4 Resolution of fraction of incoming proton momentum carried by pomeron as a function of the variable itself estimated with SATRAP. 69

7.5 Systematic uncertainties of jet azimuthal angular distribution originating from event selection. Markers show relative differences between number of events obtained with nominal and varied measurement. Vertical error bars show statistical uncertainty. In most cases uncertainties are smaller than points and error bars are not visible. Lines show statistical uncertainty of the nominal result. 70

7.6 Systematic uncertainties of jet azimuthal angular distribution originating from detector simulation and measurement technique. Markers show relative differences between number of events obtained with nominal and varied measurement. Vertical error bars show statistical uncertainty. In most cases uncertainties are smaller than points and error bars are not visible. Lines show statistical uncertainty of the nominal result. 71

7.7 Systematic uncertainties of virtuality distribution originating from event selection. Markers show relative differences between number of events obtained with nominal and varied measurement. Vertical error bars show statistical uncertainty. In most cases uncertainties are smaller than points and error bars are not visible. Lines show statistical uncertainty of the nominal result. 72

7.8 Systematic uncertainties of virtuality distribution originating from detector simulation and measurement technique. Markers show relative differences between number of events obtained with nominal and varied measurement. Vertical error bars show statistical uncertainty. In most cases uncertainties are smaller than points and error bars are not visible. Lines show statistical uncertainty of the nominal result. 73

7.9 Systematic uncertainties originating form the jet resolution parameter. Markers show relative differences between number of events obtained with nominal and varied measurement. Vertical error bars show statistical uncertainty. In most cases uncertainties are smaller than points and error bars are not visible. Lines show statistical uncertainty of the nominal result. 74

7.10 Hadron level distributions of jet azimuthal angle and virtuality. Error bars show square root of diagonal elements of statistical covariance matrix. Gray band shows square root of diagonal elements of systematic covariance matrix. Solid line histogram shows distribution shape predicted by 2-gluon exchange model. Dashed line histogram shows distribution shape predicted by boson-gluon fusion model. 75
7.11 Vectors of variance and correlation matrices of unfolded hadron level jet azimuthal angular distribution. Upper set is only statistical. Lower is total i.e. statistical and systematic. 75
7.12 Covariance matrices of unfolded hadron level virtuality distribution. Upper matrix is only statistical. Lower is total covariance, i.e. statistical and systematic. . 76
7.13 Diagram of ξ_i parameters for jet azimuthal angular distribution compared with two-gluon exchange model that minimise pull method χ^2. 78
7.14 Diagram of ξ_i parameters for photon virtuality distribution compared with two-gluon exchange model that minimise pull method χ^2. 79
7.15 Diagram of ξ_i parameters for jet azimuthal angular distribution compared with boson gluon fusion exchange model that minimise pull method χ^2. 80
7.16 Diagram of ξ_i parameters for photon virtuality distribution compared with boson gluon fusion model that minimise pull method χ^2. 81
7.17 Hadron level distributions of jet azimuthal angle in region of $0.05 < \beta < 0.15$. Error bars represent only statistical uncertainty. 82
7.18 Hadron level single differential cross sections as a function of jet azimuthal angle and virtuality. Error bars show square root of diagonal elements of statistical covariance matrix. Gray band shows square root of diagonal elements of systematic covariance matrix. 82

Chapter 1

Introduction

The goal of natural sciences is to understand and describe the world. Particle physics is focused on investigating the structure of the matter and interactions between its constituents. It lead to development of different theoretical models. Quantum electrodynamics (QED) successfully describes all electromagnetic interactions. Quantum chromodynamics (QCD) is expected to give description of strong interactions. Many experiments proved its usefulness in the presence of hard scale. However, due to large coupling constant α_s the perturbative theory breaks down in certain kinematic regions. These soft regions, are described by different phenomenological models. Many attempts are made to extrapolate QCD to the soft region. It is clear that more fundamental theory is needed in order to describe strong interactions in all kinematic regions. The studies of the regions where perturbative theory starts to break, can broaden the scope of knowledge about strong interactions. One of the processes that lay between perturbative and non-perturbative regions is diffractive scattering.

Diffraction has drawn a lot of attention since the end of 1980s. It started with the observation of so called hard diffraction, i.e. diffraction in the presence of large scale, at the SPS accelerator. This observation was confirmed by measurements at Tevatron. A large surprise were HERA results, showing a presence of events with large rapidity gap properties in the hadronic final state, which is experimental signature of diffractive scattering. These diffractive events amounted to about 10% of the events. This observation opened the possibility to study properties of diffractive exchange in similar way, as the interaction of proton is studied. High photon virtualities allowed for investigations of the structures of particles mediating diffractive interactions and their nature. It turned out that in regions where perturbative calculations are permitted, pQCD is able to describe the data as good as models based on quark parton approach QPM.

Most of the diffractive processes are a mix of soft and hard contributions. However, high transverse momentum diffractive dijet production is expected to allow for hard component extraction. A significant difference between the perturbative QCD and naive QPM models is predicted in this process. Quark parton models are based on interaction of the photon with a single parton (quark or gluon), while perturbative QCD in the lowest order is based on photon interaction with two-gluon system. The striking consequence of different number of objects interacting with photon is a change in the shape of jets azimuthal angular distribution. The aim of this analysis is experimental verification of the two models predictions. Data gathered by the ZEUS detector in years 2003–2007, which amounts to integrated luminosity of approximately 350 pb^{-1}, serve this purpose.

The thesis begins with introduction of theoretical background. Chapters 3 to 5 contain description of "utilities" used in the analysis, starting with short description of the experimental setup (i.e. HERA accelerator and ZEUS detector), through Monte Carlo, ending with event reconstruction. Chapter 6 contains the description of the exclusive diffractive dijet extraction

method, used to obtain results presented in chapter 7. The thesis is closed with summary and conclusions. The reference table of symbols used in the thesis is in the first appendix. Most of the distributions presented in the thesis have corresponding tables with data points, which are placed in the second appendix.

The offline analysis of exclusive diffractive dijet production presented in chapters 6 and 7 is the author's original work. QED radiation studies presented in sec. 5.7 are also the author's authentic contribution.

The author was also responsible for preparing the inclusive diffractive Monte Carlo sample that is available in ZEUS Common Ntuples (CN). Common Ntuples are a final and only available set of ZEUS data that is going to be maintained in the long term. Generated diffractive sample is also used in this analysis. Apart from this the author have also contributed to preparations of documentation and guidelines that will be used in new analyses of the ZEUS data. The author took part in choosing and describing a set of standard deep inelastic selection criteria, as well as implementing them in the environment of CN. Has also contributed to the documentation of procedures used in event reconstruction.

Chapter 2

Theoretical Framework

2.1 Neutral current lepton - proton interaction

Lepton - proton interaction can be mediated by a neutral boson. This type of interaction is referred to as neutral current interaction (NC). Schema of the process is presented in fig. 2.1. Lepton (labelled e) interacts with proton (p) by exchange of a neutral boson. The mediating boson can be either a virtual photon or a Z^0 but for Q^2 range covered by this analysis contribution from Z^0 exchange can be neglected. The photon couples to a parton (ξ) in proton. It leads to creation of a hadronic system h. Interaction with lepton can lead to proton disintegration or scattering. The scattered proton (or its remnants) is labelled p'. Lepton is always scattered (e'). It is a property of NC interaction.

2.1.1 Kinematics of lepton - proton interaction

Total energy in lepton - proton system is referred to as center of mass energy s and is defined as

$$\sqrt{s} := \sqrt{(\mathbf{P} + \mathbf{k})^2}\,. \tag{2.1}$$

$\mathbf{P}$ and $\mathbf{k}$ are incoming proton and lepton four-momenta, respectively. At high energies proton and lepton masses can be neglected simplifying the above formula

$$\sqrt{s} \approx \sqrt{2\mathbf{P}\mathbf{k}}\,. \tag{2.2}$$

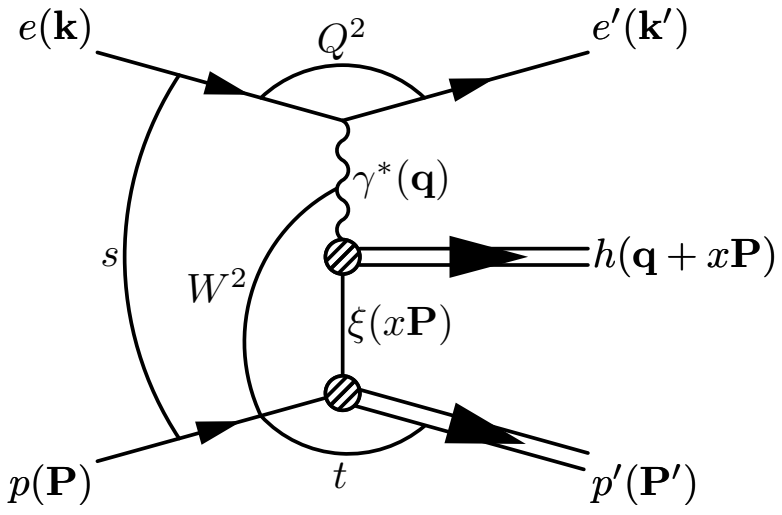

Figure 2.1: Schema of lepton - proton neutral current interaction.

In reference frame in which incoming proton and lepton move along the Z axis, with proton moving in the positive and lepton in the negative direction in the laboratory frame, lepton and proton four-momenta (neglecting rest masses) read

$$\mathbf{P} = (E_p, 0, 0, E_p) \,, \tag{2.3}$$
$$\mathbf{k} = (E_e, 0, 0, -E_e) \,. \tag{2.4}$$

In this frame total energy can be approximated with colliding particles energies

$$\sqrt{s} = \sqrt{4E_pE_e} \,. \tag{2.5}$$

More adequate measure of interaction energy is boson - proton centre of mass energy

$$W := \sqrt{(\mathbf{P} + \mathbf{q})^2} \,. \tag{2.6}$$

Exchanged boson four-momentum ($\mathbf{q}$) can be calculated with energy and momentum conservation law

$$\mathbf{q} = \mathbf{k} - \mathbf{k}' \,. \tag{2.7}$$

Exchanged virtual boson squared four-momentum is negative. In order not to use negative values, virtuality (Q^2) is introduced. It is defined as squared four-momentum transfer at lepton vertex

$$Q^2 := -\mathbf{q}^2 \,. \tag{2.8}$$

Neglecting incoming and scattered leptons masses, virtuality can be expressed in terms of leptons energies and scattered lepton polar angle

$$Q^2 = -(\mathbf{k} - \mathbf{k}')^2 \tag{2.9}$$
$$= -\left(\mathbf{k}^2 - 2\mathbf{k}\mathbf{k}' + \mathbf{k}'^2\right) \tag{2.10}$$
$$\approx 2\mathbf{k}\mathbf{k}' \,. \tag{2.11}$$

Massless incoming and scattered leptons four-momenta in laboratory frame read

$$\mathbf{k} = (E_e, 0, 0, -E_e) \tag{2.12}$$
$$\mathbf{k}' = (E_{e'}, E_{e'} \sin\theta_{e'} \cos\phi_{e'}, E_{e'} \sin\theta_{e'} \sin\phi_{e'}, E_{e'} \cos\theta_{e'}) \,, \tag{2.13}$$

where $\phi_{e'}$ and $\theta_{e'}$ are azimuthal and polar angles of the scattered lepton, respectively. For incoming lepton momentum has no transverse components,

$$Q^2 = 2\mathbf{k}\mathbf{k}' = 2E_eE_{e'}\left(1 + \cos\theta_{e'}\right) \,. \tag{2.14}$$

Virtuality determines Compton wavelength associated with the virtual photon $\lambda_{\gamma^*} = \hbar/\sqrt{Q^2}$. Thus it is related to the resolving power of the photon. The higher the Q^2, the finer proton structure is probed. Interactions with high Q^2 values can be referred to as hard interactions.

Another quantity that is connected with lepton-proton scattering is inelasticity y. It is defined as

$$y := \frac{\mathbf{P}\mathbf{q}}{\mathbf{P}\mathbf{k}} \,. \tag{2.15}$$

Inelasticity is invariant under Lorentz rotation and is interpreted as a fraction of lepton energy transferred to the proton. This interpretation is clear in incoming proton rest frame with masses of proton and lepton being neglected

$$\mathbf{P} = (E_p, 0, 0, 0) \Rightarrow y = \frac{E_p\left(E_e - E_{e'}\right)}{E_pE_e} = \frac{E_e - E_{e'}}{E_e} \,. \tag{2.16}$$

The above equation can be easily used to set a range of possible y values $y \in [0, 1]$.

In coordinate system in which incoming lepton and proton have no transverse momentum inelasticity can be expressed as follows

$$\begin{aligned} y &:= \frac{\mathbf{Pq}}{\mathbf{Pk}} = \frac{\mathbf{P}\left(\mathbf{k}-\mathbf{k}'\right)}{\mathbf{Pk}} = 1 - \frac{\mathbf{Pk}'}{\mathbf{Pk}} && (2.17)\\ &= 1 - \frac{E_p E_{e'} - p_{z,p} p_{z,e'}}{E_p E_e - p_{z,p} p_{z,e}} && (2.18)\\ &= 1 - \frac{E_p E_{e'} - E_p E_{e'} \cos\theta_{e'}}{E_p E_e + E_p E_e} && (2.19)\\ &= 1 - \frac{E_{e'}}{2E_e}\left(1 - \cos\theta_{e'}\right) . && (2.20) \end{aligned}$$

In the proton vertex analogous variables are defined. Squared four-momentum transferred at the proton vertex is defined as

$$t := \left(\mathbf{P} - \mathbf{P}'\right)^2 \tag{2.21}$$

and Bjorken scaling variable

$$x := \frac{Q^2}{2\mathbf{Pq}} . \tag{2.22}$$

In approximation of massless scattered parton and in proton infinite-momentum frame it can be interpreted as a fraction of proton momentum carried by the interacting quark. For in reference frame in which proton moves very fast transverse momenta of proton constituents are negligibly small compared to longitudinal ones. Thus the four-momentum ($\mathbf{\Xi}$) of the struck parton (ξ) can be expressed as a fraction of incoming proton four-momentum

$$\mathbf{\Xi} = \zeta \mathbf{P} . \tag{2.23}$$

In case of high proton energies ($m_p \ll E$) it can be assumed that the incoming proton is massless ($\mathbf{P}^2 = 0$). In this case the interacting parton ξ absorbs the boson and remains massless. Using the above assumption it can be shown that $\zeta = x$

$$\begin{aligned} \left(\zeta\mathbf{P} + \mathbf{q}\right)^2 &= 0 && (2.24)\\ \zeta^2\mathbf{P}^2 + 2\zeta\mathbf{Pq} + \mathbf{q}^2 &= 0 && (2.25)\\ 2\zeta\mathbf{Pq} &= -\mathbf{q}^2 && (2.26)\\ \zeta &= \frac{Q^2}{2\mathbf{Pq}} && (2.27)\\ \zeta &= x . && (2.28) \end{aligned}$$

Limits of x can be derived from the definition

$$\begin{aligned} x &= \frac{Q^2}{2\mathbf{Pq}} && (2.29)\\ &= \frac{Q^2}{\left(2\mathbf{Pq} + \mathbf{P}^2 + \mathbf{q}^2\right) - \mathbf{P}^2 - \mathbf{q}^2} && (2.30)\\ &= \frac{Q^2}{\left(\mathbf{P} + \mathbf{q}\right)^2 - \mathbf{P}^2 - \mathbf{q}^2} && (2.31)\\ &= \frac{Q^2}{W^2 - \mathbf{P}^2 + Q^2} && (2.32) \end{aligned}$$

$$\left.\begin{aligned} Q^2 &> 0\\ \left(\mathbf{P} + \mathbf{q}\right)^2 &\geq \mathbf{P}^2 \end{aligned}\right\} \Rightarrow \quad x \in [0, 1] . \tag{2.33}$$

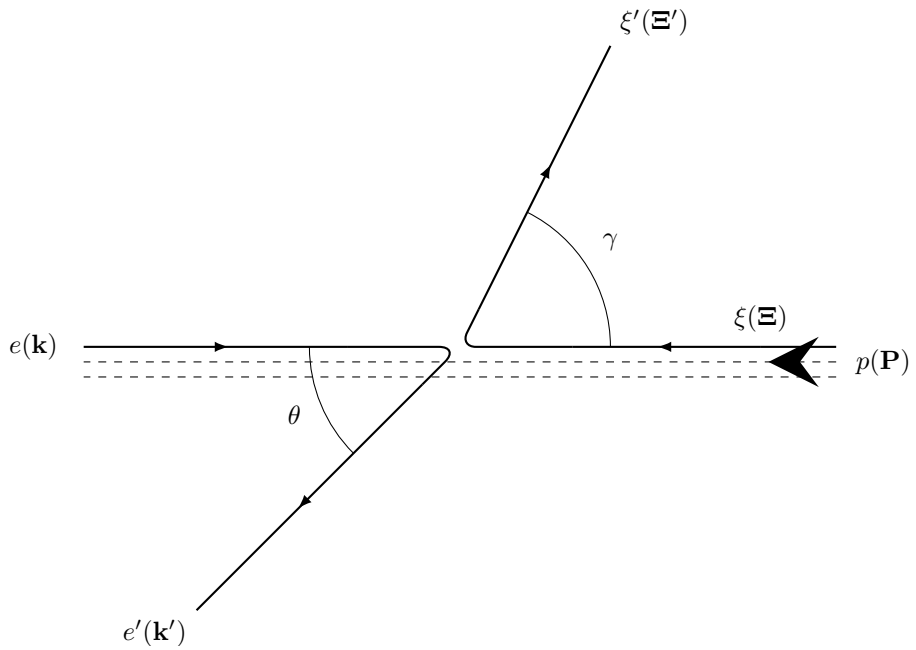

Figure 2.2: Naive quark parton model schema of deep inelastic scattering (DIS).

The limits of x are in agreement with its interpretation as a fraction of proton four-momentum carried by the interacting parton. It is worth to note that in the limit $Q^2 \ll W^2$ eq. 2.32 on the previous page can be approximated by

$$x \approx \frac{Q^2}{(\mathbf{P}+\mathbf{q})^2} = \frac{Q^2}{W^2}\,. \tag{2.34}$$

Having the basic kinematic quantities defined, a relation between them can be derived. By definition

$$xy = \frac{Q^2}{2\mathbf{Pq}}\frac{\mathbf{Pq}}{\mathbf{Pk}} = \frac{Q^2}{2\mathbf{Pk}}\,. \tag{2.35}$$

Using approximated value of lepton-proton centre of mass energy (eq. 2.2 on page 3) equation combining these basic kinematic quantities is obtained

$$xy = \frac{Q^2}{2\mathbf{Pk}} = \frac{Q^2}{s-m_p^2} \tag{2.36}$$

$$Q^2 = xy\left(s-m_p^2\right)\,. \tag{2.37}$$

Energy of virtual photon-proton system can be expressed in terms of inelasticity and virtuality assuming that colliding particles are massless

$$W = \sqrt{(\mathbf{P}+\mathbf{q})^2} = \sqrt{2\mathbf{Pq}-Q^2}\,. \tag{2.38}$$

With the help of eq. 2.15 on page 4, eq. 2.2 on page 3 and eq. 2.5 on page 4 the above equation can be written as

$$W = \sqrt{2\mathbf{Pk}y-Q^2} = \sqrt{sy-Q^2} = \sqrt{4E_eE_py-Q^2}\,. \tag{2.39}$$

Basing on naive quark parton model further relations can be derived. In this model lepton (e) interacts only with one parton (ξ). Struck parton (ξ) is assumed not to interact with other proton constituents. Schema of lepton - proton interaction seen from the point of view of naive

quark parton model is presented in fig. 2.2 on the facing page. The following reasoning is performed in coordinate system in which incoming proton and lepton move along Z axis. Z proton momentum is positive, while lepton - negative (eq. 2.3 on page 4 and eq. 2.4 on page 4). In this reference frame energy and momentum conservation laws yield

$$\mathbf{k} + \mathbf{\Xi} = \mathbf{k}' + \mathbf{\Xi}' \,. \tag{2.40}$$

It directly follows that boson four-momentum equals

$$\mathbf{q} = \mathbf{k} - \mathbf{k}' = \mathbf{\Xi}' - \mathbf{\Xi} \,. \tag{2.41}$$

Energy and momentum conservation laws can be expressed as a system of three equations: energy conservation, longitudinal and transverse momentum conservation

$$\left\{ \begin{array}{rcl} E_\xi + E_e & = & E_{\xi'} + E_{e'} \\ 0 & = & p_{t,\xi'} - p_{t,e'} \\ p_{z,\xi} + p_{z,e} & = & p_{z,\xi'} + p_{z,e'} \end{array} \right. . \tag{2.42}$$

Combining energy and longitudinal momentum conservation system of two equations is obtained

$$\left\{ \begin{array}{rcl} p_{t,e'} & = & p_{t,\xi'} \\ E_\xi - p_{z,\xi} + E_e - p_{z,e} & = & E_{\xi'} - p_{z,\xi'} + E_{e'} - p_{z,e'} \end{array} \right. \tag{2.43}$$

$$\left\{ \begin{array}{rcl} p_{t,e'} & = & p_{t,\xi'} \\ 2E_e & = & E_{\xi'} - p_{z,\xi'} + E_{e'} - p_{z,e'} \,. \end{array} \right. \tag{2.44}$$

The above system of equations allows for expressing scattered lepton energy in terms of parton and lepton angles

$$\left\{ \begin{array}{rcl} E_{\xi'} \sin\theta_{\xi'} & = & E_{e'} \sin\theta_{e'} \\ 2E_e & = & E_{\xi'} \left(1 - \cos\theta_{\xi'}\right) + E_{e'} \left(1 - \cos\theta_{e'}\right) \end{array} \right. \tag{2.45}$$

$$\left\{ \begin{array}{rcl} E_{\xi'} & = & E_{e'} \frac{\sin\theta_{e'}}{\sin\theta_{\xi'}} \\ 2E_e & = & E_{e'} \frac{\sin\theta_{e'}}{\sin\theta_{\xi'}} \left(1 - \cos\theta_{\xi'}\right) + E_{e'} \left(1 - \cos\theta_{e'}\right) \end{array} \right. \tag{2.46}$$

$$E_{e'} = \frac{2E_e \sin\theta_{\xi'}}{\sin\theta_{e'} \left(1 - \cos\theta_{\xi'}\right) + \sin\theta_{\xi'} \left(1 - \cos\theta_{e'}\right)} \tag{2.47}$$

$$= \frac{2E_e \sin\theta_{\xi'}}{\sin\theta_{e'} + \sin\theta_{\xi'} - \sin\left(\theta_{\xi'} + \theta_{e'}\right)} \,. \tag{2.48}$$

The correspondence of lepton and parton momenta shown in eq. 2.41 can be used to express kinematic variables only in terms of parton momentum. These formulae can be used to take calculations to hadron level by approximating scattered parton momentum with hadronic final state momentum. The hadronic system momentum is the sum of all hadrons momenta

$$\left(E_h, p_{x,h}, p_{y,h}, p_{z,h}\right) = \sum_{i \in h} \left(E_i, p_{x,i}, p_{y,i}, p_{z,i}\right) \,. \tag{2.49}$$

Inelasticity, defined in eq. 2.15 on page 4, expressed with parton momentum reads

$$y := \frac{\mathbf{Pq}}{\mathbf{Pk}} = \frac{\mathbf{P}\left(\mathbf{\Xi}' - \mathbf{\Xi}\right)}{\mathbf{Pk}} = \frac{E_{\xi'} - p_{z,\xi'}}{2E_e} \,. \tag{2.50}$$

Replacing scattered parton four-momentum with hadronic system four-momentum, final equation is obtained

$$y = \frac{E_h - p_{z,h}}{2E_e}\,. \tag{2.51}$$

Virtuality can be calculated using eq. 2.14 on page 4 and eq. 2.20 on page 5

$$\begin{aligned} Q^2\,(1-y) &= 2E_eE_{e'}\,(1+\cos\theta_{e'})\,\frac{E_{e'}}{2E_e}\,(1-\cos\theta_{e'}) && (2.52)\\ &= E_{e'}^2\sin^2(\theta_{e'}) = p_{t,e'}^2 && (2.53)\\ &\Downarrow \\ Q^2 &= \frac{p_{t,e'}^2}{1-y}\,. && (2.54) \end{aligned}$$

Substituting scattered lepton transverse momentum with scattered parton transverse momentum, which can be approximated by transverse momentum of hadronic system, the following expression is obtained

$$Q^2 = \frac{p_{t,\xi'}^2}{1-y} = \frac{p_{t,h}^2}{1-y}\,. \tag{2.55}$$

2.2 Deep Inelastic Scattering (DIS)

Neutral current interactions with $Q^2 \gg 1\ \mathrm{GeV}^2$ are called deep inelastic scattering (DIS). In this kinematic regime it is assumed that the exchanged boson interacts with one of the proton constituents. In this case, the constituents are point like and free.

2.3 Diffraction

Interaction with no quantum numbers, but spin and parity, exchanged between proton and boson (virtual photon) is called diffractive. This theoretical definition is very difficult to apply in experiment. Experimentally, diffractive interaction is identified as interaction with large rapidity gap LRG i.e. space in rapidity devoid of particles. Mentioned above experimental and theoretical interpretations of diffractive interaction are not equivalent.

2.3.1 Introduction

In 1923 Louis de Broglie published a note [5] with an idea that a particle can be viewed as a wave. The length of the wave depends on particle momentum (p)

$$\lambda = \frac{h}{\mathrm{p}}\,, \tag{2.56}$$

h being Planck constant. More extensively the idea was described in the first chapter of Louis de Broglie's Ph.D. thesis [6]. In 1927 de Broglie's idea was confirmed experimentally. In April Clinton Davisson and Lester Halbert Germer published the results of electron diffraction by a single crystal of nickel [7]. Independently George Paget Thomson and Andrew Reid published results of electron diffraction by thin celluloid film [8] in June. Possibility to describe particle as a wave allowed for application of optical theorems in nuclear and particle physics.

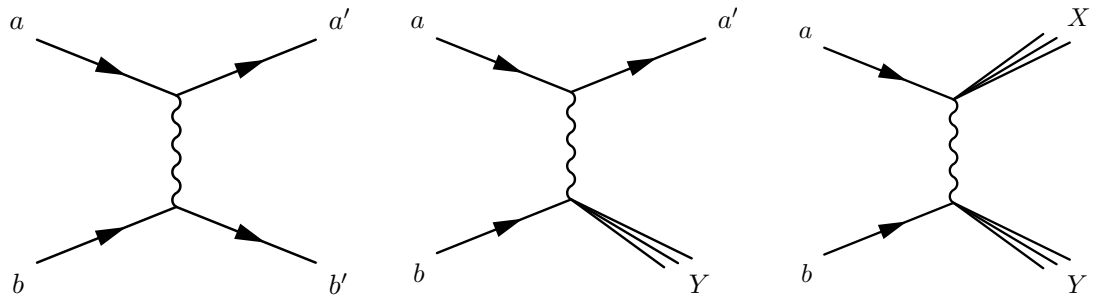

Figure 2.3: Diffractive interactions presented from left to right: elastic scattering $a+b \to a'+b'$, single diffractive dissociation $a + b \to a' + Y$, double diffractive dissociation $a + b \to X + Y$.

Diffraction in Optics

Diffraction of light is a phenomenon observed when light passes the slit of size comparable with its wave length. A special case called Fraunhofer diffraction assumes that the incident light is a plane wave and the image is viewed at infinitely distant screen

$$kR/D \ll 1\,. \tag{2.57}$$

D is the distance separating the slit from the detector, k is wave number inversely proportional to the wave length $k = 2\pi/\lambda$, R is the size of the slit. Observed diffractive image consists of light and dark stripes.

Diffraction in Particle Physics

Taking into account colliding particles energy, their size and position of detectors it turns out that Fraunhofer diffraction condition presented in eq. 2.57 is fulfilled. It was observed that elastic scattering of hadrons

$$a + b \to a' + b' \tag{2.58}$$

yields angular distributions similar to patterns obtained by diffraction of light. Due to this resemblance the name diffraction was introduced into particle physics.

In fifties diffraction was developed by taking into account the quantum nature of the interacting particles [9, 10, 11]. It was considered that the wave function of the scattered particle is being changed. This can lead to particle dissociation. Three types of diffraction can be distinguished: elastic scattering, single diffractive dissociation and double diffractive dissociation. Schematically the processes are shown in fig. 2.3.

Multi-particle dissociated final state preserves quantum numbers of the initial particle. The only quantum numbers that can change are spin and parity. Quantum numbers are preserved when mediating particle carries no charge. A consequence of the fact that a particle with vacuum quantum numbers is exchanged is, that a space devoid of particles is created. This signature is used to experimentally identify diffraction. It is worth noting that space devoid of particles can be also present in non-diffractive interactions, however its creation is exponentially suppressed [12]. The empty region is usually shown in terms of rapidity and referred to as a rapidity gap. A visualisation of the gap is presented in fig. 2.4 on the next page.

2.3.2 Soft Diffraction

One of the models that is used to describe hadron-hadron interaction is Regge phenomenology [13, 14, 15]. Regge phenomenology is based on S-matrix approach. Elastic scattering $2 \to 2$ is

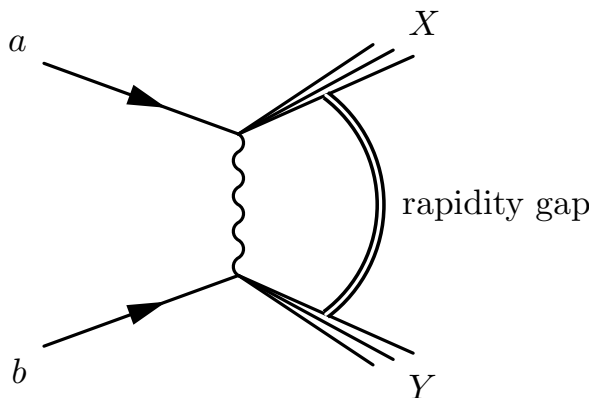

Figure 2.4: Schematic illustration of region devoid of particles due to interaction mediated by a particle that carries no charge.

described by amplitude of the form

$$\mathrm{S}(s,t) = \mathrm{I} + i\mathrm{T}(s,t)\,. \tag{2.59}$$

I is unit matrix and T is transition matrix that depends on Mandelstam variable t and centre of mass energy s.

Regge phenomenology assumes that all resonances that can mediate the scattering contribute to the scattering amplitude. These resonances can be assembled into groups containing particles that differ only by spin. It turned out that particles from such groups, form a straight line in spin-squared mass plane. The straight line is called Regge trajectory. The trajectory depends on Mandelstam t variable and is parametrised

$$\alpha(t) = \alpha(0) + \alpha' t\,. \tag{2.60}$$

Trajectories formed by mesons are called reggeons. The transition matrix is the sum of appropriate trajectories

$$\mathrm{T} = \sum_k \beta_{ak}(t)\beta_{bk}(t)s^{\alpha_k(t)}\,. \tag{2.61}$$

$\beta_{ak}(t), \beta_{bk}(t)$ are residue functions that describe couplings between scattering hadrons and the trajectories, s is the centre of mass energy. S matrix can be used to calculate the elastic scattering cross section of two hadrons

$$\frac{d\sigma}{dt} = \sum_k \frac{\beta_{ak}^2(t)\beta_{bk}^2(t)}{16\pi} s^{2\alpha_k(t)-2}\,. \tag{2.62}$$

The optical theorem relates total cross section to scattering amplitude

$$\sigma = \frac{4\pi}{k}\mathrm{Im}\left[\mathrm{S}(0)\right]\,, \tag{2.63}$$

where Im [S] denotes imaginary part of S and k denotes wave vector of the incident wave. This theorem can be used in total cross section determination

$$\sigma = \sum_k \beta_{ak}(0)\beta_{bk}(0)s^{\alpha_k(0)-1}\,. \tag{2.64}$$

Regge phenomenology based only on meson trajectories is not able to reproduce the rise of the total cross section in high centre of mass energy region. In order to solve this problem a trajectory corresponding to particle with vacuum quantum numbers was introduced [16]. This trajectory is called pomeron. The pomeron trajectory is parametrised [17, 18]

$$\alpha_{\mathbb{P}} = 1.08 + 0.25\ \mathrm{GeV}^{-2} \times t\,. \tag{2.65}$$

Processes with pomeron exchange are diffractive.

2.3.3 Hard Diffraction

In diffraction also hard scale can be present. UA8 collaboration was the first to confirm it. Jets with high transverse energy were observed already in 1988 in diffractive proton-antiproton interaction on SPS accelerator [19].

The hard scale observed by UA8 experiment comes from the process with soft component. The soft component is responsible for rapidity gap creation. This soft component is modified by the typical QCD evolution. This type of processes is expected to be described by the model of Ingelman-Schlein type [20]. In these models, soft component is hidden in diffractive parton distribution functions.

Rapidity gap, however, can also be created in hard regime that is describable in perturbative QCD. These processes can be observed in diffractive lepton-proton deep inelastic scattering. Two types of such interactions are expected to be of this nature:

- exclusive vector meson production [21],
- exclusive dijet production [22] and diffractive heavy flavour production [23],
- large t diffractive inclusive vector meson production [24].

2.3.4 Diffractive Deep Inelastic Scattering (DDIS)

Diffractive dissociation in lepton-proton interaction was predicted in 1971 by Bjorken [25]. This process is in principle diffractive scattering of virtual photon, emitted by the lepton, off proton. Kinematic description of the DDIS process differs from non-diffractive one, because particle that mediates the interaction is assumed to have internal structure.

Kinematics

Schema of deep inelastic scattering is presented in fig. 2.1 on page 3. Diffractive interaction occurs when pomeron mediates the interaction. In resolved pomeron approach it means that the internal structure of the pomeron has to be taken into account. The complete description of the interaction requires introduction of new variables. In this paragraph the interpretation of the new kinematic variables is based on the resolved pomeron model. However, their definitions are general and can be used also with other models, although the interpretation of the information that they convey can be different.

First new variable is a fraction of the incoming proton momentum carried by the pomeron. The variable is denoted as $x_{\mathbb{P}}$ and is expressed in terms of virtual photon, incoming and scattered proton momenta

$$x_{\mathbb{P}} := \frac{\mathbf{q}\,(\mathbf{P} - \mathbf{P}')}{\mathbf{qP}}\,. \tag{2.66}$$

Mass of the hadronic system h produced in deep inelastic scattering equals

$$M^2 = (\mathbf{q} + \mathbf{P} - \mathbf{P}')^2\,. \tag{2.67}$$

Hadronic system mass, definition of W eq. 2.6 on page 4 and definition of t eq. 2.21 on page 5 can be used to calculate $x_{\mathbb{P}}$. From the definition eq. 2.66 directly follows that

$$x_{\mathbb{P}} = \frac{M^2 + Q^2 - t}{W^2 + Q^2 - m_p}\,. \tag{2.68}$$

In approximation of small momentum transfer at proton vertex, which holds for diffractive DIS scattering ($Q^2 \gg t$), the above formula can be simplified

$$x_{\mathbb{P}} \approx \frac{M^2 + Q^2}{W^2 + Q^2}\,. \tag{2.69}$$

Another variable that is introduced in diffractive deep inelastic scattering is fraction of pomeron momentum carried by the interacting parton

$$\beta := \frac{Q^2}{2\mathbf{q}\,(\mathbf{P} - \mathbf{P}')}\,. \tag{2.70}$$

It can also be expressed in terms of M (eq. 2.67 on the preceding page)

$$\beta = \frac{Q^2}{M^2 + Q^2 - t}\,. \tag{2.71}$$

In diffractive DIS ($Q^2 \gg t$) the formula takes the form

$$\beta \approx \frac{Q^2}{Q^2 + M^2}\,. \tag{2.72}$$

It is worth noting that β is an analogue of Bjorken x, but with respect to pomeron instead of incoming proton.

It can be observed that product of the newly introduced variables $x_{\mathbb{P}}$ and β equals Bjorken variable x

$$x_{\mathbb{P}}\beta = \frac{\mathbf{q}\,(\mathbf{P} - \mathbf{P}')}{\mathbf{qP}} \frac{Q^2}{2\mathbf{q}\,(\mathbf{P} - \mathbf{P}')} = \frac{Q^2}{2\mathbf{qP}} = x\,. \tag{2.73}$$

This result is in agreement with interpretation of the variables in the resolved pomeron model. Bjorken x is a fraction of incoming proton momentum carried by the interacting parton, which is equal to the fraction of momentum carried by the pomeron and fraction of pomeron momentum carried by the interacting parton. The above equation shows that Bjorken x and $x_{\mathbb{P}}$ are related. In the approximation of low momentum transfer at proton vertex eq. 2.72 the relation is as follows

$$x_{\mathbb{P}} \approx x \frac{Q^2 + M^2}{Q^2} \tag{2.74}$$

or

$$x \approx x_{\mathbb{P}} \frac{Q^2}{Q^2 + M^2}\,. \tag{2.75}$$

2.4 Diffractive Dijet Production in DIS

Dijet production in diffractive interactions is interesting, because large jet transverse momentum introduce hard scale, that allows for perturbative calculations. Most commonly considered channels of diffractive dijet production in lepton-proton interactions are QCD Compton, boson gluon fusion (single gluon exchange) and two gluons exchange. The first two process describe dijet production in the context of resolved pomeron. QCD Compton process is important for high values of Q^2, thus this process is not taken into account in this analysis. In kinematic region of $Q^2 < 500$ GeV^2 dominates BGF [26]

Symbols and relations used in calculations in the following subsections:

$\mathbf{e}_x = (0,1,0,0)$	X polarisation vector,
$\mathbf{e}_y = (0,0,1,0)$	Y polarisation vector,
$\mathbf{p}_{\perp,q} = p_{t,q}\left(\mathbf{e}_x \cos\phi_q + \mathbf{e}_y \sin\phi_q\right)$	vector of quark transverse momentum,
$\mathbf{q}' = \mathbf{q} + x\mathbf{P}$	sum of virtual photon and interacting parton four-momenta,
$\alpha_{l,q} : \mathbf{V}' = \alpha_{l,q}\mathbf{q}' + \frac{p_{t,q}^2}{2\alpha_{l,q}\mathbf{P}\mathbf{q}'}\mathbf{P} + \mathbf{p}_{\perp,q}$	$\alpha_{l,q}$ is quark longitudinal momentum fraction according to Sudakov decomposition,
$M^2 = \left(\mathbf{q} + x_{\mathbb{P}}\mathbf{P}\right)^2$	mass of hadronic system expressed in terms of virtual photon and incoming proton four-momenta,
$p_{t,q}^2 = \alpha_{l,q}\left(1 - \alpha_{l,q}\right) M^2$	quark transverse momentum expressed in terms of hadronic system mass and longitudinal momentum fraction.

Cross section calculations are done in virtual photon-pomeron centre of mass frame. Z axis is defined by the virtual photon momentum. XZ plane is spanned by the incoming and scattered lepton momenta. Calculations are focused on parton azimuthal angular distributions. The azimuthal angle is the angle between lepton and parton plane. The visualisation is shown in fig. 2.5.

Calculations are restricted to the forward direction $t = 0$ and virtual photon is taken to be linearly polarised in the transverse direction.

2.4.1 Boson Gluon Fusion (BGF)

In boson gluon fusion process, fusion of the virtual photon, originating from the lepton, with a gluon produce a quark-antiquark pair. In this interaction a single gluon is exchanged. A diagram of this interaction is shown in fig. 2.6 on the next page.

Cross section of quark-antiquark pair production which is presented below is taken from [27]. Kinematic region of $W^2 \gg Q^2$ is chosen. In Sudakov decomposition of the gluon four-momentum $\mathbf{l}$ the component along the $\mathbf{q}'$ is negligibly small, thus

$$\mathbf{l} = \alpha_{l,g}\mathbf{P} + \mathbf{p}_{\perp,g}\,, \tag{2.76}$$

with

$$\alpha_{l,g} = x\left(1 + \frac{W^2}{Q^2}\right) \tag{2.77}$$

and gluon polarisation vector $\mathbf{P}\sqrt{2/W^2}$. Ignoring overall constants the shape of the cross section is obtained. Setting virtual photon transverse polarisation to be along X axis, the

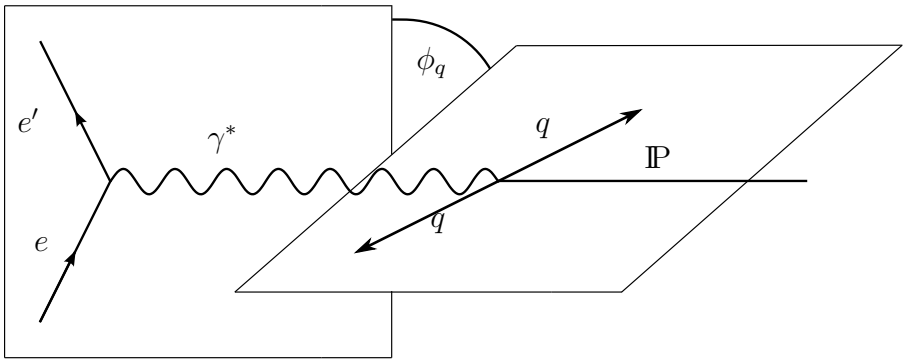

Figure 2.5: Definition of azimuthal angle in virtual photon-pomeron centre of mass system with Z axis along the virtual photon momentum and XZ plane spanned by the incoming and scattered lepton. The angle of interest is angle between lepton and parton plane.

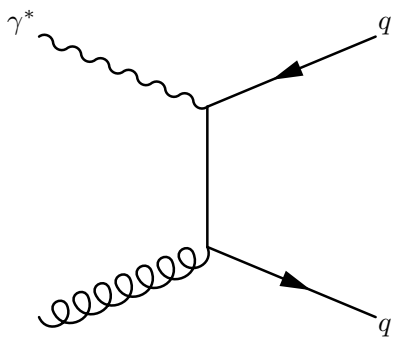

Figure 2.6: Schematic illustration of dijet production in photon-gluon fusion channel $\gamma^* + g \to q + \overline{q}$.

square of the process is obtained

$$\mathbf{e}_x \mathbf{e}_x \mathbf{V}\mathbf{V} - 4\alpha_{l,q}\left(1-\alpha_{l,q}\right)\mathbf{e}_x \mathbf{V} \mathbf{e}_x \mathbf{V}\,. \tag{2.78}$$

Vector $\mathbf{V}$ has the form of a dipole and can be interpreted as the $q\overline{q}$ component of the virtual photon wave function

$$\mathbf{V} = \frac{\mathbf{V}'}{\alpha_{l,q}\left(1-\alpha_{l,q}\right)Q^2 + p_{t,q}^2} - \frac{\mathbf{V}' - \mathbf{l}}{\alpha_{l,q}\left(1-\alpha_{l,q}\right)Q^2 + p_{t,q-g}^2}\,. \tag{2.79}$$

Integrating over gluon azimuthal angle ϕ_g and taking the limit $p_{t,g}^2 \to 0$

$$\int \frac{d\phi_g}{2\pi}\mathbf{V}_i\mathbf{V}_j = \frac{p_{t,g}^2}{2\left(\alpha_{l,q}\left(1-\alpha_{l,q}\right)Q^2 + p_{t,q}^2\right)^2}\left(\delta_{ij} - \mathbf{V'}_i\mathbf{V'}_j\frac{p_{t,q}^2 Q^2}{M^2\left(\alpha_{l,q}\left(1-\alpha_{l,q}\right)Q^2 + p_{t,q}^2\right)^2}\right)\,. \tag{2.80}$$

Thus cross section is proportional to

$$d\sigma \propto \left(1 - 2\frac{p_{t,q}^2}{M^2}\right)\frac{(Q^2)^2 + M^4}{\left(Q^2+M^2\right)^2} + 4\frac{p_{t,q}^2}{M^2}\cos\left(2\phi_q\right)\frac{Q^2M^2}{\left(Q^2+M^2\right)^2}\,. \tag{2.81}$$

It is worth noting that the coefficient in front of $\cos\left(2\phi_q\right)$ is positive, so quarks are preferably produced in the lepton plane.

Several models use boson gluon fusion channel to explain dijet production. One of the most commonly used is resolved pomeron model, which is the default model in RAPGAP MC generator [28]. Other model that is using this channel is Soft Colour Interaction model [29].

Resolved Pomeron Model

The presence of hard scale, that allows for use of perturbative QCD, and the assumption that pomeron is a composite particle lead to a model of resolved pomeron based on Ingelman and Schlein model [20]. In this model Regge factorisation is assumed. It means that diffractive interaction can be split into two steps independent of each other. Firstly, pomeron is emitted from the proton. Secondly, a parton from the pomeron interacts with virtual photon.

Cross section calculations in resolved pomeron model are similar to non-diffractive deep inelastic scattering cross section. The difference is that dependence on diffractive variables is added and diffractive structure functions are used

$$\frac{d^4\sigma^{\mathrm{D}}}{dx_{\mathbb{P}}dtdQ^2d\beta} = \frac{2\pi\alpha^2}{xQ^2}\left[\left(1+(1-y)^2\right)F_2^{\mathrm{D}}\left(\beta,Q^2,t,x_{\mathbb{P}}\right) - y^2F_L^{\mathrm{D}}\left(\beta,Q^2,t,x_{\mathbb{P}}\right)\right]\,. \tag{2.82}$$

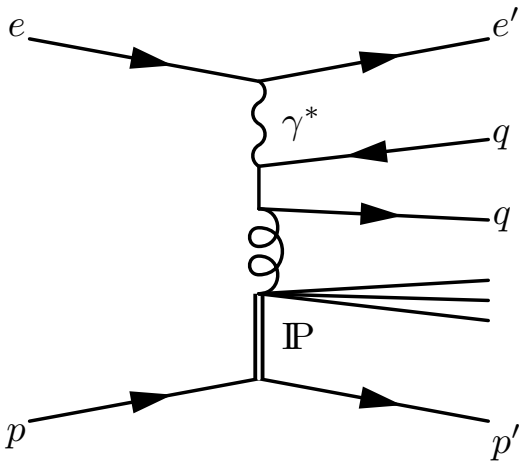

Figure 2.7: Schematic illustration of dijet production in resolved pomeron model via photon-gluon fusion.

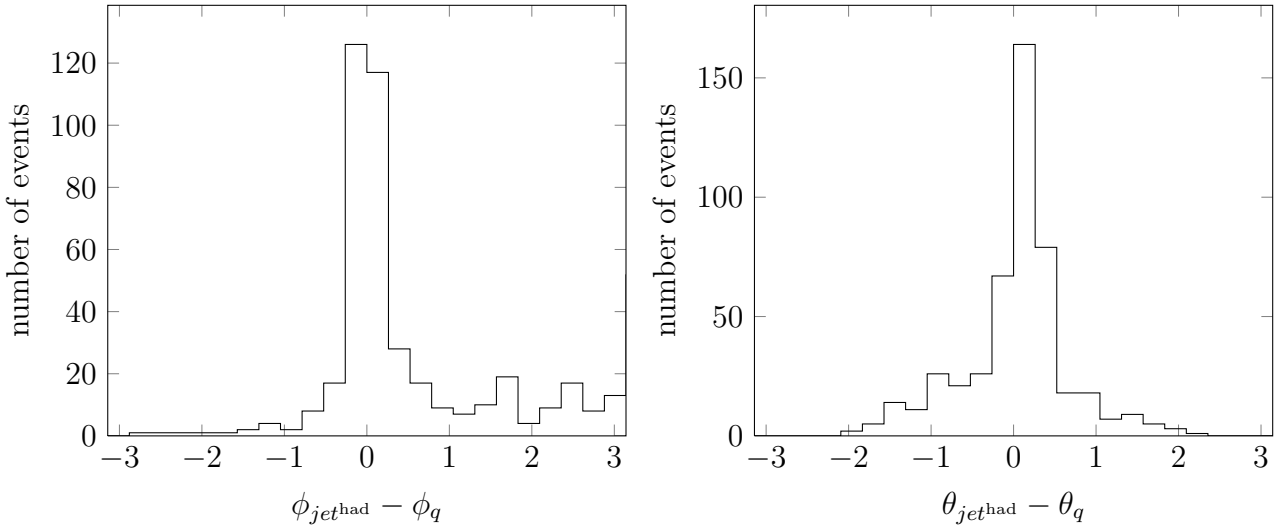

Figure 2.8: Resolution of azimuthal and polar angles of quark or antiquark reconstructed with exclusive jet.

F_2^{D} and F_L^{D} are diffractive structure functions. Assuming Regge factorisation, F_2^{D} can be split into

$$F_2^{\mathrm{D}} = f\left(t, x_{\mathbb{P}}\right) F_2^{\mathbb{P}}\left(\beta, Q^2\right) , \tag{2.83}$$

where $F_2^{\mathbb{P}}$ is pomeron structure function and f is pomeron flux. Diffractive parton densities are expected to satisfy the DGLAP evolution equation. The most popular parametrisation, which is set as default in RAPGAP MC generator [28] is H1 parametrisation [30].

A schema of diffractive dijet production in deep inelastic scattering seen from the point of view of resolved pomeron model is presented in fig. 2.7. Since only one gluon is exchanged, a pomeron remnant is present. The shape of the event is determined by the quark-antiquark pair. The remnant introduces only some distortion. It has been verified by the studies of quark momentum reconstruction with exclusive jets. The results obtained from BGF MC (see sec. 4.1 on page 29) in the kinematic region used in this analysis (see eq. 7.9 to eq. 7.14 on page 64)are presented in fig. 2.8.

Soft Colour Interactions

Soft Colour Interactions (SCI) [31] model is an alternative to resolved pomeron. It starts from perturbative QCD calculations and adds soft gluons that does not change the momenta of the partons, but change colour ordering. The colour structure may be changed in such a way, that standard hadronisation procedures produce rapidity gaps. The additional gluons are supposed to reproduce soft interactions between perturbatively produced partons and the colour medium of the proton.

In the very basic model, one parameter R is used. This parameter represents the probability of soft interaction, which boils down to colour change between two partons. Statistical nature of the number of soft interaction per event can lead in some cases to rapidity gap production, via standard hadronisation processes.

2.4.2 Two Gluon Exchange

Two gluon exchange channel models diffractive interaction as an exchange of a colour singlet consisting of two gluons. The singlet couples to the hadronic state into which virtual photon fluctuates. The simplest realisation of the hadronic system is quark-antiquark pair, which results in dijet production in diffractive dissociation of the virtual photon. A more complex system consists of a quark, antiquark and gluon. Mentioned above processes are schematically presented in fig. 2.9 on the facing page.

Dijet production via two gluon exchange in the leading order is realised with four diagrams shown in fig. 2.10 on the next page. Cross section calculations in the leading-log presented below are taken from [27]. Process amplitude is expressed with unintegrated gluon distribution of proton using k-factorisation theorem [32]. It is assumed that $s \gg Q^2$. Virtual photon polarisation is put along the X axis. The square of the process $\gamma^* + 2g \to q + \overline{q}$ amplitude can be expressed with momenta of both gluons $\mathbf{l}$ and $\mathbf{l}'$

$$\mathbf{e}_x \mathbf{e}_x \mathbf{V}_D(\mathbf{l})\, \mathbf{V}_D(\mathbf{l}') - 4\alpha_{l,q}(1-\alpha_{l,q})\, \mathbf{e}_x \mathbf{V}_D(\mathbf{l})\, \mathbf{e}_x \mathbf{V}_D(\mathbf{l}') \ , \tag{2.84}$$

with

$$\mathbf{V}_D(\mathbf{l}) = 2\frac{\mathbf{V}'}{\alpha_{l,q}(1-\alpha_{l,q})Q^2 + p_{t,q}^2} - \frac{\mathbf{V}'-\mathbf{l}}{\alpha_{l,q}(1-\alpha_{l,q})Q^2 + p_{t,q-g}^2} - \frac{\mathbf{V}'+\mathbf{l}}{\alpha_{l,q}(1-\alpha_{l,q})Q^2 + p_{t,q+g}^2} \ . \tag{2.85}$$

Integrating over gluon azimuthal angle ϕ_g and taking the limit $p_{t,g}^2 \to 0$ in the leading term

$$\int \frac{d\phi_g}{2\pi} \mathbf{V}_D(\mathbf{l}) = \mathbf{V}' \frac{4Q^2M^4}{\left(Q^2+M^2\right)^3} \frac{p_{t,g}^2}{p_{t,q}^4} \left(1 + \mathcal{O}\left(p_{t,g}^2\right)\right) \ . \tag{2.86}$$

The integration is done independently for each gluon. The cross section for the transversely polarised photon is in the form of

$$d\sigma \propto 1 - 2\frac{p_{t,q}^2}{M^2 - 2p_{t,q}^2} \cos(2\phi_q) \ . \tag{2.87}$$

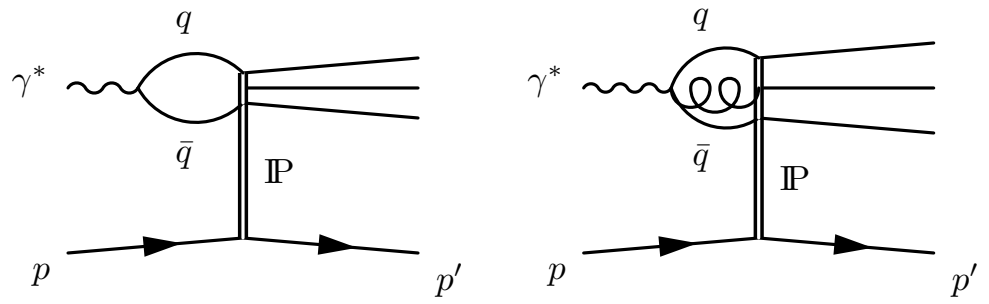

Figure 2.9: Diffractive deep inelastic scattering in proton rest frame. In this frame the photon fluctuates into hadronic state. In the left graph the photon fluctuates into $q\bar{q}$ system, in the right graph into $q\bar{q}g$ system.

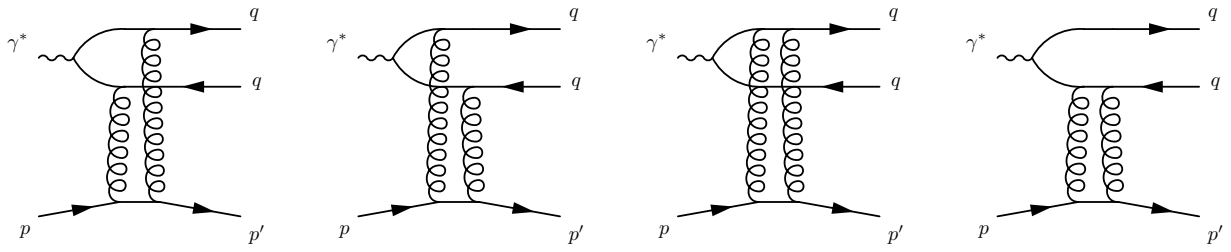

Figure 2.10: Diagrams contributing to dijet production via two-gluon exchange.

To get the full cross section all polarisations have to be taken into account. This results in

$$\frac{d\sigma^{\mathrm{D}}}{dydQ^2dM^2dp_{t,q}^2d\phi_q dt_{|t=0}} = \frac{\alpha}{yQ^2\pi}\Bigg[\frac{1+(1-y)^2}{2} \frac{d\sigma_T^{\mathrm{D}}}{dM^2p_{t,q}^2t_{|t=0}} - 2\,(1-y)\,\frac{p_{t,q}^2}{M^2-2p_{t,q}^2}\cos\left(2\phi_q\right) \frac{d\sigma_T^{\mathrm{D}}}{dM^2p_{t,q}^2t_{|t=0}} + (1-y) \frac{d\sigma_L^{\mathrm{D}}}{dM^2p_{t,q}^2t_{|t=0}} + (2-y)\sqrt{1-y}\cos\left(\phi_q\right) \frac{d\sigma_I^{\mathrm{D}}}{dM^2p_{t,q}^2t_{|t=0}}\Bigg]. \quad (2.88)$$

Calculations of exclusive diffractive dijet production in DIS are also calculated using collinear factorisation. Calculations and result are presented in [33]. Of course the form of the cross section is the same as in eq. 2.88

$$\frac{d\sigma^{\mathrm{D}}}{dydQ^2} = \frac{\alpha}{yQ^2\pi}\Bigg[\frac{1+(1-y)^2}{2}d\sigma_T^{\mathrm{D}} - 2\,(1-y)\cos\left(2\phi_q\right)d\sigma_{TT}^{\mathrm{D}} + (1-y)\,d\sigma_L^{\mathrm{D}} + (2-y)\sqrt{1-y}\cos\left(\phi_q\right)d\sigma_I^{\mathrm{D}}\Bigg]. \quad (2.89)$$

Calculations and discussion of a three parton final state ($q\bar{q}g$) is available in [34]. The calculations are done in the leading $\log\left(Q^2\right)$ and leading $\log\left(M^2\right)$. Calculations show that the gluon is preferably emitted in the pomeron direction forming a jet. Second jet is formed by the quark-antiquark pair. Only in small fraction of events the gluon is emitted perpendicular to the photon-pomeron axis and three jets are reconstructed. It turns out that three parton hadronic state significantly contributes to dijet cross section.

Models that use this channel in dijet production are e.g. dipole models, purely or half perturbative ones.

BEKW Model

Model suggested by J. Bartels, J. Ellis, H. Kowalski and M. Wüsthoff [1] tries to extrapolate perturbative calculations to soft region. It is done by assuming special forms of virtual photon wave function and proton diffractive structure functions parametrisation. The diffractive structure function F_2^{D} consist of four terms, taking into account twist four

$$F_2^{\mathrm{D}} = F_{q\bar{q}}^T + F_{q\bar{q}g}^T + \Delta F_{q\bar{q}}^L + \Delta F_{q\bar{q}}^T . \tag{2.90}$$

Two first terms are responsible for production of quark-antiquark and quark-antiquark-gluon systems from transversely polarised photons. Third term describes higher twist production of $q\bar{q}$ system from longitudinally polarised photon. The last element corresponds to higher twist production of $q\bar{q}$ system from transversely polarised photon. Contributions to the structure function are assumed to have the following forms

$$F_{q\bar{q}}^T = A\left(\frac{x_0}{x_{\mathbb{P}}}\right)^{n_2} \beta\left(1-\beta\right) , \tag{2.91}$$

$$F_{q\bar{q}g}^T = B\left(\frac{x_0}{x_{\mathbb{P}}}\right)^{n_2} \alpha_s \ln\left(\frac{Q^2}{Q_0^2}+1\right)\left(1-\beta\right)^{\gamma} , \tag{2.92}$$

$$\Delta F_{q\bar{q}}^L = C\left(\frac{x_0}{x_{\mathbb{P}}}\right)^{n_4} \frac{Q_0^2}{Q^2}\left[\ln\left(\frac{Q^2}{4Q^2\beta}+1.75\right)\right]^2 \beta^3\left(1-2\beta\right)^2 , \tag{2.93}$$

$$\Delta F_{q\bar{q}}^T = D\left(\frac{x_0}{x_{\mathbb{P}}}\right)^{n_4} \frac{Q_0^2}{Q^2} \ln\left(\frac{Q^2}{4Q^2\beta}+1.75\right)\beta^3\left(1-\beta\right) . \tag{2.94}$$

A Consequence of the above parametrisation is that $q\bar{q}$ the contribution from the transversely polarised photon dominate in the region of average β values. This contribution vanishes in the limits of $\beta \to 0$ and $\beta \to 1$. In the region of β approaching 0, $q\bar{q}g$ system dominates. On the other end of β distribution ($\beta \to 1$), the structure function is dominated by the contribution from longitudinal photon $q\bar{q}$ production. A distribution of β split into contributions, obtained from the fit of model parameters to the data gathered by the ZEUS detector in 1994, is presented in fig. 2.11 on the next page.

Saturation Model

The main aim of saturation model [35, 36] is extrapolation of calculations in perturbative kinematic region, to the region of small x and Q^2. In this region perturbative calculations diverge. This problem is overcome by introducing cross section saturation. There are two sources of the saturation. One type of saturation can be observed when photon wavelength ($\lambda_{\gamma^*} \propto 1/\sqrt{Q^2}$) reaches the size of the proton. The other type is observed in small-x region, where parton density is so large that interaction and recombination of partons with themselves saturates the cross section.

The model suggested by Golec-Biernat and Wüsthoff assumes the following form of the cross section

$$\sigma^{\mathrm{D}} = \sigma_0^{\mathrm{D}}\left[1-\exp\left(\frac{r^2}{4R_0^2\left(x\right)}\right)\right] . \tag{2.95}$$

Saturation scale R_0 is x dependent

$$R_0 = \frac{1}{Q_0}\left(\frac{x}{x_0}\right)^{\lambda/2} . \tag{2.96}$$

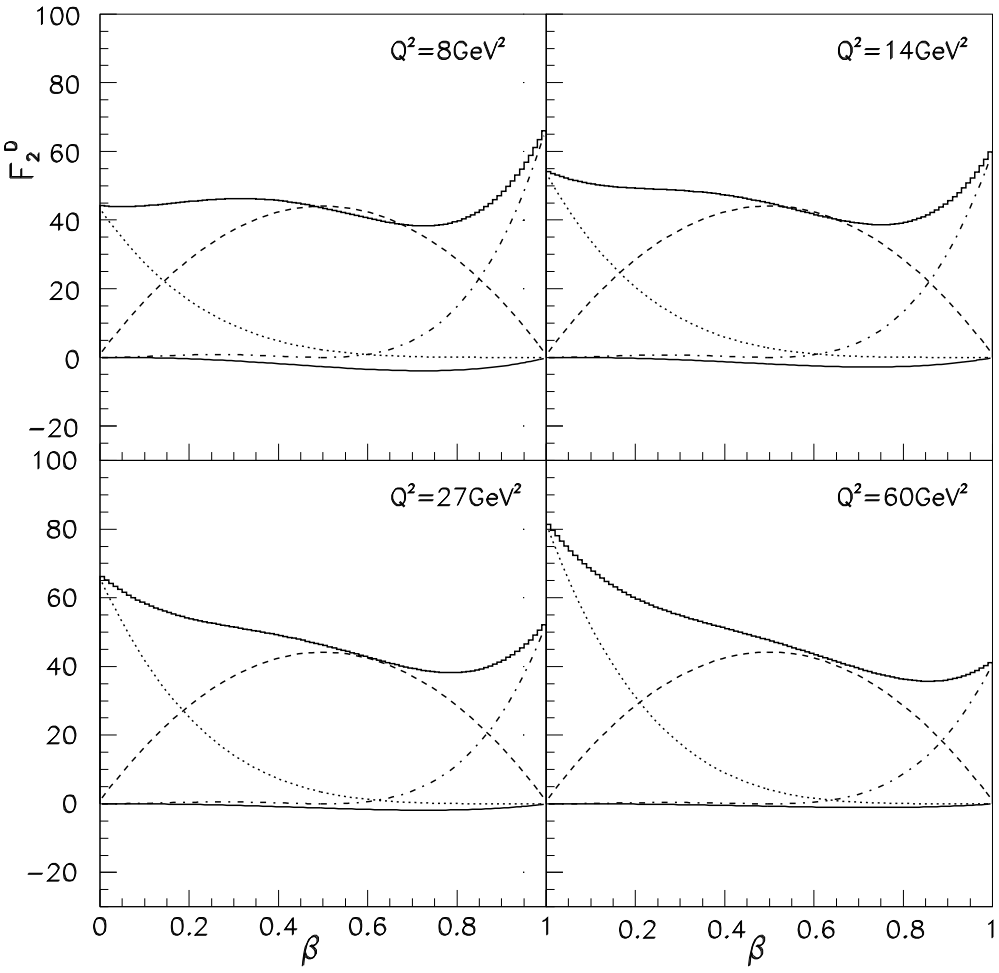

Figure 2.11: Taken from [1]. Distribution of β for fixed $x_{\mathbb{P}} = 0.001$ with BEKW model parameters fit to the ZEUS 1994 data. Upper solid line shows F_2^{D}, dashed line - $F_{q\bar{q}}^T$, dotted line - $F_{q\bar{q}g}^T$, dashed-dotted line - $Flqq$, lower solid line - $\Delta F_{q\bar{q}}^T$.

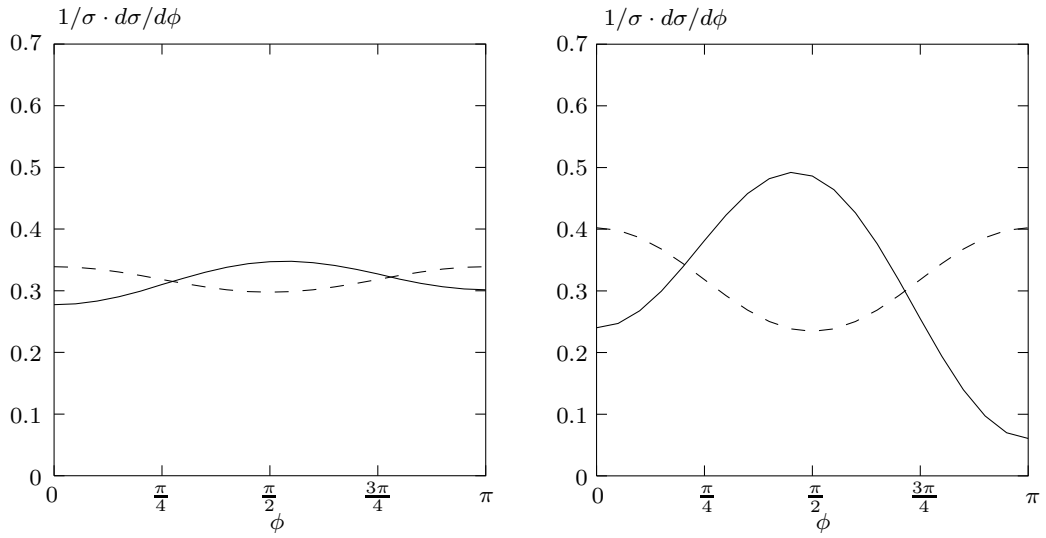

Figure 2.12: Taken from [2]. Distributions of azimuthal angle of parton originating from $q\overline{q}$ system. Distributions are calculated in kinematic region of $Q^2 = 100$ GeV and $p_{t,q}^2 > 5$ GeV^2. Left hand graph shows distribution for $\beta = 1/3$, right hand graph for $\beta = 2/3$. Solid line shows distribution obtained with two gluon exchange, dashed line shows distribution obtained with photon-gluon fusion (single gluon exchange).

One of the important features of this cross section parametrisation is that for small r cross section is proportional to r^2 (colour transparency). The other is that in region of large r the cross section saturates.

2.5 Aim of the Analysis

There is a clear difference in forms of cross sections for a single (eq. 2.81 on page 14) and double (eq. 2.88 on page 17) gluon exchange. When only one gluon is exchanged a contribution from term proportional to $\cos(2\phi_q)$ is positive, while in two gluon case it is negative. Thus the difference between models is expected to be easily observed in azimuthal angular distribution of jets reconstructed in virtual photon-pomeron centre of mass frame. It is enough to measure the shape of the distribution in order to distinguish between the two processes. Results of numerical studies of $q\overline{q}$ production done by H. Lotter [2] are shown in fig. 2.12 on the preceding page. The asymmetry in the distribution for two gluon exchange channel comes from the interference term. This term cancels if contributions from ϕ_q and $\phi_q + \pi$ are added. In measurement it is difficult to distinguish between quark jet and antiquark jet, thus the contributions are added and no asymmetry is expected. A conclusion that can be drawn from the numerical studies is that the larger the β the more pronounced shape of azimuthal angular distribution.

The convex shape of azimuthal angular distributions in two-gluon exchange is caused by the $q\overline{q}$ production from transversely polarised photon. Thus it is desirable to suppress all other contributions.

Contribution from longitudinally polarised photon does not depend on the parton azimuthal angle. This contribution will effectively lower the sensitivity of the measurement, by forming a pedestal. Dijet production originating from transversely polarised photon dominates in high β region (fig. 2.11 on the previous page). It can be suppressed by imposing upper β limit.

As it is presented in sec 2.4.2 on page 16 two parton as well as three parton hadronic systems are measured as dijet events. Thus the contribution from $q\overline{q}g$ has to be suppressed with other, than jet algorithm, means. A way to do it, is to conduct the measurement in high β region, where contribution to cross section from three parton events is small compared to two parton one. Theoretical calculations shown in [33] suggest the selection criterion of $\beta > 0.5$.

The aim of this analysis is experimental verification of photon-gluon fusion and two gluon exchange models by measurement of dijet azimuthal angular distribution. The measurement done in the region of $0.5 < \beta < 0.7$ is expected to provide a clean sample of events originating from $q\overline{q}$ produced by the transversely polarised virtual photon. There have been only one similar analysis [37] done using data gathered by the ZEUS detector in years 1999-2000. The previous analysis is based on dijets with transverse momentum $p_{t,jet} > 1.25$ GeV.

Chapter 3

Experimental Setup

The aim of this thesis is analysis of lepton-proton collision data. Leptons used in collisions were electrons and positrons. In order to measure properties of such interactions at high centre of mass energy, leptons and protons have to be accelerated. This was done in HERA accelerator. The collisions were studied with ZEUS detector. Detector as well as accelerator were part of DESY (Deutsches Elektronen-Synchrotron) research facility, which was founded in Hamburg on 18 December 1959.

3.1 HERA Accelerator

Hadron-Electron Ring Accelerator (HERA) [38] was the the first ring facility storing two different types of particles. HERA was built in seven years starting 1984. The accelerator was built in 6336 m long tunnel in Hamburg. The tunnel was 15–30 m underground.

Accelerating two types of particles that differ in mass more than 1800 times required two separate rings. The rings were placed one over the other. The most demanding was proton ring. With protons accelerated to 820 GeV or even 920 GeV, the use of superconducting magnets was the only possible solution to keep protons in the ring. At the time HERA was planned, there were no operating accelerators using this kind of magnets. In total 650 magnets, each producing a magnetic field of approximately 4.7 T and operating in temperature of 4.4 K, were used in the proton ring.

Particles were accelerated in several stages. Linear accelerator was used to boost negative hydrogen ions (H^-) to energy of 50 MeV and electrons to energy of 500 MeV. Next, electrons were injected subsequently into two other accelerators: DESY II, where the exit energy was 7.5 GeV and to PETRA II, where the energy was 12 GeV. Such electrons were ready to be injected to HERA ring, where they gained nominal energy of 27.5 GeV. Negative hydrogen ions were stripped off of electrons and accelerated to energy of 7.5 GeV by DESY III accelerator. Next, storage ring PETRA boosted protons to 40 GeV. These protons were used to fill HERA storage ring. In the end protons obtained energy of 820 GeV until year 1998 and 920 GeV afterwards.

Lepton and proton beams consisted of 220 bunches. The separation between bunches was equal 96 ns which was equivalent to 29 m. At least 10 bunches were left empty for control measurements. Each bunch was filled with about 10^{10} particles.

HERA operation, which lasted 15 years (from 1992 till 2007), is usually split into two stages: HERA I and HERA II. In the beginning of the first stage protons of energy 820 GeV were collided with leptons of 26.7 GeV energy. In 1994 lepton beam energy was increased to 27.5 GeV. Proton beam energy reached 920 GeV in 1998. This yield centre of mass energy of 318 GeV. The first period of HERA operation ended in year 2000. In this period the

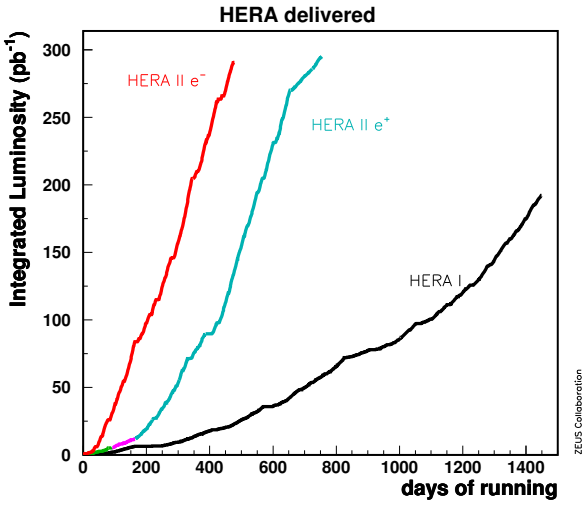

Figure 3.1: Integrated luminosity delivered by the HERA accelerator. HERA II luminosity is split to electron and positron contributions.

accelerator delivered 193 pb^{-1} integrated luminosity. The accelerator was upgraded in years 2000-2003. In 2003 it was again put to operation starting the second phase called HERA II. Upgrades increased delivered luminosity by a factor of five. The energies remained unchanged. Luminosity delivered by HERA I and HERA II as a function of days of running is presented in fig. 3.1. At the end of HERA operation proton beam energy was lowered in order to allow for measurement of the longitudinal structure function. Protons of 460 GeV and 575 GeV were used in these runs, which are called Low Energy Runs (LER) and Medium Energy Runs (MER).

Four detectors used beams delivered by HERA. The detectors were placed in four separate halls. A schema of the accelerator and position of the halls is presented in fig. 3.2 on the facing page. General purpose detectors H1 and ZEUS started operation in 1992. In 1995 HERMES detector begun operation. It used only lepton beam that was directed onto a target built of protons or neutrons. The main purpose of the HERMES detector was investigation of proton spin structure. In years 1999-2003 HERA-B experiment used proton beam colliding with aluminium or copper target. Proton-nucleus collisions were used to investigate B mesons physics.

3.2 ZEUS Detector

The ZEUS detector [39, 40] was placed in the south hall. It was general purpose detector optimised for electron(positron)-proton collisions. Since proton beam energy was much larger than lepton beam, the centre of mass system followed the proton beam direction. This means that most of the particles emerging from the interaction were produced in the forward direction. Thus the ZEUS detector had been built asymmetric. In this section only detector components important to this analysis are described.

Commonly used coordinate system in the ZEUS collaboration is orthogonal and dextrogyratory. The origin is placed in a nominal interaction point. Z axis is parallel to the beam lines and pointed in the same direction as incoming proton momenta. Y axis is pointing up. X axis is pointing to the centre of the accelerator. Polar angle is measured from the Z axis, azimuthal angle - from the X axis. The coordinate system is presented in fig. 3.3 on the next page.

Schemata of the ZEUS detector cross sections are presented in fig. 3.4 on page 24 and fig. 3.5 on page 25. One of the most important detector component was uranium calorimeter (CAL). It precisely measured energy and direction of particles and their clusters. In order to increase the

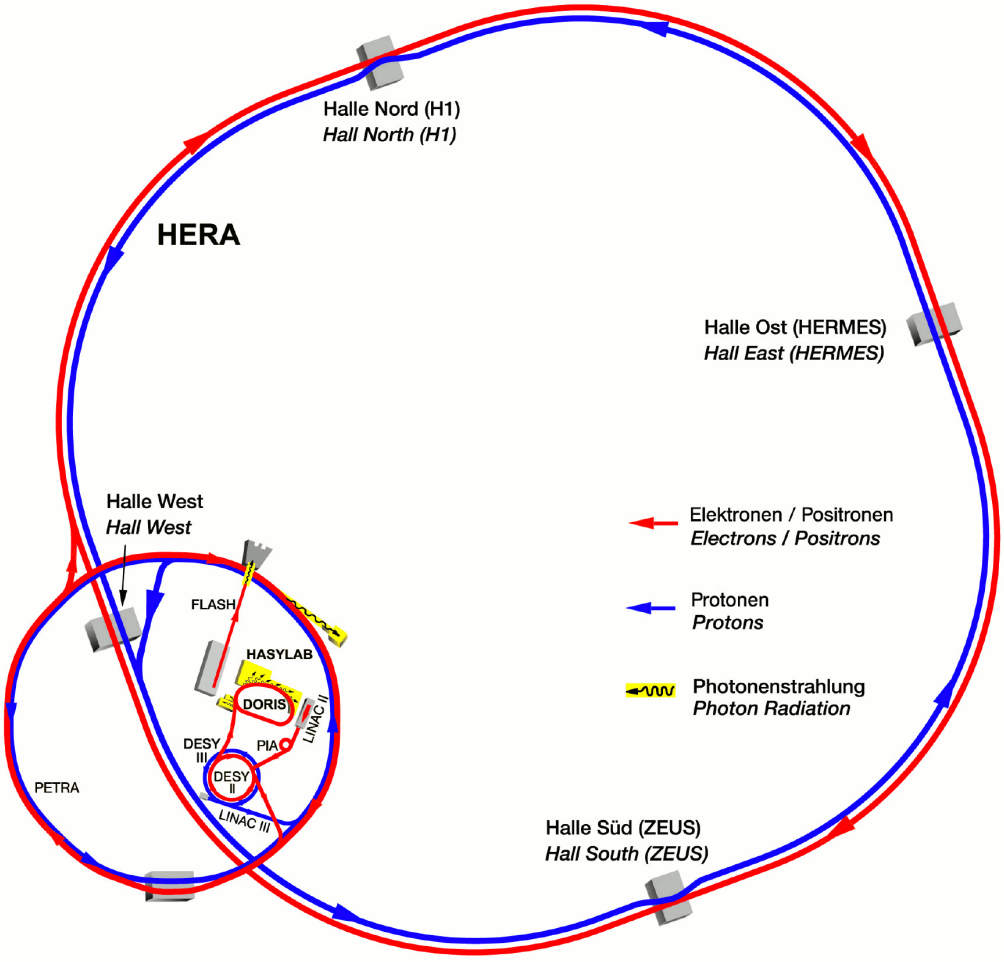

Figure 3.2: A schema of HERA accelerator and position of experiments.

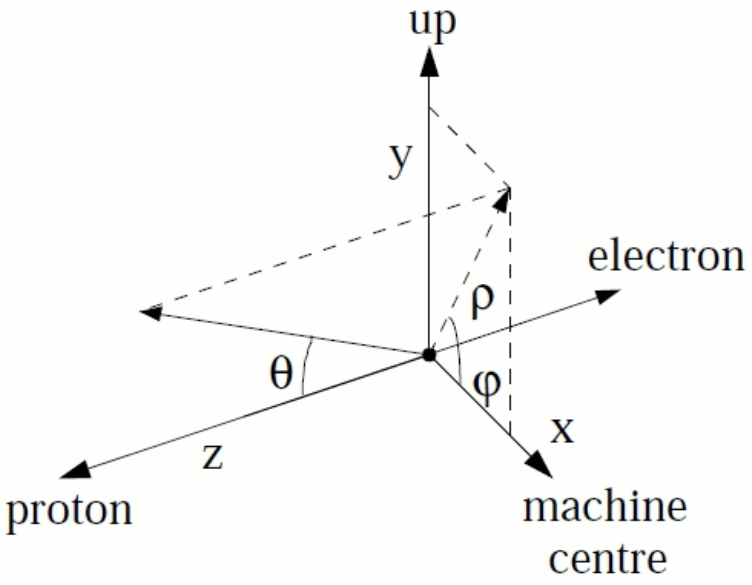

Figure 3.3: Coordinate system used in the ZEUS collaboration.

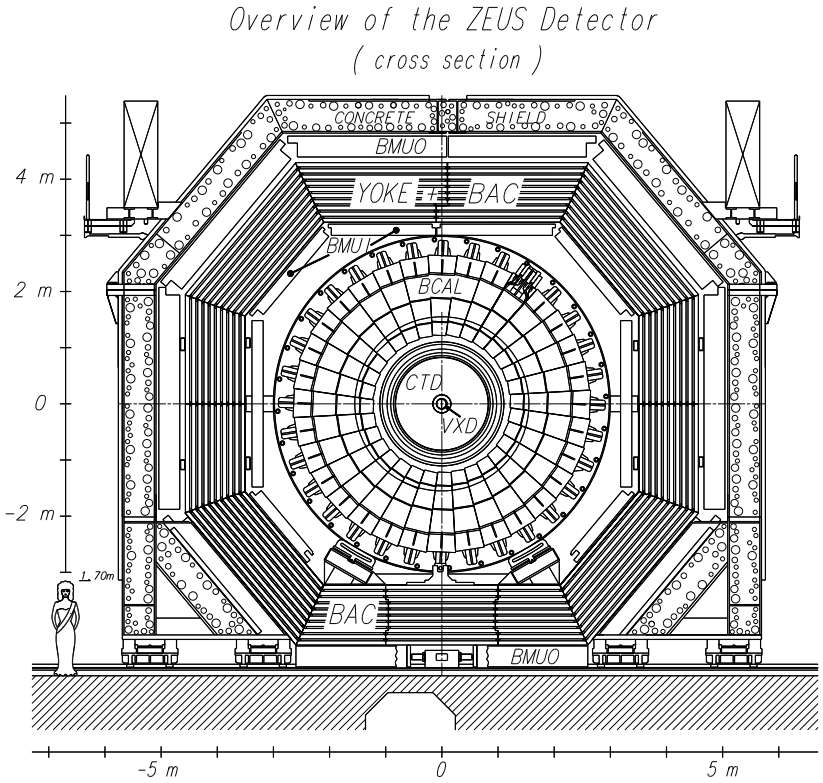

Figure 3.4: Schema of the ZEUS detector XY cross section.

Table 3.1: Acceptance of each calorimeter part in terms of polar angle and pseudorapidity.

	θ [deg]	η
FCAL	1.6 – 36.7	1.10 – 4.27
BCAL	36.7 – 129.1	-0.74 – 1.10
RCAL	129.1 – 177.4	-3.82 – -0.74

precision of the measurement a backing calorimeter had been installed. It was used to measure the energy of particles that were not stopped by the main calorimeter. Charged particles tracks were reconstructed with several tracking detectors: central tracking detector (CTD) and silicon microvertex detector (MVD). Magnetic field present in the detector allowed for momentum measurement. A separate detector called MUON was used to measure muons. It was built of limited streamer tubes.

3.2.1 Uranium Calorimeter

The calorimeter was split into three parts: forward (FCAL), barrel (BCAL) and backward (BCAL). All parts covered 99.8 % of solid angle in the front and 99.5 % in the back. Acceptance of each calorimeter part in terms of polar angle and pseudorapidity is presented in tab. 3.1.

Each part of the calorimeter was built of towers divided into electromagnetic and hadronic sections. Transverse dimensions of a section were as follows: front calorimeter — 5 cm $\times$ 20 cm, barrel calorimeter — 5 cm $\times$ 24 cm, rear calorimeter — 10 cm $\times$ 20 cm. The electromagnetic section covered about 25 radiation lengths. The total absorption length varied starting from 4 (RCAL), via 5 (BCAL) to 7 (FCAL) interaction lengths. Calorimeter sections were built of absorbent–scintillator sandwiches. The active layer was 2.6 mm thick, the absorbent layer was 3.3 mm thick. These values had been chosen so that the ratio of energy deposited by electrons and hadrons was one ($e/h = 1.00 \pm 0.02$). Scintillator signal was channelled to photomultipliers

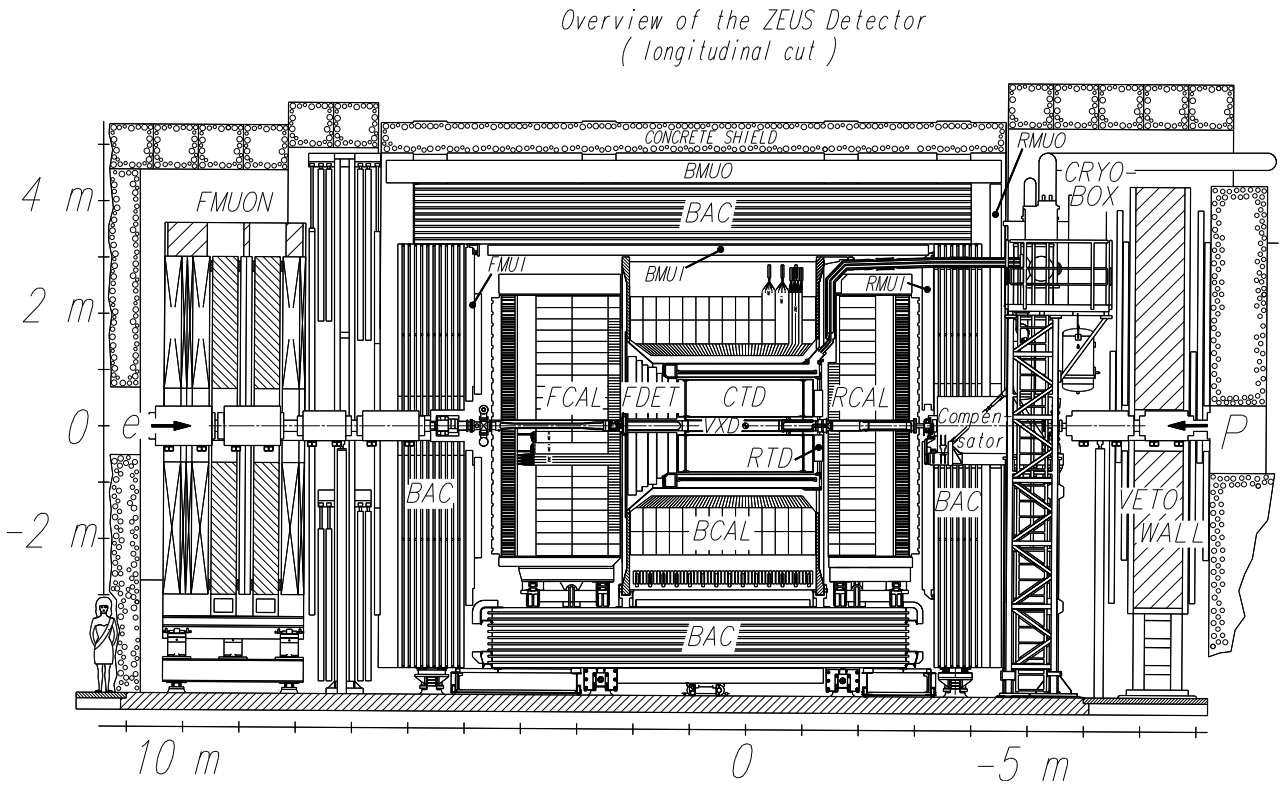

Figure 3.5: Schema of the ZEUS detector XZ cross section.

with the help of optical fibres. Depleted uranium was used as the absorbent. Thickness of one absorbent layer corresponded to one radiation length. Depleted uranium absorber allowed for $e/h = 1$ while keeping good energy resolution. Uranium atoms in the absorber were fissioned by particles produced in the interaction. Released energy compensated for the energy lost in the absorber. Natural radioactivity of the uranium was used for calibration. Each absorber was wrapped in metal foil to lower the natural uranium radioactivity background. The thickness of the foil was 0.2 mm for electromagnetic part and 0.4 mm for hadronic section.

The calorimeter was designed in such way that 90 % of the particles deposited at least 95 % of their energy. The calorimeter signal was processed in 1 ns. High spatial resolution enabled lepton identification based on shower shape. Hadron initiated cascades were measured with angular resolution of 10 mrad. The following relative energy resolution were obtained for hadrons and electrons respectively[1]

$$\frac{\sigma_h}{E} = \frac{0.35}{\sqrt{E\ [\mathrm{GeV}]}} \oplus 1\,\%\,, \tag{3.1}$$

$$\frac{\sigma_e}{E} = \frac{0.18}{\sqrt{E\ [\mathrm{GeV}]}} \oplus 2\,\%\,. \tag{3.2}$$

3.2.2 Tracking detectors

Central tracking detector was built of wire chamber. The wires were grouped in 9 sections. The wires had been positioned such, that azimuthal and polar angular resolutions were equal and reached 200 mrad. This allowed for track transverse momentum reconstruction with the following resolution

$$\frac{\sigma\,(p_{t,})}{p_{t,}} = 0.0058 p_{t,}\ [\mathrm{GeV}] \oplus 0.0065 \oplus \frac{0.0014}{p_{t,}\ [\mathrm{GeV}]}\,. \tag{3.3}$$

[1] $a \oplus b = \sqrt{a^2 + b^2}$

The active part of the chamber was limited by radii of 18.2 cm and 79.4 cm. The chamber was 205 cm long. It spanned in Z axis from -100 cm to 105 cm. At least 12 layers of wires were required to provide signal simultaneously. The CTD covered polar angles $15^\circ < \theta < 165^\circ$.

Micro vertex detector (MVD) [41] was installed in the ZEUS detector during 2000–2001 upgrade. This tracking detector was divided into forward and barrel part. The latter was about 65 cm long. It was built of three layers of silicon strip sensors. Each layer consisted of two planes of single sided silicon strip detectors. A readout cell, of 123.68×64.24 mm^2 surface, was connected to 512 channels. A spatial resolution of 13 µm was achieved for perpendicular tracks.

3.2.3 Luminosity Monitor

Bremsstrahlung was used in luminosity measurement. In proton electric field, electrons radiated a photon $e + p \to e + p + \gamma$. A coincidence of photon and scattered lepton was required.

Both the lepton and the photon were observed at very small angles. Luminosity detectors were placed close to the beam pipe. The main photon detector was placed 107 m away from the nominal interaction point. It was a sampling calorimeter, consisting of lead-scintillator layers with position detector. Photons entered the detector through a copper-beryllium window. Behind the window was a coal filter, which was screening the detector from synchrotron radiation.

Electron detector was placed 35 m away from the nominal interaction point. Leptons entered sampling calorimeter (lead-scintillator) through stainless steel window.

3.2.4 Trigger

Bunches in HERA accelerator (see sec. 3.1 on page 21) were crossed every 96 ns. It resulted in events rate of about 10.4 MHz. ZEUS event recording rate was about 1 Hz. A three level trigger [42] was used to reduce accelerator delivered event rate to amount possible to save.

Apart from decreasing the number of events to save, trigger was required to accept significant fraction of events interesting from the physical point of view.

First Level Trigger (FLT)

The first level trigger [43, 4] reduced event rate below 1 kHz. It was a part of every component of the detector. Only coarse analog information was used to produce component-based event information. The information was prepared in 2 µs. Then it was sent to the global first level trigger (GFLT). GFLT decided whether the event was accepted and sent appropriate signal to detector components with 4.6 µs. During this time the full analog data of a component was stored in the local buffer. In the case of event rejection the data was deleted. Otherwise the data was digitised.

Fast Clear (FC)

Parallel to the data digitisation, the calorimeter data is reprocessed with a cluster algorithm. Main calorimeter components (FCAL, BCAL, RCAL) are processed simultaneously by fast clear processors. FC decision had been reached in 50 µs i.e. before digitisation was completed. When event was accepted, the data was written to the data stream by fast clear. Otherwise an abort signal was sent to all detector components.

Second Level Trigger (SLT)

Digitised data was processed by the second level trigger [44, 45, 46]. Digitisation allowed higher accuracy calculations to be done. Component-based event information was sent in 5 ms to the global second level trigger (GSLT), which took the decision (in 3 ms) if event should be further processed. Meanwhile the full data had been stored in asynchronous pipeline capable of storing up to 15 events. This stage reduced event rate to less than 100 Hz.

Event Builder

An event that has passed the second level trigger was build with the help of the ZEUS event builder [47]. This means that information from all components was gathered. The full raw event was translated into ADAMO [48, 49] format. The data in ADAMO format was an input to the third level trigger.

Third Level Trigger (TLT)

The third level trigger [50, 51], with the use of a farm of Silicon Graphics computers, made event selection based on offline code. Offline-like analysis information was available at this level. Event rate at the third level trigger output was of the order of a few Hz. Events accepted by TLT were written to tape.

Chapter 4

Monte Carlo Samples

Monte Carlo simulations (MC) are commonly used and serve many purposes. In many cases studied processes are so complicated that only the use of MC makes it possible to understand them. Simulations give possibility to mix theoretical calculations with empirical models of processes which are currently beyond the scope of theoretical models.

MC simulations in particle physics can be split into two stages. First, hadron level four-momenta are generated. This stage is common to all experiments. It is based on theoretical and empirical models of simulated processes. At this stage also all physics corrections, e.g. QED radiation simulation, are applied. The output of this part of simulation is a set of hadron level particles and their four-momenta. At the second stage, interaction of these particles with matter is simulated. This part is usually experiment specific, because matter distribution is different for each detector. Not to mention detector response. Simulation results are analysed in exactly the same way as data. It allows for test of experimental methods and direct comparison of theoretical models to data.

This analysis utilises MC simulations for estimation of detector effects and background. RAPGAP [28] Monte Carlo generator has been used to generate diffractive samples. Non-diffractive samples have been generated with DJANGOH [52] using Ariadne [53] QCD cascade. All samples, except for the two-gluon and BGF ones, include simulation of QED radiation. The simulation has been done with HERACLES [54]. The detector simulation has been done with MOZART [40] package.

4.1 Diffractive Samples

RAPGAP [28] is MC generator of electron(positron)-proton and proton-proton collisions. RAPGAP is using BASES [55] package to calculate integrals using Monte Carlo method. The package is also used to generate pseudo random numbers.

Several theoretical models are implemented in RAPGAP. Main diffractive sample used in the analysis has been generated with saturation model (SATRAP), which process number in RAPGAP equals IPRO=3000. The model is described in sec 2.4.2 on page 18. CTEQ set 5D [56] proton parton distribution functions have been used. Events have been generated in kinematic range of $Q^2 > 4\,\mathrm{GeV}^2$ and $W > 5\,\mathrm{GeV}$. Hadronisation has been simulated with JETSET [57] program, where an ALEPH tune have been set. JETSET is based on Lund string fragmentation model [58]. In order to obtain better description of the data SATRAP MC is weighted

$$w = \left(-0.01M^2 + 0.35M - 0.086\right) \times \left(3y^2 - 2.86y + 1.45\right) . \tag{4.1}$$

Additionally a ratio of events with $q\bar{q}$ and $q\bar{q}g$ systems is changed to $q\bar{q}/q\bar{q}g = 1/0.65$ in order to obtain good description of the data by the MC in β distribution. The main diffractive sample

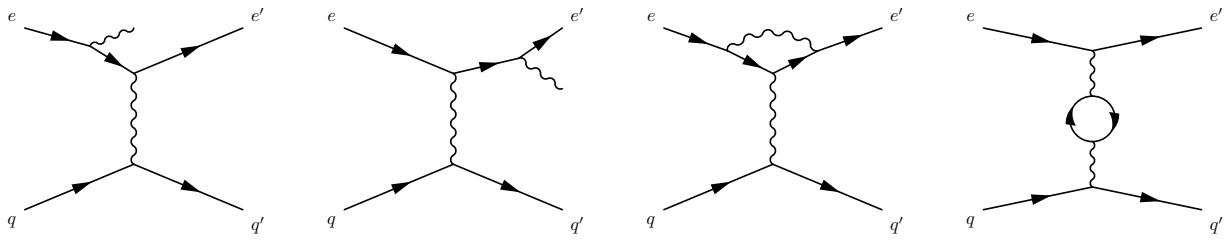

Figure 4.1: Feynman diagrams describing the leading order QED corrections from left to right are: initial state radiation, final state radiation, vertex correction, self-energy correction.

has been used to correct the data for detector effects.

In total 120.42 million events have been generated.

Photoproduction background has been generated with PYTHIA 6.2 [59] generator. CTEQ4 proton parton distribution functions have been used. The sample kinematic region is $Q^2 < 2$ GeV^2.

Diffractive sample of two-gluon exchange has been generated with the same settings as the main sample, only the model of diffractive interaction has been changed (IPRO=20 and IPRO=21). Boson-gluon fusion sample has been obtained in the same way, but with (IPRO=13 and IPRO=14). These samples has been used only for hadron level comparison with unfolded data.

4.2 Non-diffractive Sample

Non-diffractive deep inelastic scattering sample has been generated with DJANGOH. Just like in diffractive samples CTEQ 5D proton parton distributions have been used together with ALEPH tune of JETSET. The ARIADNE used in QCD cascade simulation is based on colour-dipole model [60, 61, 62]. The model is based on assumption that colour-charged partons form dipoles. Gluon emission from the dipole is used to approximate higher-order effects.

4.3 QED Radiation Simulation

HERACLES 4.0 is event generator prepared especially to describe QED processes observed in electron(positron)-proton collisions at HERA centre of mass energies. Leptonic as well as complete one-loop virtual corrections are implemented in HERACLES. This makes the description of QED processes very good. Feynman diagrams describing the leading order QED corrections are presented in fig. 4.1.

4.4 Detector Simulation

MOZART (MOnte carlo for Zeus Analysis, Reconstruction and Trigger) is a package simulating ZEUS detector. It is based on GEANT 3.13 [63] package that was developed at CERN and simulates particles interaction with matter. A ZEUS detector model was created. GEANT package is used to simulate physical processes that particles in the detector undergo. A separate package called ZGANA [64] is used to simulate trigger.

The output of the detector simulation is in exactly the same format as data. This allows for processing MC just like data.

Chapter 5

Event Reconstruction

5.1 Hadronic Final State Reconstruction

Precise reconstruction of particle final state is very important. For it provides fundamental information used in analysis. In order to determine final state particles momenta with the highest possible accuracy, information from tracking and muon detectors, as well as calorimeter is combined. As a result so called "energy flow objects" (EFO) [65, 66, 67] are obtained. Each EFO is regarded as a particle or a group of particles.

Information combination is done in steps. Firstly, calorimeter cells are clustered into cell islands. Secondly, cone islands are reconstructed out of cell islands. Thirdly, tracks are matched to cone islands and particles momenta are reconstructed. Finally, moun corrections are applied.

5.1.1 Cell Islands

Cell islands are clusters of calorimeter cells. Before the clustering, cells that are suspected to contain signal not originating from lepton-proton interaction are removed. There were several sources of noise in calorimeter cells:

depleted uranium used in calorimeter was a source of constant in time noise, which is significantly suppressed by removing the cells with energy in the electromagnetic part smaller than 60 MeV and in hadronic part smaller than 110 MeV, additionally isolated cells with energies smaller than 100 MeV in EMC part and 150 MeV in HAC part are removed; this noise is very well simulated in the MC;

a faulty PMT could give a signal as a result of high-voltage discharge; the use of two photomultipliers per each cell allows for identification of this noise based on the signal imbalance obtained from both PMTs; cells with the following difference in energy signal from left (E_r) and right (E_l) PMT are marked as noise

$$|E_r - E_l| > 0.7\,(E_r + E_l) + 0.018 \text{ GeV} \tag{5.1}$$

one dead and one faulty PMT in a calorimeter cell doesn't allow for high-voltage discharge identification based on PMTs energy imbalance, because the energy of the dead PMT was set to be equal to the energy of the other PMT; the faulty PMT fired more frequently than others, on this basis the noise cells were identified.

Cell islands are created by connecting a cell to one of its nearest neighbours with energy higher than the considered cell. In case of more than one neighbouring cell containing energy greater than the considered cell, the neighbour with the highest energy is chosen. Nearest

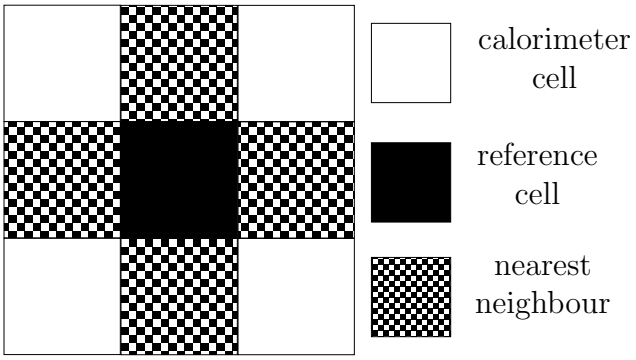

Figure 5.1: Definition of nearest neighbours of a cell. Cells in corners are not considered as nearest neighbours.

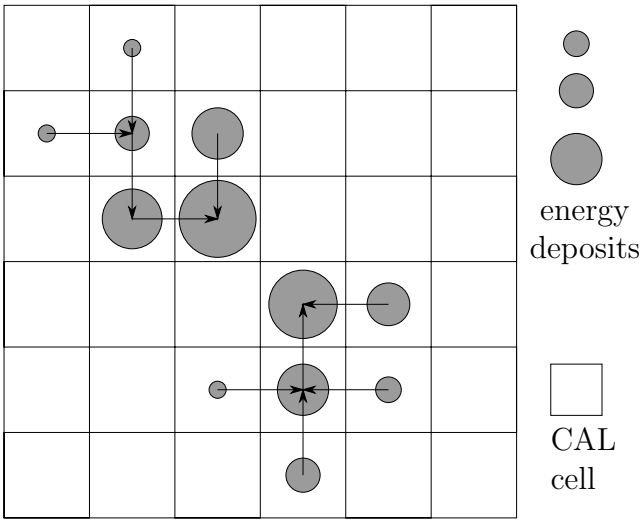

Figure 5.2: Example of cell clustering with cell island clustering algorithm.

neighbours of a cell are cells: above, below, to the right and to the left. Cells in corners are not considered as nearest neighbours. Definition of nearest neighbourhood is depicted in fig. 5.1. Calorimeter cells, that were placed next to the beam pipe, are considered to be each others nearest neighbours. This can lead to reconstruction of energy deposit centre inside the beam pipe. Example of cell islands clustering is shown in figure fig. 5.2.

Clustering algorithm is run separately in all calorimeter parts: FEMC, FHAC1, FHAC2, BEMC, BHAC1, BHAC2, REMC, RHAC.

5.1.2 Cone Islands

Cone islands are clusters of cell islands (sec 5.1.1 on the preceding page). Clustering starts from the outer regions of the detector and goes toward the centre. Firstly, for every HAC2 cell island the closest HAC1 cell island is found. Distance is defined as angle between the vector connecting the HAC2 cell island to the interaction point and the vector connecting HAC1 cell island to the interaction point. The distance (d_{h}) separating the HAC2 cell island from the closest HAC1 cell island is used to calculate combination weight according to the formula obtained based on single pion MC simulations

$$a_{\mathrm{h}}\left(d_{\mathrm{h}}\right) = \exp\left(-643.6 d_{\mathrm{h}}^4 + 483.2 d_{\mathrm{h}}^3 - 103.7 d_{\mathrm{h}}^2 - 6.527 d_{\mathrm{h}}\right) . \tag{5.2}$$

Secondly, the closest EMC cell island is found and angular distance (d_{e}) separating the HAC2 cell island and the EMC cell island is used to calculate combination weight with the formula

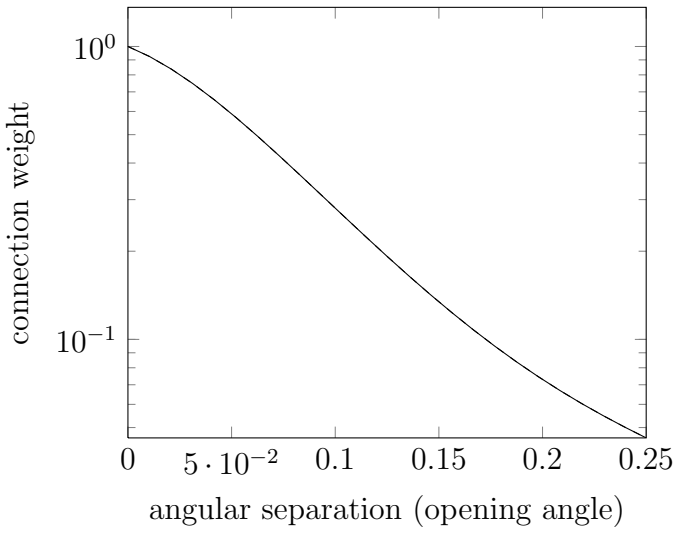

Figure 5.3: Connection weight as a function of angular separation. Dashed line shows connection weight between hadronic clusters, solid line shows connection weight between hadronic and electromagnetic clusters as well as between electromagnetic clusters.

obtained based on single pion MC simulations

$$a_{\mathrm{e}}\left(d_{\mathrm{e}}\right) = \exp\left(-650.5 d_{\mathrm{e}}^4 + 509.2 d_{\mathrm{e}}^3 - 100.1 d_{\mathrm{e}}^2 - 11.75 d_{\mathrm{e}}\right) . \tag{5.3}$$

Out of the two combination weights (a_{h} and a_{e}) larger one is chosen as the combination weight (a) and connection corresponding to this weight is considered. Cell islands are connected if combination weight is greater than 0.05.

Next HAC1 cell islands are connected to EMC cell islands using the same algorithm. For each HAC1 cell island, closest EMC cell island is found based on angular separation. Using formula for HAC to EMC connection weight eq. 5.3. When connection weight is greater than 0.05, HAC1 and EMC cell islands are combined.

Finally, EMC cell islands are connected to each other. Angular separation between a EMC cell island and its nearest neighbour is used to calculate connection weight (a) with eq. 5.3. Unlike HAC2 and HAC1 cases, connection is done if weight is greater than 0.2.

All connected cell islands form a cone island.

5.1.3 Cone island position reconstruction

Cell cluster position reconstruction algorithm as input takes position of each calorimeter cell and energy deposited in the cell. Cell position is a geometrical cell centre shifted according to energy imbalance in photomultiplier tubes used in cell readout.

Cell cluster position is a weighted mean position of all calorimeter cells constituting the cluster

$$\vec{R} = \frac{\sum_i w_i \vec{r_i}}{\sum_i w_i} . \tag{5.4}$$

Hadronic (HAC) and electromagnetic (EMC) calorimeter cells weights are calculated according to the following formulae:

$$w_i^{\mathrm{HAC}} = \max\left\{0;\ 2 + \ln\left(\frac{E_i}{E_{tot}}\right)\right\} , \tag{5.5}$$

$$w_i^{\mathrm{EMC}} = \max\left\{0;\ 4 + \ln\left(\frac{E_i}{E_{tot}}\right)\right\} . \tag{5.6}$$

E_i and E_{tot} are energy deposited in the cell and total cluster energy. Logarithmic weights compensate exponential falloff of shower energy.

5.1.4 EFO Reconstruction

Once calorimeter information is fully reconstructed, it is combined with tracking information. A track is assigned to a cone island if distance between track extrapolated to calorimeter and cone island is smaller than 20 cm or smaller than cone island extent. The extent is defined as size of a cone island projected to a plane perpendicular to a line connecting the interaction point with the cone island. Connected cone islands and tracks form EFO.

5.1.5 EFO momentum reconstruction

Several EFO momentum reconstruction methods are used. Reconstruction method depends on EFO characteristics.

1. EFO is only a single track. In this case it is assumed to be a charged pion. With this assumption tracking information is used to determine EFO's momentum.

2. EFO is only a single cone island. In this case EFO is assumed to be a neutral particle and its momentum is reconstructed with the use of calorimeter information.

3. EFO is a cone island with at least four tracks. It is assumed that EFO is a group of particles and only calorimeter information is used in momentum reconstruction.

4. EFO is a cone island and a track. In this case there are three possibilities:

   (a) only track information is used when

   - energy deposited in calorimeter is not significantly greater than energy measured with track and EFO's momentum measured with track is more precise than with calorimeter. Energy condition is checked with energy ratio: $E_{cal}/E_{track} < 1 + 1.2\sigma\,(E_{cal}/E_{track})$. A margin of 1.2 of standard deviation of ratio is used.
   - EFO is reconstructed in one of "supercrack" regions with calorimeter energy deposit smaller than 1.2 of track energy and track momentum resolution is better than calorimeter resolution.
   - EFO is assumed to be a muon, which was well reconstructed with track. This is the case when following conditions are fulfilled:
     - calorimeter energy deposit is smaller than 5 GeV
     - $E_{cal}/E_{track} < 0.25$
     - track transverse momentum is smaller than 30 GeV

   (b) energy measured with calorimeter and track angular information is used when $E_{cal}/E_{track} < 1 + 1.2\sigma\,(E_{cal}/E_{track})$ and track energy resolution is worse than calorimeter one.

   (c) only calorimeter information is used in all cases that are not mentioned above.

5. EFO is reconstructed with one or two cone islands and two or three tracks. In this case a track, that is the sum of tracks associated to EFO, and a cone island, that is the sum of cone islands associated to EFO, are used with momentum reconstruction algorithm presented in case 4, i.e. when EFO is build of only one track and only one cone island.

5.1.6 Muon corrections

Fully reconstructed EFOs are corrected with muon information. Corrections are applied only to EFOs that are considered to be good muon candidates by GMUON [68] finder. Following corrections are applied:

1. EFO reconstructed with only track information is replaced by EFO reconstructed with only muon information

2. EFO is added if muon track is not associated to any existing EFO

3. EFO is added if muon track is associated with EFO that was reconstructed with some other track

4. EFO with energy greater than 150% of minimal ionising particle energy deposit is considered to be a cluster of particles. Energy that would be deposited in calorimeter by minimal ionising particle is subtracted from EFO energy and new EFO, reconstructed with muon information, is added

5. EFO is added if muon candidate has energy smaller than 50% of minimal ionising particle energy deposit

5.2 Scattered Lepton Identification and Reconstruction

Scattered lepton is identified with the help of neural network algorithm called SINISTRA [69, 70]. The identification is done with only calorimeter information. The use of neural network allowed to do selection based on 55 parameters (54 signals from photomultiplier tubes and the angle of incidence of the particle).

Firstly, a clustering algorithm is run. The algorithm is supposed to identify groups of calorimeter towers corresponding to one particle. Such groups are called islands. Clustering is done by assigning a tower to its nearest neighbour with the highest energy. Tower which energy is greater than energy deposited in any of the nearest neighbouring towers is called the seed. Towers pointing to the same seed as well as the seed constitute an island. A subset of island's towers consisting of the seed and its nearest neighbours is distinguished and referred to as the window.

Leptons scattered at low angles deposit energy close to the edge of the calorimeter. Identification of such leptons is problematic because of their interaction with the beam pipe and possibility of depositing large amounts of energy in hadronic calorimeter. In order to avoid such problems, islands close to the beam pipe, i.e. in the region

$$\begin{cases} X/\mathrm{cm} \in (-14, 14) \\ Y/\mathrm{cm} \in (-14, 14)\,, \end{cases} \tag{5.7}$$

are removed.

Before the actual neural network algorithm is used, preselection is done. Scattered lepton is expected to deposit most of its energy in the electromagnetic calorimeter, thus it is required that at least 80% of the window total energy is deposited in EMC

$$\frac{E^{\mathrm{w}}_{EMC}}{E^{\mathrm{w}}_{\mathrm{tot}}} > 0.8\,. \tag{5.8}$$

A well separated scattered lepton deposits most of its energy in area defined by the window. This property gives rise to two more criteria. It is required that at least 90% of the total island energy is deposited in the window

$$\frac{E_{\mathrm{tot}}^{\mathrm{w}}}{E_{\mathrm{tot}}} > 0.9\,. \tag{5.9}$$

Moreover, energy deposited outside the window cannot be larger than 1 GeV

$$E_{\mathrm{tot}} - E_{\mathrm{tot}}^{\mathrm{w}} < 1\ \mathrm{GeV}\,. \tag{5.10}$$

The above three cuts reject about 90% of hadronic clusters while causing inefficiency, by electromagnetic clusters rejection, of the order of 3%.

Distinction between electromagnetic and hadronic showers with energies greater than 12 GeV is possible even with simple cuts. Neural network was trained in the more difficult region of energies between 4 GeV and 12 GeV. A sample of 3555 electromagnetic and 3555 hadronic showers had been generated. The sample was used to train neural network in 2000 epochs.

Each tower in the rear part of the electromagnetic calorimeter consisted of two cells. Each cell was read by two photomultiplier tubes. Towers in the front and barrel parts of the EMC consisted of four cells. In order to have the island described with the same parameters in all calorimeter parts, the signals from the upper and lower cells in the FCAL and BCAL are summed. In this way each window is described by 36 PMTs signals from the EMC. PMTs signals from both sections of hadronic calorimeter are summed resulting in another 18 parameters. In total there is information from 54 PMTs. This information together with the angle of incidence of the particle are input to the neural network algorithm.

The result of SINISTRA algorithm is probability that a given island is the product of electromagnetic shower. Only energy clusters with probability greater than 90% are assumed to be electromagnetic. The electromagnetic cluster with the highest probability is identified as scattered lepton. In case there are two clusters with the same probability the one with higher energy is chosen. Efficiency of the neural network algorithm is above 85% for energy deposits of 10 GeV and grows with the energy. Purity is greater than 96% for clusters with energy above 10 GeV.

Scattered lepton is assigned energy of the appropriate cluster corrected for the detector effects (e.g. inactive material). Direction of the lepton momentum is calculated as the direction of the vector connecting the reconstructed interaction point with the position of the scattered lepton in the calorimeter.

5.3 Kinematics Reconstruction

Once EFOs are reconstructed and scattered lepton candidate is identified, event kinematics can be calculated. Several methods of reconstruction of kinematic variables are used in the analysis. All of the following equations are derived using the coordinate system in which incoming lepton and proton move along the Z axis. Their four-momenta are written explicitly in eq. 2.3 on page 4 and eq. 2.4 on page 4. A comparison of relative resolutions of different methods is presented in fig. 5.4 on page 40 and summarised in tab. 5.1 on the next page. Resolutions are calculated for kinematic range covered in this analysis.

5.3.1 Electron Method

Electron method (El) reconstructs kinematic variables using only information about incoming and scattered lepton. Scattered lepton four-momentum is usually precisely measured, thus electron method gives accurate values. However, the results can be easily distorted by the

Table 5.1: Comparison of relative resolutions of kinematic variables calculated with different reconstruction methods.

variable	σ_{El}	σ_{JB}	σ_{DA}
x	0.20	0.31	0.17
y	0.13	0.19	0.10
Q^2	0.07	0.36	0.06
W	0.07	0.10	0.06

initial or final state radiation. All of the following formulae depend on the lepton energy before interaction, which is assumed to be equal to the lepton beam energy. If initial state radiation is present, this assumption is no longer valid. Final state radiation affects this method if scattered lepton four-momentum is not corrected for the emitted photon (sec 5.7.1 on page 45).

Formulae for reconstruction of kinematic variables can be derived straight from their definitions by substituting variables with their measured equivalents.

- inelasticity is calculated from eq. 2.20 on page 5

$$y_{\mathrm{El}} = 1 - \frac{E_{e'}}{2E_e}\left(1 - \cos\theta_{e'}\right) \tag{5.11}$$

- virtuality is reconstructed using eq. 2.14 on page 4

$$Q^2_{\mathrm{El}} = 2E_e E_{e'}\left(1 + \cos\theta_{e'}\right) \tag{5.12}$$

- Bjorken scaling variable is calculated with eq. 2.35 on page 6

$$x_{\mathrm{El}} = \frac{E_{e'}\left(1 + \cos\theta_{e'}\right)}{2y_{\mathrm{El}}E_p} \tag{5.13}$$

- boson-proton centre of mass energy is calculated with eq. 2.39 on page 6

$$W_{\mathrm{El}} = \sqrt{4E_pE_ey_{\mathrm{El}} - Q^2_{\mathrm{El}}} \tag{5.14}$$

5.3.2 Jacquet-Blondel Method

Jacquet-Blondel method (JB) [71], to reconstruct kinematic variables, uses only information about hadronic final state. Since scattered lepton four-momentum is not used in calculations, the method can be also used to reconstruct kinematics in charged current processes. This method is insensitive to final state radiation (unless the photon is reconstructed as a part of hadronic system), however yields rather poor resolutions compared to other methods. The resolution is poor, because hadronic final state is not measured as precisely as scattered lepton.

JB method assumes that transverse momentum of undetected final state particles is negligible.

- inelasticity is calculated with eq. 2.51 on page 8

$$y_{\mathrm{JB}} = \frac{E_h - p_{z,h}}{2E_e} \tag{5.15}$$

- virtuality is reconstructed using eq. 2.55 on page 8

$$Q^2_{\mathrm{JB}} = \frac{p^2_{x,h} + p^2_{y,h}}{1 - y_{\mathrm{JB}}} \tag{5.16}$$

- Bjorken scaling variable is calculated by neglecting proton mass in eq. 2.37 on page 6

$$x_{\mathrm{JB}} = \frac{Q^2_{\mathrm{JB}}}{s y_{\mathrm{JB}}} \tag{5.17}$$

- boson-proton centre of mass energy is calculated with eq. 2.39 on page 6

$$W_{\mathrm{JB}} = \sqrt{4 E_p E_e y_{\mathrm{JB}} - Q^2_{\mathrm{JB}}} \tag{5.18}$$

5.3.3 Double-Angle Method

Double-angle method (DA) [72] reconstructs kinematic variables using only information about angles of scattered lepton and hadronic system. Since no energy measurement is used, this method is more precise than Jacquet-Blondel method and is not as vulnerable to QED radiation as electron method.

Apart from scattered lepton polar angle, the method uses effective polar angle of hadronic system. In order to not use absolute energy measurement the effective angle is calculated as follows

$$\cos\theta_h = \frac{p^2_{t,h} - (E_h - p_{z,h})^2}{p^2_{t,h} + (E_h - p_{z,h})^2}\,. \tag{5.19}$$

It can be shown that the above formula is equal to the cosine of an effective polar angle of the hadronic system, by neglecting the mass

$$\begin{aligned}
\cos\theta_h &= \frac{p^2_{x,h} + p^2_{y,h} - (E_h - p_{z,h})^2}{p^2_{x,h} + p^2_{y,h} + (E_h - p_{z,h})^2} && (5.20)\\
&= \frac{p^2_{x,h} + p^2_{y,h} - E^2_h + 2E_h p_{z,h} - p^2_{z,h}}{p^2_{x,h} + p^2_{y,h} + E^2_h - 2E_h p_{z,h} + p^2_{z,h}} && (5.21)\\
&= \frac{p^2_{x,h} + p^2_{y,h} - p^2_{x,h} - p^2_{y,h} - p^2_{z,h} + 2E_h p_{z,h} - p^2_{z,h}}{2E^2_h - 2E_h p_{z,h}} && (5.22)\\
&= \frac{2p_{z,h}\,(E_h - p_{z,h})}{2E_h\,(E_h - p_{z,h})} && (5.23)\\
&= \frac{p_{z,h}}{E_h}\,. && (5.24)
\end{aligned}$$

The DA method is based on the fact that using energy momentum conservation rule, scattered lepton energy can be expressed in terms of angles eq. 2.48 on page 7

$$\begin{aligned}
E_{e'} &= \frac{2E_e \sin\theta_h}{\sin\theta_{e'}\,(1 - \cos\theta_h) + \sin\theta_h\,(1 - \cos\theta_{e'})} && (5.25)\\
&= \frac{2E_e \sin\theta_h}{\sin\theta_{e'} + \sin\theta_h - \sin(\theta_h + \theta_{e'})}\,. && (5.26)
\end{aligned}$$

Energy calculated in such way is used in equations obtained with electron method.

- inelasticity (from eq. 5.11 on page 37)

$$y_{\mathrm{DA}} = 1 - \frac{1}{2E_e}\frac{2E_e \sin\theta_h}{\sin\theta_{e'}\,(1-\cos\theta_h) + \sin\theta_h\,(1-\cos\theta_{e'})}\,(1-\cos\theta_{e'}) \tag{5.27}$$

$$= \frac{\sin\theta_{e'}\,(1-\cos\theta_h)}{\sin\theta_h\,(1-\cos\theta_{e'}) + \sin\theta_{e'}\,(1-\cos\theta_h)} \tag{5.28}$$

$$= \frac{\sin\theta_h\,(1+\cos\theta_{e'})}{\sin\theta_{e'} + \sin\theta_h + \sin\left(\theta_h + \theta_{e'}\right)} \tag{5.29}$$

- virtuality (from eq. 5.12 on page 37)

$$Q^2_{\mathrm{DA}} = 2E_e\frac{2E_e \sin\theta_h}{\sin\theta_{e'}\,(1-\cos\theta_h) + \sin\theta_h\,(1-\cos\theta_{e'})}\,(1+\cos\theta_{e'}) \tag{5.30}$$

$$= \frac{4E_e^2 \sin\theta_h\,(1+\cos\theta_{e'})}{\sin\theta_h\,(1-\cos\theta_{e'}) + \sin\theta_{e'}\,(1-\cos\theta_h)} \tag{5.31}$$

$$= \frac{4E_e^2 \sin\theta_h\,(1+\cos\theta_{e'})}{\sin\theta_{e'} + \sin\theta_h - \sin\left(\theta_h + \theta_{e'}\right)} \tag{5.32}$$

- Bjorken scaling variable (from eq. 5.13 on page 37)

$$x_{\mathrm{DA}} = \frac{2E_e \sin\theta_h}{\sin\theta_{e'}\,(1-\cos\theta_h) + \sin\theta_h\,(1-\cos\theta_{e'})}\frac{1+\cos\theta_{e'}}{2y_{\mathrm{DA}}E_p} \tag{5.33}$$

$$= \frac{E_e}{E_p}\frac{\sin\theta_h\,(1+\cos\theta_{e'})}{\sin\theta_{e'}\,(1-\cos\theta_h)} \tag{5.34}$$

$$= \frac{E_e}{E_p}\frac{\sin\theta_h + \sin\theta_{e'} + \sin\left(\theta_h + \theta_{e'}\right)}{\sin\theta_h + \sin\theta_{e'} - \sin\left(\theta_h + \theta_{e'}\right)} \tag{5.35}$$

- boson-proton centre of mass energy is calculated with eq. 2.39 on page 6

$$W_{\mathrm{DA}} = \sqrt{4E_pE_ey_{\mathrm{DA}} - Q^2_{\mathrm{DA}}} \tag{5.36}$$

5.4 Reconstruction of Diffractive Variables

Diffractive variables that are used in the analysis and are not measured directly are: fraction of incoming proton momentum carried by pomeron ($x_{\mathbb{P}}$) and fraction of pomeron momentum carried by interacting parton (β). Both quantities are reconstructed using DIS kinematics calculated with double-angle method.

- $x_{\mathbb{P}}$ is calculated according to eq. 2.74 on page 12

$$x_{\mathbb{P}} = x_{\mathrm{DA}}\frac{Q^2_{\mathrm{DA}} + M^2}{Q^2_{\mathrm{DA}}} \tag{5.37}$$

- β is calculated according to eq. 2.72 on page 12

$$\beta = \frac{Q^2_{\mathrm{DA}}}{Q^2_{\mathrm{DA}} + M^2} \tag{5.38}$$

Distribution of differences between fraction of the proton momentum carried by the pomeron reconstructed using DA and hadron level $x_{\mathbb{P}}$ is shown in fig. 5.5 on page 41. Resolution of $x_{\mathbb{P}}$ equals 0.001. Distribution of relative differences between β and β is shown also in fig. 5.5 on page 41. Relative resolution of β equals 0.2.

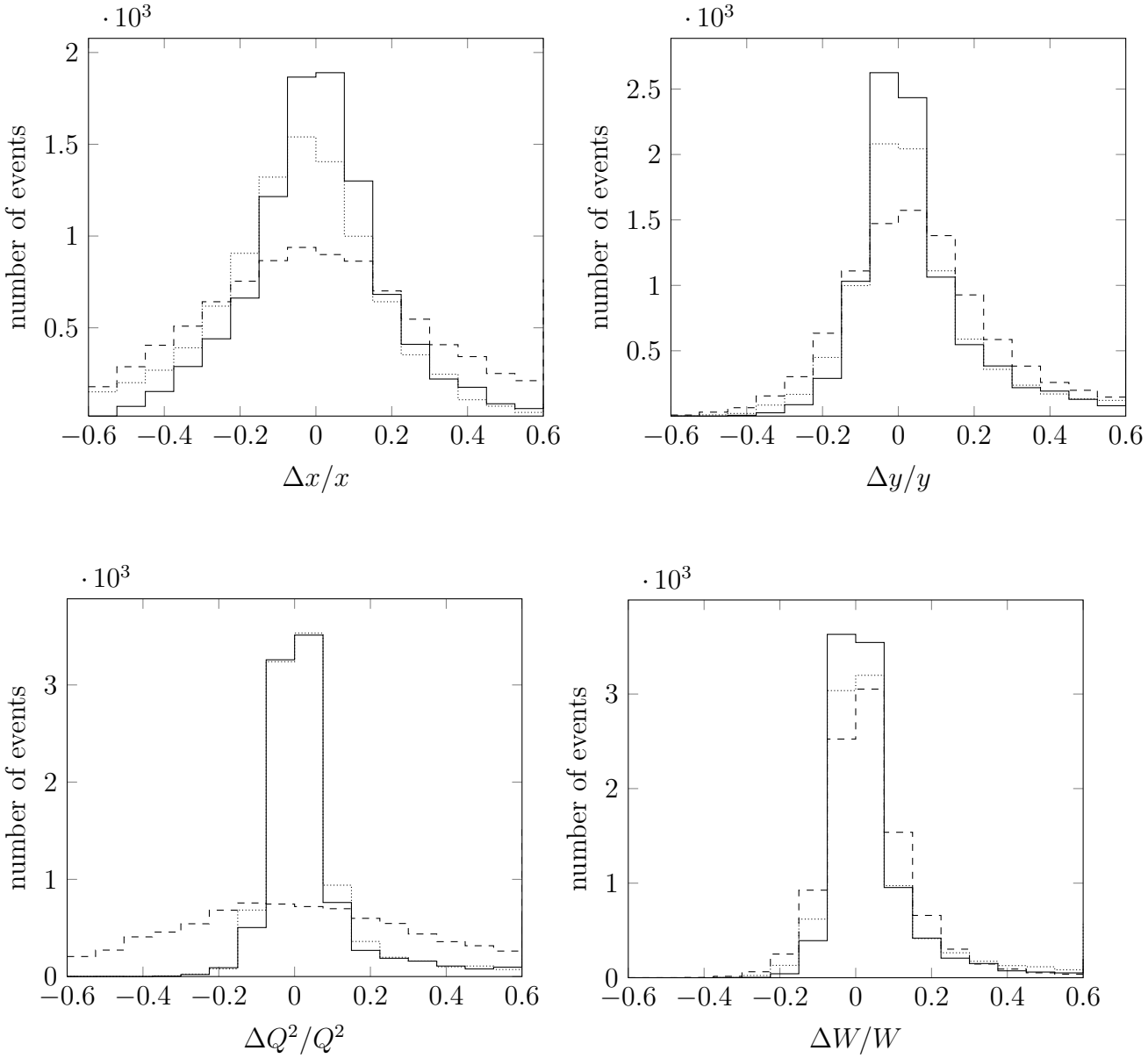

Figure 5.4: Distributions of relative differences between reconstructed and generated, values of kinematic variables estimated with SATRAP. Distributions of Bjorken scaling variable (on the left) and inelasticity (on the right) are presented in the upper row. Distributions of virtuality (on the left) and boson-proton centre of mass energy (on the right) are presented in the lower row. Dotted histograms show relative differences for kinematic variables reconstructed with electron method, dashed histograms show relative differences for kinematic variables reconstructed with Jacquet-Blondel method, solid histograms show relative differences for kinematic variables reconstructed with double-angle method.

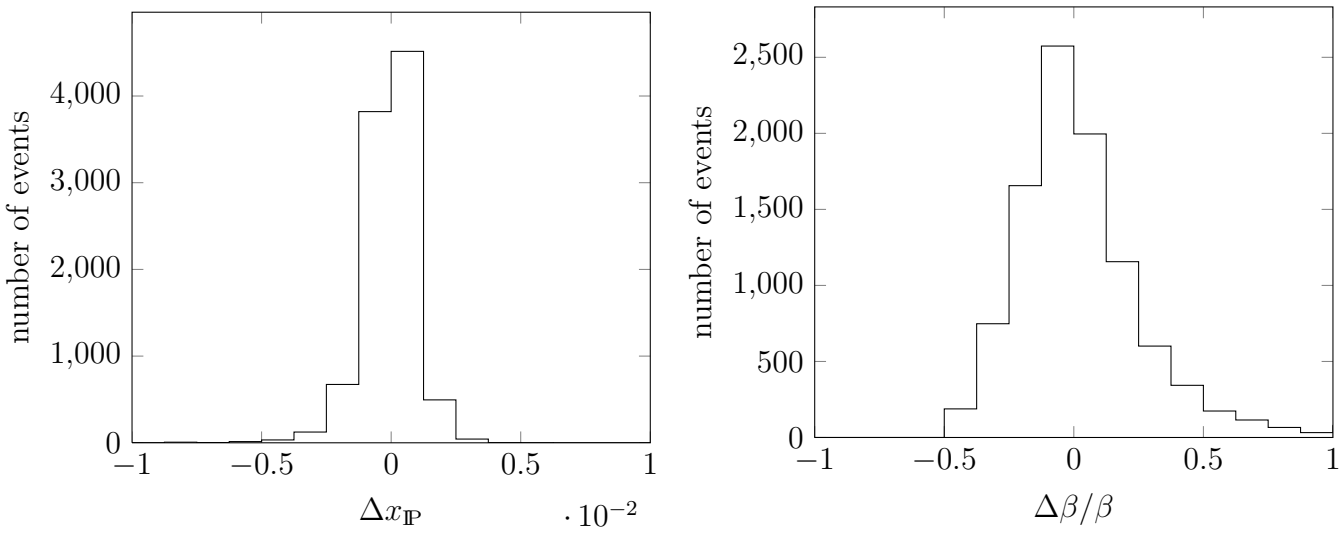

Figure 5.5: Distributions of relative differences between reconstructed, with double-angle method, and generated values of diffractive variables estimated with SATRAP. In the left graph distribution of fraction of incoming proton momentum carried by pomeron is shown. In the right graph distribution of fraction of pomeron momentum carried by interacting parton is shown.

5.5 Jet Reconstruction

Jets are reconstructed using the FastJet package [73]. The package contains implementation of several jet algorithms and allows for adding user defined algorithms as plugins.

5.5.1 Durham Jet Algorithm

Out of native FastJet algorithms k_t for e^+e^- is used in exclusive mode. The algorithm is also known as Durham jet algorithm [74]. The advantage of this algorithm is that it can be used in theoretical calculations and in measurement with small values of the jet resolution parameter y_{cut}. The fact that jets are resolved by relative transverse momentum makes the algorithm preserve exponentiation i.e. terms of the form $\alpha_s^n \ln^m (y_{\text{cut}})$ can be combined into an exponential function of less singular terms [75, 76]. This allows for resummation of all double logarithmic terms $(\alpha_s \ln^2 y_{\text{cut}})$, which are the effective coupling. Double logarithmic terms are associated with soft and collinear gluon emission. This kind of emission is important when radiation is suppressed by kinematics. In case of small y_{cut} values radiation is suppressed by small invariant mass of the jet.

The exclusive mode is chosen, because the process under studies consists of only a quark-antiquark pair. This mode preserves properties of the studied process, e.g. back-to-back jet configuration in hadronic system centre of mass frame.

The algorithm consists of the steps listed below.

1. Scaled transverse momentum y_{ij} is calculated for every pair of final state objects (i, j). The momentum is defined as

$$y_{ij} := 2\frac{\min\left(E_i^2, E_j^2\right)}{M^2}\left(1 - \cos\theta_{ij}\right) . \tag{5.39}$$

   θ_{ij} is an angle between objects (i, j) and M^2 is total energy of hadronic system.

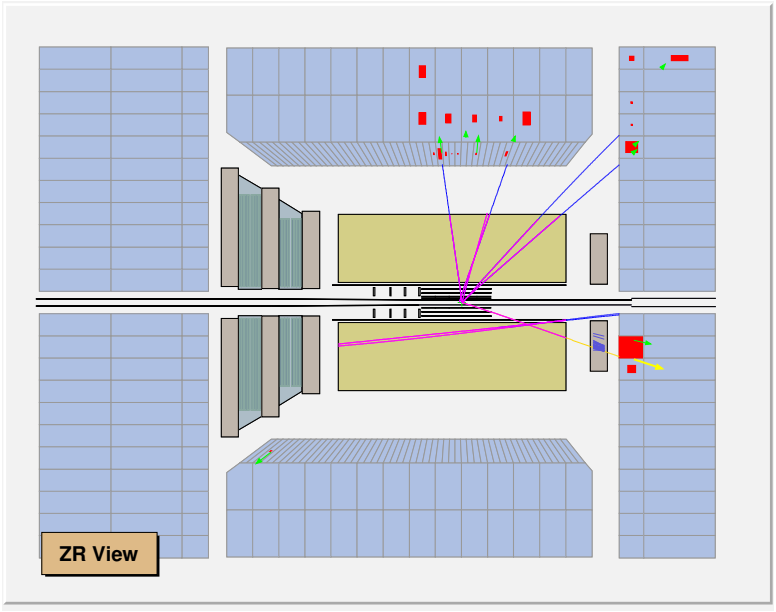

Figure 5.6: Display of event 1554 of run 61588. Green arrows represent energy flow objects. Yellow arrow shows EFO identified as scattered lepton. Size of red rectangles is proportional to energy deposited in calorimeter cell. In lower left corner of the calorimeter, isolated EFO with low energy is visible. If it were present on jet algorithm particles input list, it would create a fake jet.

2. If the smallest momentum is smaller than the jet resolution parameter, particles corresponding to this momentum are combined into a pseudoparticle. The new particle's momentum is calculated with energy scheme i.e. the four-vectors of merged particles are summed.

3. The above steps are repeated until all scaled transverse momenta are larger than y_{cut}.

5.5.2 Input and Jet Resolution Parameter

Jets are reconstructed in the virtual photon-pomeron centre of mass reference frame. This makes jet algorithm sensitive to separated particles with low energy, which boosted by the transformation gain large momentum and create fake jets. Example of an event containing such low energy particle is shown in fig. 5.6. In order to overcome this problem EFOs with insufficient energy and large separation from other EFOs are removed from the input to the jet algorithm. Energy threshold is set to 400 MeV. This is standard ZEUS energy threshold. Separation distance has been chosen based on MC studies. Distributions of low energy EFOs separations for events with well reconstructed jets ($|\Delta p_{t,jet}/p_{t,jet}| < 0.1$) and badly reconstructed jets ($\Delta p_{t,jet}/p_{t,jet} > 0.4$) are presented in fig. 5.7 on the next page. The separation threshold has been set to $\pi/2$, since above this value badly reconstructed jets dominate. The above selection procedure also makes jet multiplicity in MC agree with the data jet multiplicity.

The transformation is done in two steps. Firstly, all input EFOs are boosted to their centre of mass frame. Scattered lepton and virtual photon undergo the same boost. Next, coordinate system is rotated such that Z axis is pointing along the virtual photon momentum and scattered lepton lies in XZ plane.

Jets calculated on hadron level are calculated using stable final state hadrons transformed to the γ^*-$\mathbb{P}$ centre of mass reference frame. Transformation is done in the same way as on detector level. The only difference is that true virtual photon and scattered lepton momenta

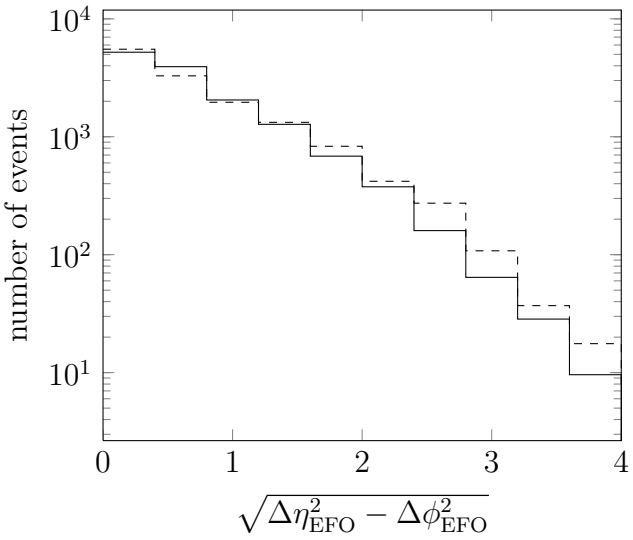

Figure 5.7: Distribution of separations, in pseudorapidity and azimuthal angle, of EFO with energy smaller than 400 MeV from EFOs with energy greater than 400 MeV. Solid lines corresponds to events with well reconstructed jets ($|\Delta p_{t,jet}/p_{t,jet}| < 0.1$) and dashed line corresponds to events with badly reconstructed jets ($\Delta p_{t,jet}/p_{t,jet} > 0.4$).

are used.

Detector and hadron level jets are reconstructed with jet resolution parameter equal $y_{\mathrm{cut}} = 0.15$. This value ensures high efficiency of the jet algorithm.

5.6 Resolutions

In order to calculate resolutions, a detector level jet must be assigned a hadron level jet. The distance between detector and hadron level jets in $\phi - \eta$ space is used to pair jets. Jets that are closest to each other are coupled i.e. detector level jet is assigned a hadron level jet that value of $\sqrt{\left(\eta_{jet} - \eta_{jet^{\mathrm{had}}}\right)^2 + \left(\phi_{jet} - \phi_{jet^{\mathrm{had}}}\right)^2}$ is smallest.

Resolution of jet azimuthal angle as a function of the azimuthal angle itself is presented in fig. 5.8 on the following page. There is no significant bias in azimuthal angle reconstruction. Resolution of the angle doesn't depend on its value except for the angles close to 0 and π, where resolution is worse. This resolution deterioration is caused by QED initial and final state radiation. Detailed studies are presented in sec. 5.7. Resolution of jet azimuthal angle as a function of jet transverse momentum is also shown in fig. 5.8 on the following page. It can be observed that the higher transverse momentum the better angular distribution.

Resolution of jet transverse momentum in function of jet azimuthal angle is shown in fig. 5.9 on the next page. Reconstructed transverse momentum is biased towards higher values. It is expected since jet transverse momentum is steeply falling distribution. The biggest bias is observed for jets with azimuthal angles close to 0 or π. Additionally, resolution of these jets is worse than of the rest. This also is the effect of QED initial and final state radiation (sec. 5.7).

5.7 QED Radiation

Incoming lepton, before interacting with proton, can emit a photon, such process is called initial state radiation (ISR). Analogously scattered lepton can emit a photon after interacting with

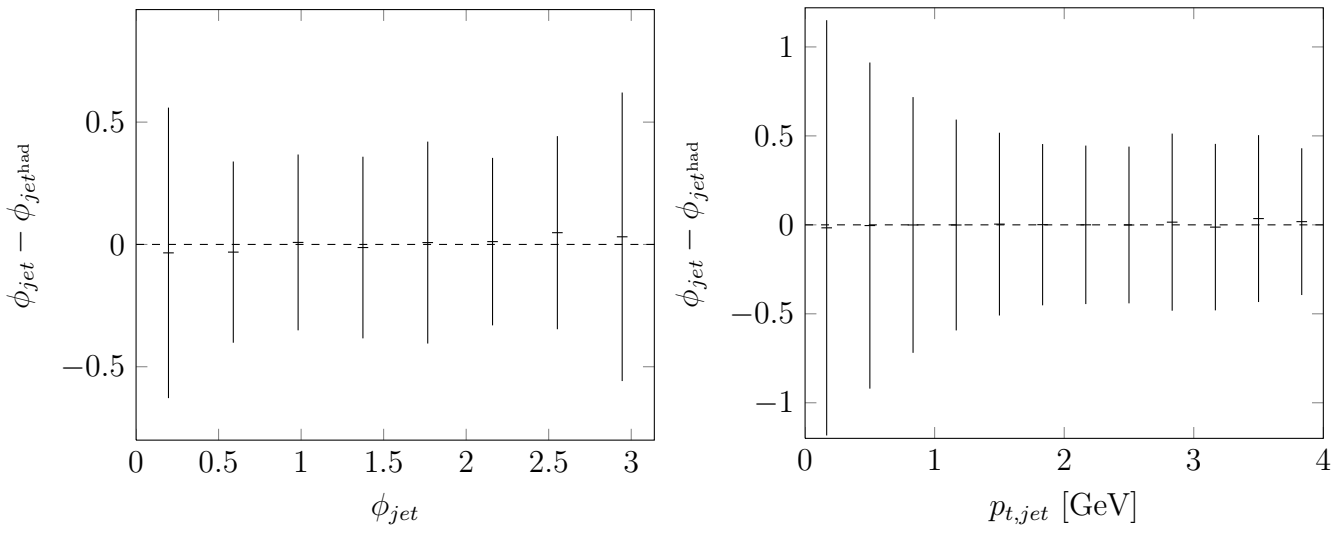

Figure 5.8: Distribution of differences of jet azimuthal angle reconstructed on detector and hadron level as a function of detector jet azimuthal angle (on the left) and detector jet transverse momentum (on the right). Markers show mean value of the distribution of differences for a given interval of detector jet azimuthal angle. Error bars show standard deviation of the distribution of differences for a given interval of detector jet azimuthal angle.

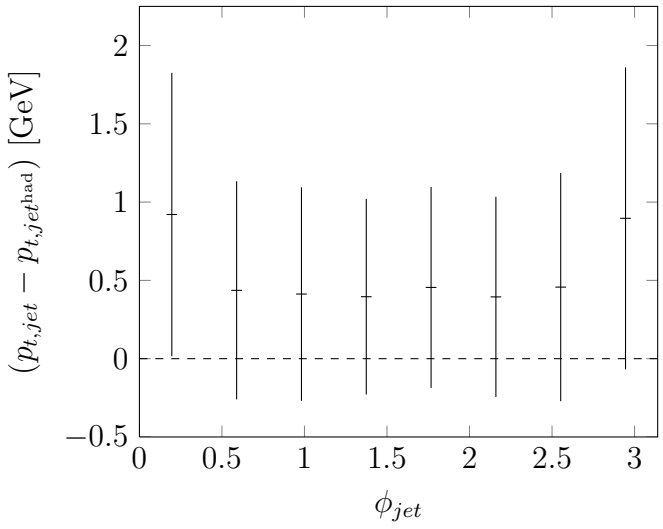

Figure 5.9: Distribution of differences of jet transverse momentum reconstructed on detector and hadron level in function of detector jet azimuthal angle. Markers show mean value of the distribution of differences for a given interval of detector jet azimuthal angle. Error bars show standard deviation of the distribution of differences for a given interval of detector jet azimuthal angle.

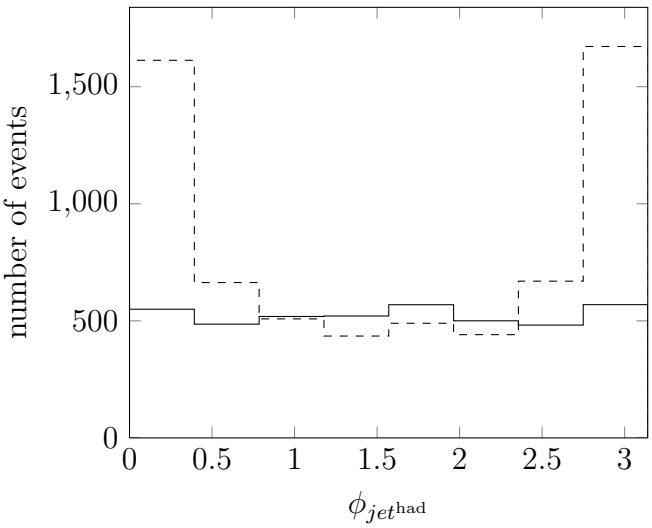

Figure 5.10: Azimuthal angular distribution of jets reconstructed on hadron level. SATRAP 2006 electron sample was used. Events were requiered to pass the following selection criteria: $\beta > 0.45, x_{\mathbb{P}} < 0.01, 100\text{ GeV} < W < 300\text{ GeV}, p_{t,jet} > 2\text{ GeV}$. Solid histogram shows distribution calculated with correct virtual photon, dashed histogram shows distribution reconstructed with virtual photon four-momentum calculated as the difference between incoming and scattered lepton, which does not take into account ISR and FSR.

proton. Such process is called final state radiation (FSR). Both of these processes change event kinematics. Effects of mentioned above processes were investigated.

5.7.1 Effects of ISR and FSR

ISR and FSR change the way virtual photon four-momentum should be reconstructed

$$\mathbf{q} = \left(\mathbf{k} - \mathbf{q}^{\mathbf{isr}}\right) - \left(\mathbf{k}' + \mathbf{q}^{\mathbf{fsr}}\right) . \tag{5.40}$$

Virtual photon four-momentum reconstructed as difference between incoming and scattered lepton four-momenta is shifted with respect to the true virtual photon four-momentum

$$\mathbf{k} - \mathbf{k}' = \mathbf{q} + \mathbf{q}^{\mathbf{isr}} + \mathbf{q}^{\mathbf{fsr}} . \tag{5.41}$$

FSR seldom contribute to the above error, because in case of collinear photon emission, the photon deposits energy in the same calorimeter cell as scattered lepton. Thus scattered lepton four-momentum is automatically corrected for FSR. Only high energy final state radiation emitted at large angles affects virtual photon four-momentum reconstruction. In case of initial state radiation error is always induced.

Incorrectly reconstructed virtual photon four-momentum affects the analysis in two ways. Firstly, all kinematic variables are incorrectly calculated. Secondly, virtual photon four-momentum is used to transform particles to the frame of measurement. The effect of incorrect transformation is clearly visible on hadron level fig. 5.10. Many more events with incorrectly reconstructed photon pass the cuts, because jet transverse momentum is overestimated. Incorrectly reconstructed events tend to have azimuthal angle close to 0 or π.

The effect of migrations of jet azimuthal angle towards 0 or π is also clearly visible in resolution studies. In fig. 5.11 on the following page difference between jet azimuthal angle reconstructed on detector and hadron level as a function of hadron jet azimuthal angle is shown. Differences are not only scattered around 0, but also around lines $\phi_{jet} - \phi_{jet^{\text{had}}} = -\phi_{jet^{\text{had}}}$ and

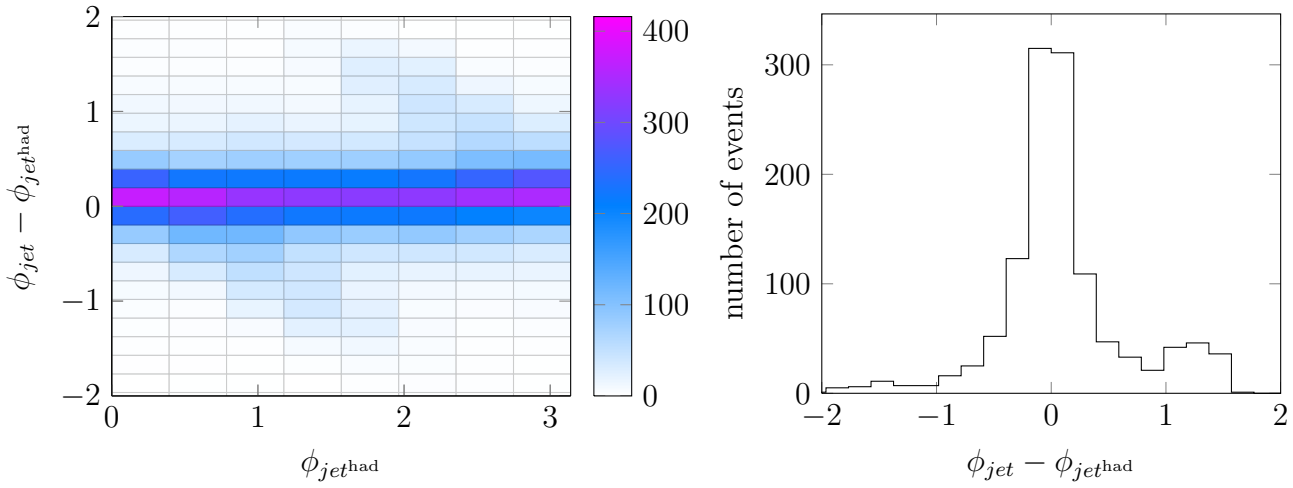

Figure 5.11: Jet azimuthal angle resolution obtained using MC containing ISR and FSR. In the left graph a distribution of differences between jet azimuthal angle reconstructed on detector and hadron level in function of hadron jet azimuthal angle is presented. In the right graph distribution of differences between jet azimuthal angle reconstructed on detector and hadron level for hadron jet azimuthal angles between 1.55 and 1.95 is presented.

$\phi_{jet} - \phi_{jet^{\text{had}}} = -\phi_{jet^{\text{had}}} + \pi$. The projection of the fourth bin shown in fig. 5.11 reveals the second peak in the vicinity of $\phi_{jet^{\text{had}}} = 1.4$.

Results of studies of the jet azimuthal angular resolution in function of hadron jet azimuthal angle repeated with MC not containing ISR or FSR are shown in fig. 5.12 on the facing page. The differences in jet azimuthal angles are centred at 0. There is no second peak in the projection of the fourth bin. This confirms that QED radiation causes migrations of jet azimuthal angle to 0 or π.

In case of high energy initial or final state radiation emitted at large angle the photon can be detected in the calorimeter and reconstructed as separate particle. Then additional error in the transformation is induced. It can also happen that such photon will be identified as a jet since it can be well separated from the hadronic system.

5.7.2 Radiation Tagged Events

It was checked if data confirm that events with initial or final state radiation migrate in jet azimuthal angle towards 0 or π. Events with radiation were selected based on difference between inelasticity reconstructed with electron (sec 5.3.1 on page 36) and Jacquet-Blondel (sec 5.3.2 on page 37) methods as is suggested in [77]. The distribution obtained with data and the MC is presented in fig. 5.13 on the next page. The data is well reproduced by MC. Thus it is expected that the fraction of events with ISR or FSR is also well reproduced and MC can be used to study effects of QED radiation.

In fig. 5.13 on the facing page a contribution from events without ISR nor FSR to full SATRAP MC sample is presented. The MC shows that in the region of $y_{\text{El}} - y_{\text{JB}} > 0.2$ events with QED radiation dominate. Events with radiation are also present in the region where the difference is close to 0. These are events with low energy initial or final state radiation, which does not significantly affect the measurement.

In order to test the effect of QED radiation in data, azimuthal angular distribution of jets in virtual photon-pomeron centre of mass frame was measured. Distributions obtained for events with ($y_{\text{El}} - y_{\text{JB}} > 0.2$) and without ($y_{\text{El}} - y_{\text{JB}} < 0.005$) radiation were compared. The

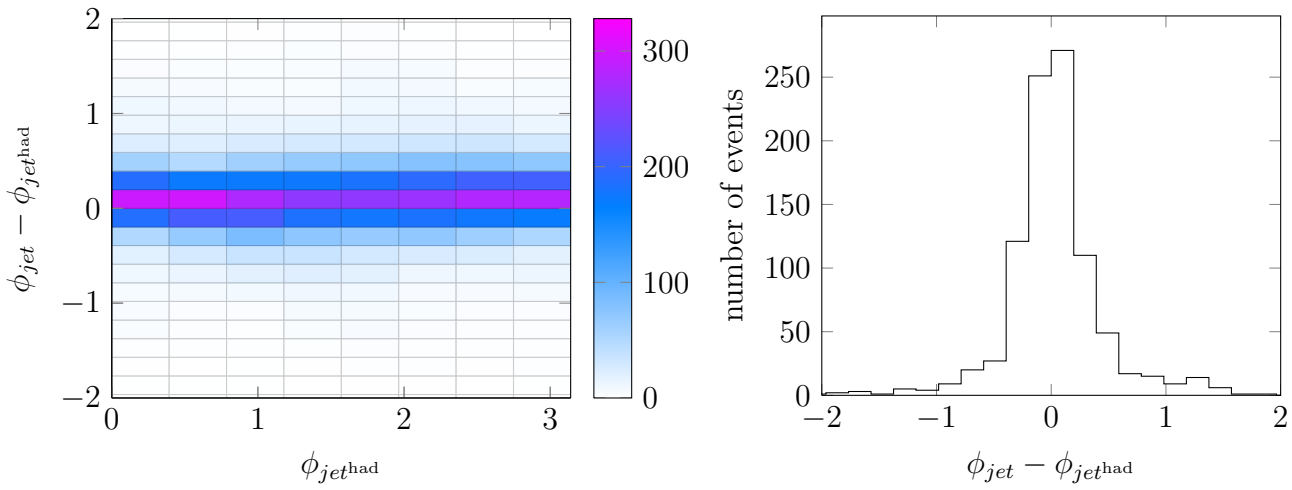

Figure 5.12: Jet azimuthal angle resolution obtained using MC without ISR nor FSR. In the left graph distribution of differences between jet azimuthal angle reconstructed on detector and hadron level in function of hadron jet azimuthal angle is presented. In the right graph distribution of differences between jet azimuthal angle reconstructed on detector and hadron level for hadron jet azimuthal angles between 1.2 and 1.6 is presented.

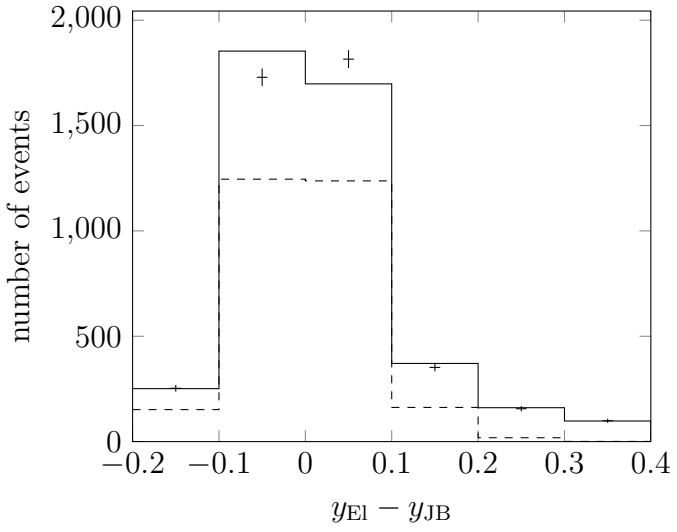

Figure 5.13: Distribution of differences in inelasticity reconstructed with electron and Jacquet-Blondel methods. Figure shows the differences obtained with data and SATRAP MC after the standard selection criteria described in ch. 6 on page 49. Black points show distribution of data as well as statistical errors. Black histogram shows SATRAP distribution. Dashed histogram shows distribution of MC events without ISR or FSR.

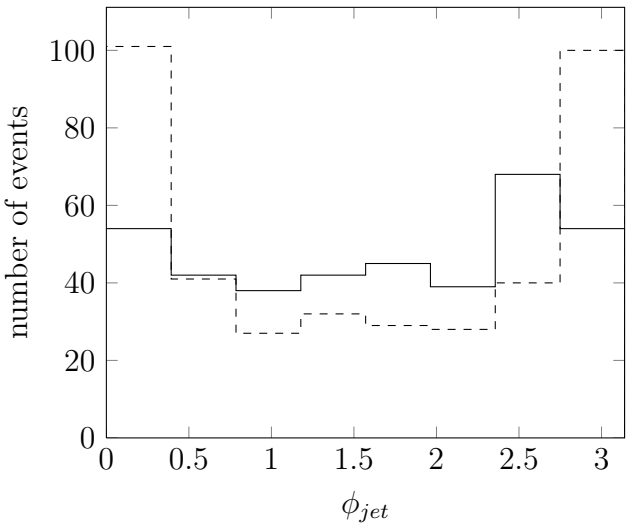

Figure 5.14: Jet azimuthal angular distribution in virtual photon-pomeron centre of mass frame, after the standard selection criteria described in ch. 6 on the next page. Solid histogram shows distribution of events with $y_{\mathrm{El}} - y_{\mathrm{JB}} < 0.005$ i.e. with negligible impact of initial or final state radiation, dashed histogram shows distribution of events with $y_{\mathrm{El}} - y_{\mathrm{JB}} > 0.2$ i.e. with dominating effects of ISR or FSR.

comparison is shown in fig. 5.14. Data behaves similarly to MC. Events with radiation tend to contain jets with azimuthal angle close to 0 or π.

Chapter 6

Data Sample and Signal Selection

In this chapter data used in analysis as well as event selection criteria are described. Monte Carlo samples used in this chapter are normalised to the data. The normalisation has been done with all selection conditions fulfilled.

6.1 Data Sample

Analysed data were collected during HERA II runs i.e. in years 2003-2007. During these years protons were collided with electrons (2004 - 2006) and positrons (2003 - 2004, 2006 - 2007). Colliding protons were accelerated to $E_p = 920$ GeV, leptons to $E_e = 27.5$ GeV. Lepton-proton centre of mass energy was equal to $\sqrt{s} = 318$ GeV. Data recorded during electron as well as positron runs is used. Integrated luminosity of good quality data gated by the ZEUS detector during these years amounts to 372 pb^{-1} [78]. Information about integrated luminosity gated in different periods of data taking is shown in fig. 6.1 on the following page and tab. 6.1.

Only data that were marked EVTAKE = 1 are used in this analysis. This ensures that all detector components were fully operational.

6.2 Online Selection

The first stage of event selection was at online level. Only events accepted by diffractive DIS trigger chain DST50 were considered in further analysis. In order to accept the event every condition in the trigger chain presented below was required to be fulfilled.

Table 6.1: Integrated luminosity of good quality data gated by the ZEUS detector during years 2003 - 2007 [78].

Period	Run Range	Lepton Charge	Luminosity [pb^{-1}]
2003	45416 - 46638	+	2.08
2004	47010 - 51245	+	38.68
2004 - 2005	52244 - 57123	-	134.16
2006	58181 - 59947	-	54.80
2006 - 2007	60005 - 62637	+	142.37
total			372.09

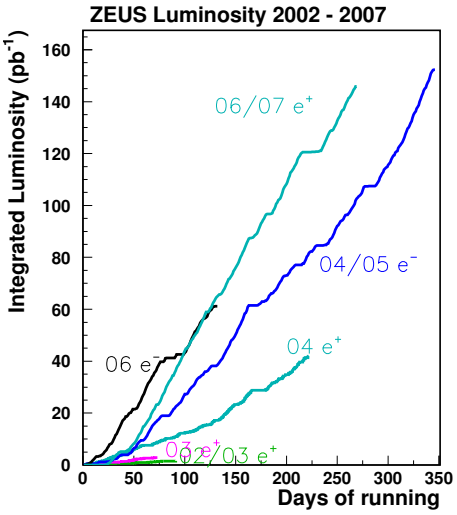

Figure 6.1: Integrated luminosity gated by the ZEUS detector in years 2002 - 2007 split into periods of data taking. Figure taken from [3]

FLT: DIS

FLT DIS was a first level trigger that selected deep inelastic scattering events. Event was accepted if at least one of the following trigger slots fired.

- FLT28 and FBISOE[1]
- FLT30
- FLT40
- FLT41
- FLT43
- FLT44
- FLT46
- FLT47 - active since 07.03.2005
- FLT62

Detailed description of FLT logic can be found in [79].

SLT: SPP02

SPP02 was a diffractive DIS second level trigger.

- difference between total energy deposited in calorimeter and total momentum along the beam line reconstructed with calorimeter cells had to be greater than 30 GeV
- one of the following conditions had to be fulfilled

[1]FCAL00_isol_e or FCAL01_isol_e or FCAL02_isol_e or FCAL03_isol_e or (FLT_TRKCL $>$ 1 and (BCAL08_isol_e or BCAL09_isol_e or BCAL10_isol_e or BCAL11_isol_e or BCAL12_isol_e or BCAL13_isol_e or BCAL14_isol_e or BCAL15_isol_e))

  - energy deposited in rear electromagnetic calorimeter had to be greater than 2.5 GeV
  - energy deposited in barrel electromagnetic calorimeter had to be greater than 2.5 GeV
  - energy deposited in forward electromagnetic calorimeter had to be greater than 10 GeV
  - energy deposited in forward hadronic calorimeter had to be greater than 10 GeV
- energy of scattered lepton candidate had to be greater than 5 GeV
- energy deposited in calorimeter cells closest to the beam pipe (fig. 6.2 on the following page) had to be smaller than 20 GeV
- event had to be accepted by a set of DIS first level trigger

TLT: SPP03

SPP03 was a diffractive DIS third level trigger. Trigger logic was as follows.

- all events that passed cuts were stored
- difference between total energy deposited in calorimeter and total momentum along the beam line measured with calorimeter cells had to be between 30 GeV and 100 GeV
- energy of scattered lepton candidate was required to be greater than 4 GeV
- position of scattered lepton candidate in calorimeter was required to be not too close to the beam pipe, i.e. outside the square with 12 cm sides centred on the beam pipe
- energy deposited in calorimeter cells closest to the beam pipe (fig. 6.2 on the next page) had to be smaller than:
  - 10 GeV in years 2006-2007
  - 20 GeV in years 2003-2005
- event had to be accepted by SPP02 second level trigger

6.2.1 Trigger Efficiency

Trigger efficiency has been checked in order to verify if online selection causes any bias in the measurement. The efficiency can be calculated with the use of event sample selected by a trigger which is independent of the one under consideration. In this analysis DST9 trigger, which requires good lepton candidate, is chosen. Additionally all offline selection criteria described in sec. 6.3 to sec. 6.7 on pages 53–59 are imposed on the control sample. Trigger efficiency is calculated as a ratio of number of control sample events accepted by the DST50 trigger slot to all events in the control sample

$$\epsilon_{DST9}^{DST50} = \frac{N^{DST9 \wedge DST50}}{N^{DST9}} \,. \tag{6.1}$$

A comparison between trigger efficiency obtained from data and MC is presented in fig. 6.3 on the following page. The MC agrees with data within statistical uncertainties. It is enough to use MC to correct for trigger efficiency.

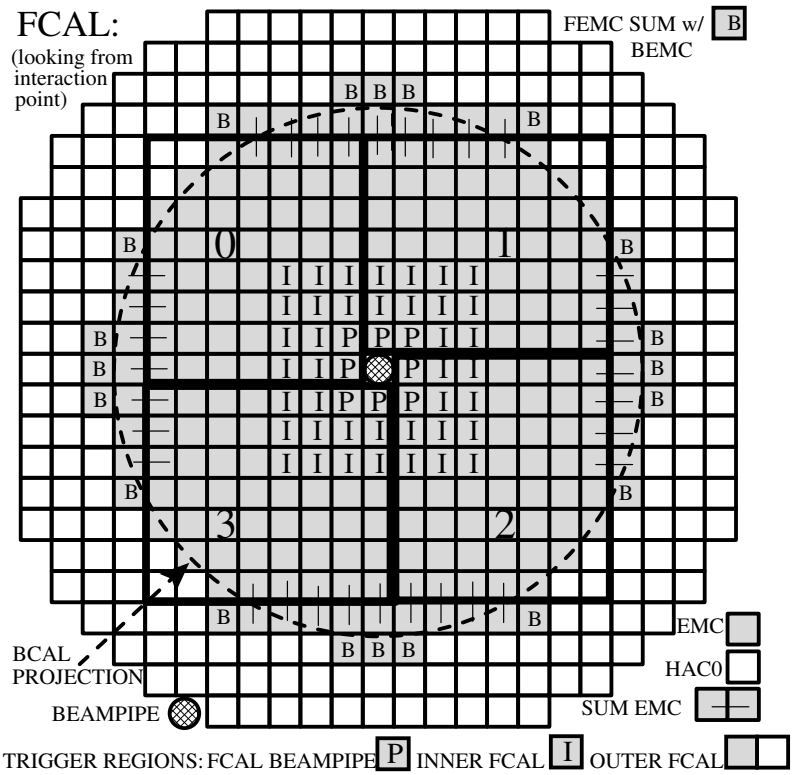

Figure 6.2: Taken from [4]. View from the interaction point of the FCAL trigger regions and trigger towers.

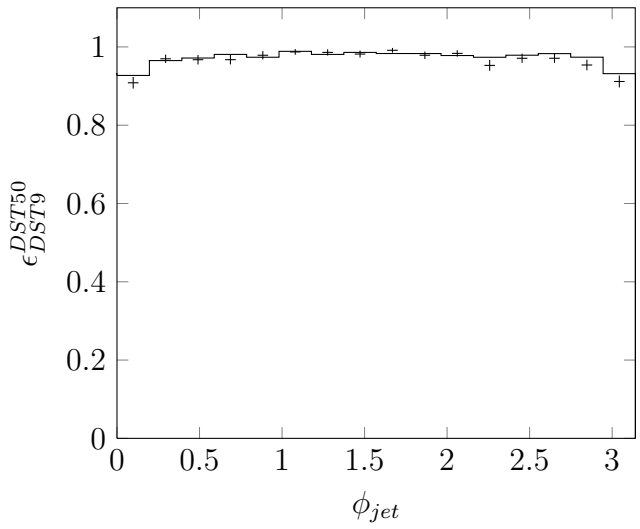

Figure 6.3: Trigger efficiency as a function of jet azimuthal angle. Black points show distribution of trigger efficiency calculated with data and statistical uncertainties. Histogram shows trigger efficiency calculated with MC.

6.3 DIS Selection

Out of online preselected diffractive DIS events a clean sample of deep inelastic scattering was selected with full offline information available. The following selection criteria provided a sample with well identified and reconstructed scattered lepton.

$\mathcal{P}_{e'} > \mathbf{0.9}$ Exactly one scattered lepton candidate with Sinistra (sec. 5.2) probability of being the scattered lepton greater than 0.9 is required. In case there are more than one scattered lepton candidates, probabilities of the others has to be smaller than 0.9. This requirement ensures good scattered lepton identification. Distribution of scattered lepton probability is shown in tab. A.17 on page 103.

$E_{e'} > \mathbf{10\ GeV}$ Energy of scattered lepton candidate reconstructed with double-angle method greater than 10 GeV reduces probability that a photon is identified as a scattered lepton, thus suppressing photoproduction background. Additionally, required scattered lepton minimal energy ensures high efficiency of Sinistra (sec. 5.2) algorithm and allows for precise reconstruction of momentum. Distribution of scattered lepton energy reconstructed with double-angle method is shown in figure 6.4a on the following page.

Track If position of the scattered lepton is reconstructed in the range of CTD i.e. $23^\circ < \theta_0 < 156^\circ$, a track associated with the scattered lepton is required. θ_0 is polar angle of energy deposit measured from the nominal interaction point. The distance between the calorimeter energy deposit and the track extrapolated to the calorimeter cannot be larger than 20 cm. This cut rejects events with neutral particle identified as scattered lepton. Distribution of distance of the extrapolated track from the calorimeter energy deposit is shown in figure 6.4b on the next page.

Position Cuts Events with scattered lepton reconstructed in certain areas are rejected. These are the regions in which scattered lepton had to pass substuntial amount of inactive material before being detected or regions with poor acceptance. Accuracy of the lepton momentum reconstruction is significantly lower in these areas.

- too close to the beampipe

$$\sqrt{X_{e'}^2 + Y_{e'}^2} < 18 \text{ cm} \tag{6.2}$$

- the region of cooling pipes

$$\begin{cases} \text{-14 cm} < X_{e'} < 12 \text{ cm} \\ \text{90 cm} < Y_{e'} \\ Z_{e'} < \text{-148 cm} \end{cases} \tag{6.3}$$

- the joins of calorimeter sections

$$\begin{array}{rcl} \text{-104 cm} < & Z_{e'} & < \text{-98.5 cm} \\ \text{164 cm} < & Z_{e'} & < \text{174 cm} \end{array} \tag{6.4}$$

Scattered lepton position in plane perpendicular to the beam pipe is shown in fig. 6.5 on the following page.

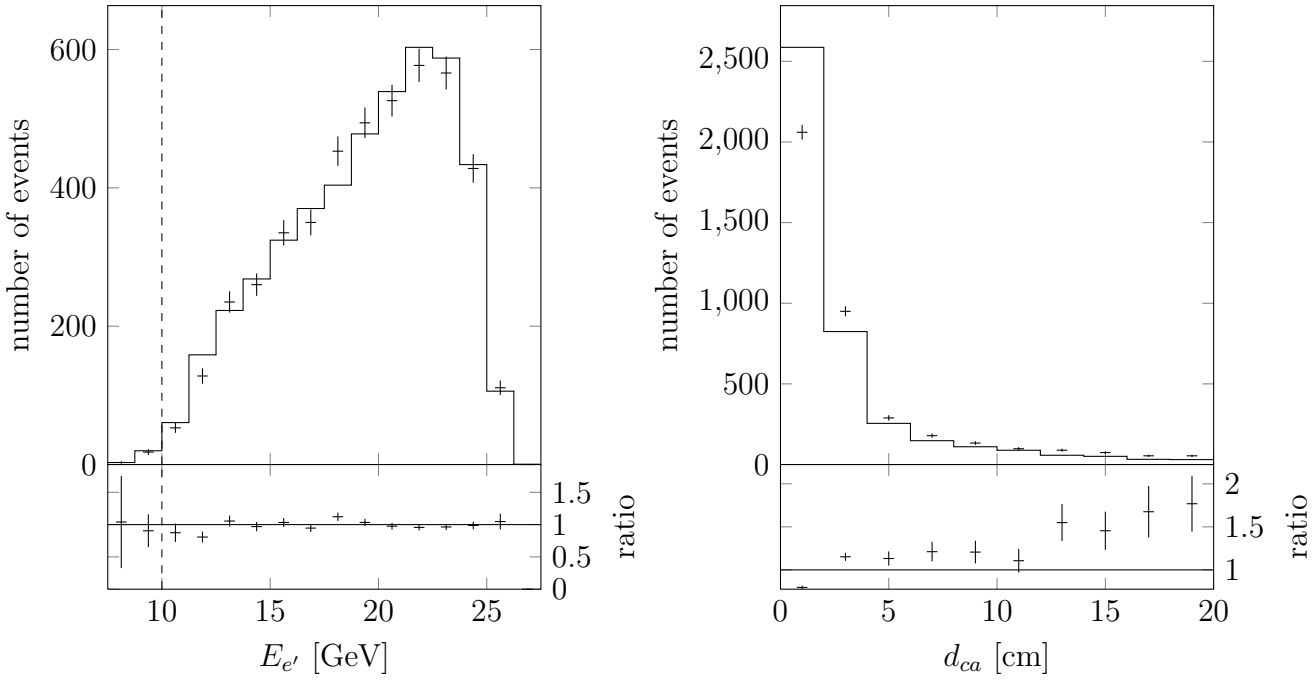

Figure 6.4: Control distributions of scattered lepton energy reconstructed with double-angle method (on the left) and distance separating scattered lepton energy deposit in calorimeter from extrapolated track associated with it (on the right). Black points show distribution of data with statistical uncertainties. Black histograms show SATRAP distributions. Dashed lines show cut values.

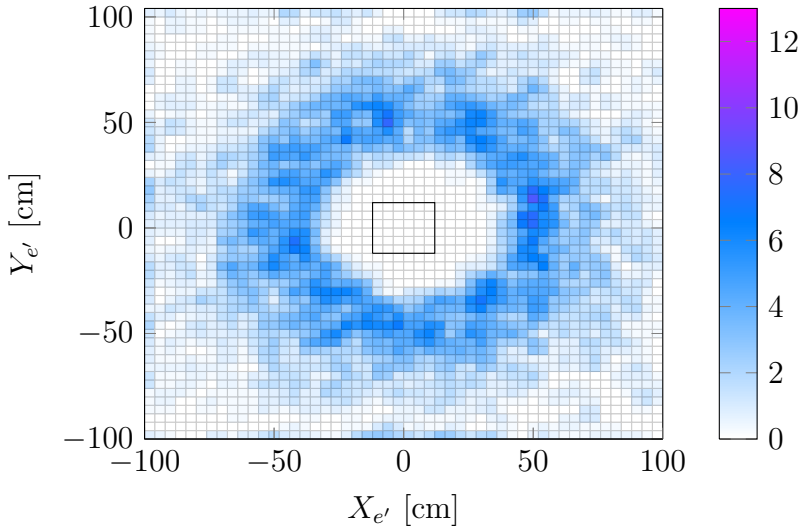

Figure 6.5: Scattered lepton reconstructed position (black solid line shows the TLT box cut).

6.4 Event Selection

Additional selection criteria were applied to improve quality of sample.

$|Z_{\text{vtx}}| < \mathbf{30\ cm}$ Vertex cannot be shifted more than 30 cm along the beam pipe from the nominal interaction point. This requirement reduces beam-gas background, which vertices are evenly distributed along the beam pipe. It also ensures that event is fully contained in the detector. Distribution of vertex position along the beam pipe is shown in figure 6.6a on the next page.

$N_{\text{trk}} > \mathbf{0}$ A track associated with the vertex significantly improves reconstruction of the vertex coordinates. Distribution of number of tracks associated with vertex is shown in figure 6.6b on the following page.

$N_{\mathbf{EFO}} > \mathbf{3}$ Diffractive final state should consist of at least four EFO. Two parton events are of interest to this analysis, thus it is expected that hadronisation results in at least four particles. Distribution of number of EFOs is shown in figure 6.6c on the next page.

$E_{\text{had}}/E_{\text{tot}} > \mathbf{0.06}$ At least 6% of total energy deposited in calorimeter has to be deposited in hadronic part. This cut removes purely electromagnetic events that mimic jets e.g. J/Ψ production. Distribution of fraction of total energy deposited in hadronic calorimeter is shown in figure 6.6d on the following page.

$\mathbf{45\ GeV} < E_{\mathbf{tot}} - p_{z,\mathbf{tot}} < \mathbf{70\ GeV}$ Difference between the total energy of an event and its momentum along the beam line is expected to be equal twice the incoming lepton energy $E_{\text{tot}} - p_{z,\text{tot}} = 55$ GeV. This is the consequence of momentum conservation eq. 2.44 on page 7. Substitution of parton level quantities with their detector level equivalents yields

$$2E_e = 55\ \text{GeV} = E_h - p_{z,h} + E_{e'} - p_{z,e'} = E_{\text{tot}} - p_{z,\text{tot}}\,. \tag{6.5}$$

The final state balance is insensitive to proton remnants escaping through the beam pipe. Undetected particles momenta along the beam pipe are almost equal their energies, thus they do not contribute. The balance is sensitive to particles going in opposite direction, which origin in most cases is lepton. Particles with large transverse momentum also significantly contribute to the balance. Thus, this quantity gives information if event was well contained within the detector. It also helps to remove events with ISR. Emitted photons escape through the beam pipe and all kinematic variables are incorrectly reconstructed. Restricting allowed values of $E_{\text{tot}} - p_{z,\text{tot}}$ suppresses photoproduction events, which due to lack of scattered lepton are characterised by small $E_{\text{tot}} - p_{z,\text{tot}}$ values. Distribution of energy-momentum along the beam pipe balance is shown in figure sec. 6.4 on page 57.

6.5 Diffractive Selection

Diffractive events were selected with the following criteria.

$\eta_{\text{max}} < 2$ Pseudorapidity of every EFO with energy greater than 400 MeV has to be smaller than 2. This criterion selects events with large rapidity gap, which is a signature of diffractive process. This requirement ensures pseudorapidity gap in forward region of at least 2.27 (see sec 3.2.1 on page 24). Distribution of maximal pseudorapidity of EFO with energy greater than 400 MeV is shown in figure 6.8a on page 58.

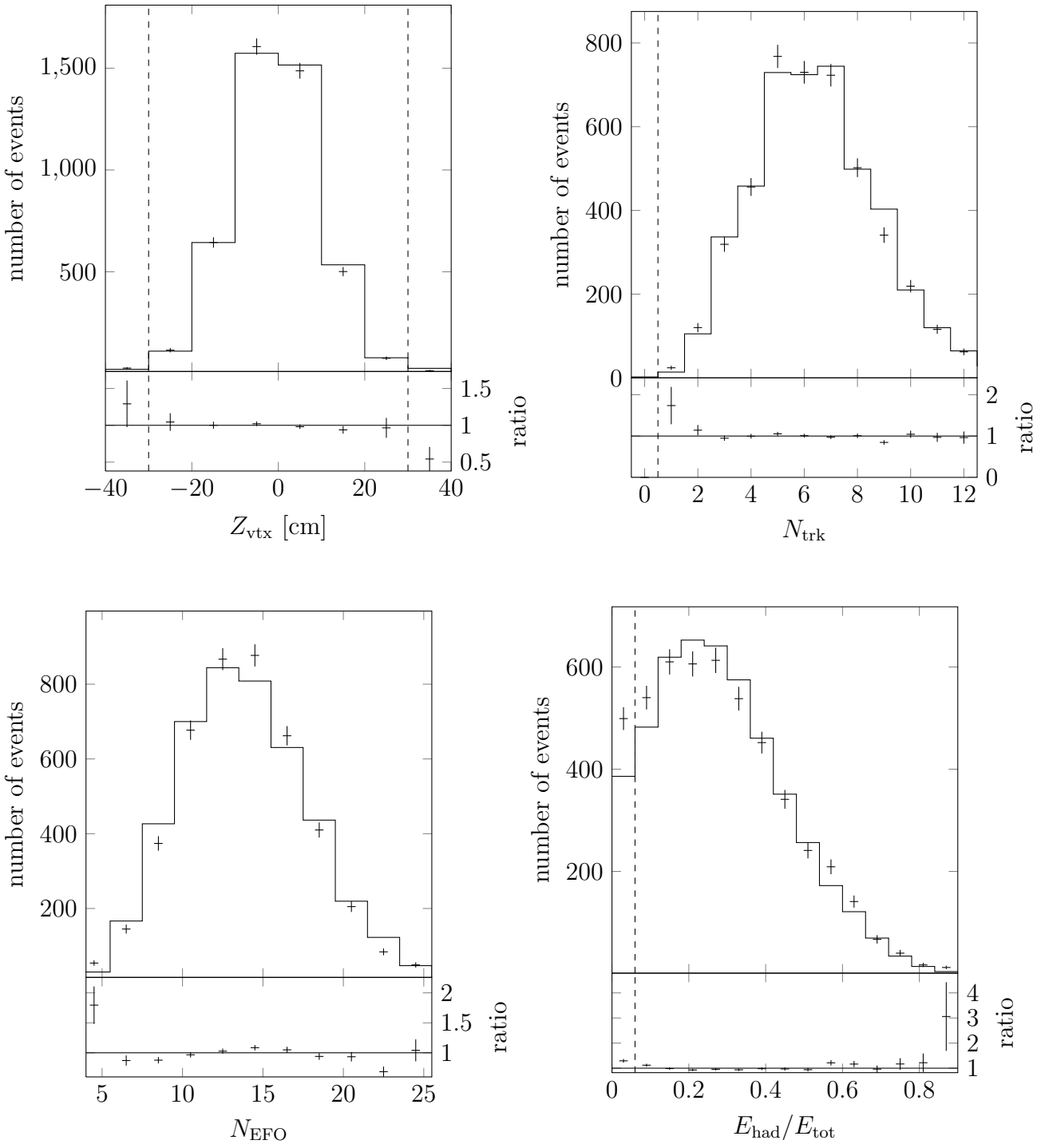

Figure 6.6: Control distributions of vertex position along the beam pipe (on the left) and number of tracks associated with the vertex (on the right) are shown in the upper row. Control distributions of number of EFOs in diffractive final state (on the left) and fraction of total energy deposited in hadronic calorimeter (on the right) are presented in the lower row. Black points show distribution of data with statistical uncertainties. Black histograms show SATRAP distributions. Dashed lines show cut values.

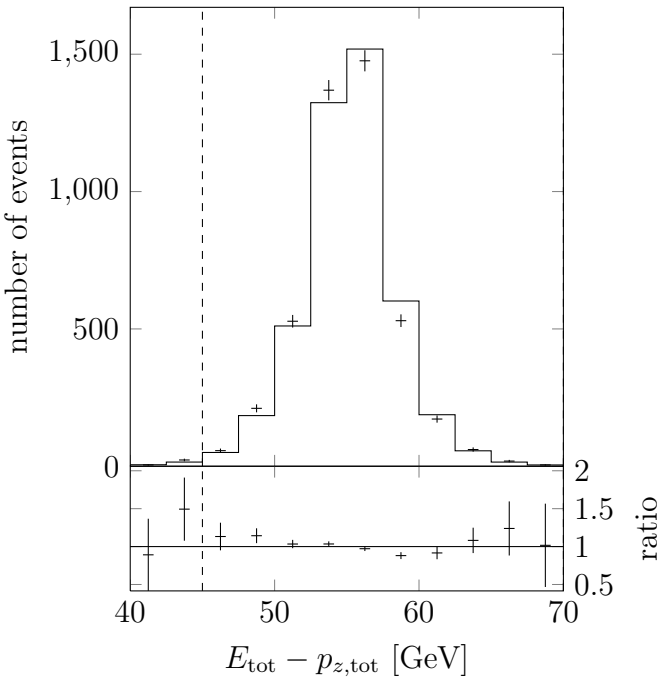

Figure 6.7: Control distribution showing energy-momentum along the beam pipe balance. Black points show distribution of data with statistical uncertainties. Black histograms show SATRAP distributions. Dashed lines show cut values.

$x_{\mathbb{P}} < \mathbf{0.01}$ Diffractive events are characterised by small momentum exchange at proton vertex. Requirement of pomeron momentum to be smaller than 1% of incoming proton momentum suppresses non-diffractive events. Distribution of reconstructed fraction of incoming proton momentum carried by pomeron is shown in figure 6.8b on the next page.

$M > \mathbf{5\ GeV}$ High invariant mass of diffractive system ensures there are no events with resonant particle production and there is enough energy in the system to create two jets with high transverse momentum. Distribution of invariant mass of diffractive system is shown in figure 6.8c on the following page.

$\mathbf{0.5} < \beta < \mathbf{0.7}$ Fraction of pomeron momentum carried by the interacting parton greater than 0.5 suppresses three-parton events and upper limit of 0.7 suppresses two-parton events originating from longitudinally polarised photon (see sec. 2.5 on page 20). Distribution of the pomeron momentum fraction is shown in figure 6.8d on the following page.

6.6 Kinematic Region

A kinematic region that is compatible with above selection was chosen.

$Q^2_{\mathbf{DA}} > \mathbf{25\ GeV^2}$ Kinematic region of photon virtuality reconstructed with double-angle method is determined by the fraction of pomeron momentum carried by the interacting parton and mass of diffractive system. Dependence of Q^2 on β and M can be derived from eq. 2.72 on page 12

$$\beta \approx \frac{Q^2}{Q^2 + M^2} \tag{6.6}$$

$$Q^2 \approx \frac{\beta M^2}{1 - \beta}\,. \tag{6.7}$$

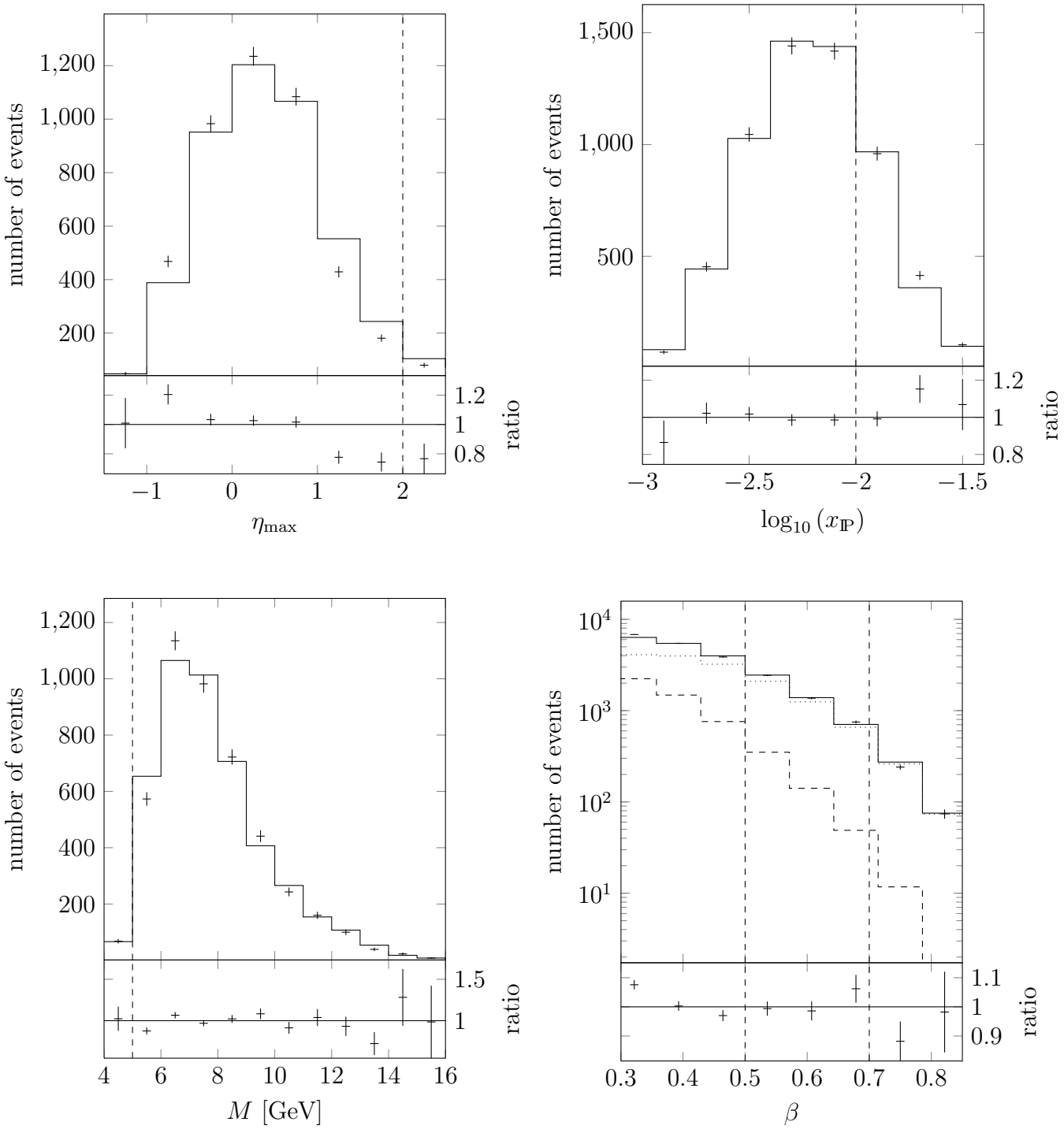

Figure 6.8: Control distributions of maximal pseudorapidity of EFOs with energy greater than 400 MeV (on the left) and reconstructed fraction of incoming proton momentum carried by the pomeron (on the right) are shown in the upper row. Control distributions of invariant mass of diffractive system (on the left) and fraction of pomeron momentum carried by the interacting parton (on the right) are shown in the lower row. Dashed histogram shows number of three parton events ($q\bar{q}g$), dotted — two parton events ($q\bar{q}$). Black points show distribution of data with statistical uncertainties. Black histograms show SATRAP distributions. Dashed lines show cut values.

Taking into account diffractive event selection ($\beta > 0.5, M > 5$ GeV), $Q^2_{\mathrm{DA}} > 25$ GeV^2 is obtained. Distribution of photon virtuality is shown in figure 6.9a on the following page.

90 GeV $< W_{\mathbf{DA}} <$ 250 GeV Allowed values of photon-proton invariant mass reconstructed with double-angle method were determined by diffractive selection criteria and photon virtuality. Approximate limits of W can be estimated with basic kinematic relations: lower limit according to eq. 2.34 on page 6 and eq. 2.75 on page 12 equals

$$W \approx \sqrt{\frac{Q^2}{x}} = \sqrt{\frac{Q^2 + M^2}{x_{\mathbb{P}}}} = 67 \text{ GeV}\,, \tag{6.8}$$

upper limit according to eq. 2.37 on page 6

$$W \approx \sqrt{\frac{Q^2}{x}} = \sqrt{y\left(s - m_p^2\right)} = \sqrt{\frac{E_e - E_{e'}}{E_e}\left(s - m_p^2\right)} = 254 \text{ GeV}\,. \tag{6.9}$$

Lower limit is additionally restricted by rapidity gap requirement. Therefore there are no events with photon-proton invariant mass lower than 70 GeV. Distribution of W reconstructed with double-angle method is shown in figure 6.9b on the following page.

0.1 $< y_{\mathbf{El}} <$ 0.64 Inelasticity region calculated with electron method was narrowed by diffractive criteria and scattered lepton minimal energy. Upper limit can be calculated using inelasticity definition in incoming proton rest frame eq. 2.15 on page 4

$$y = \frac{E_e - E_{e'}}{E_e} = 0.64\,. \tag{6.10}$$

Lower limit can be calculated with eq. 2.37 on page 6 and eq. 2.75 on page 12

$$y = \frac{Q^2}{x\left(s - m_p^2\right)} = \frac{Q^2 + M^2}{x_{\mathbb{P}}\left(s - m_p^2\right)} = 0.04\,. \tag{6.11}$$

Just like in the case of photon-proton invariant mass, lower limit of inelasticity is additionally restricted by rapidity gap requirement. In this kinematic region good performance of double-angle method is expected. Distribution of inelasticity reconstructed with electron method is shown in figure 6.9c on the following page.

6.7 Jet Selection

Events with jets were selected with the following requirements and parameters.

$y_{\mathbf{cut}} = \mathbf{0.15}$ Jets are reconstructed with resolution parameter equal 0.15 (see sec. 5.5 on page 41). This value provides relatively high efficiency of reconstructing exactly two jets in two parton events, while still being able to reject some of the three parton events.

$N_{\mathbf{jets}} = \mathbf{2}$ Exactly two jets are required. No EFO can be discarded by the jet algorithm. Since the analysis is done in the centre of mass of diffractive system, reconstructed jets are back to back. Thus they have equal transverse momenta.

$p_{t,jet} > \mathbf{2\ GeV}$ Jets transverse momenta in virtual photon-pomeron centre of mass system have to be greater than 2 GeV. High transverse momentum allows for comparison of the result with QCD perturbative calculations. Distribution of jet transverse momentum is shown in fig. 6.10 on page 61.

Any jet laboratory frame cuts are avoided, since they alter virtual photon-pomeron centre of mass system distributions.

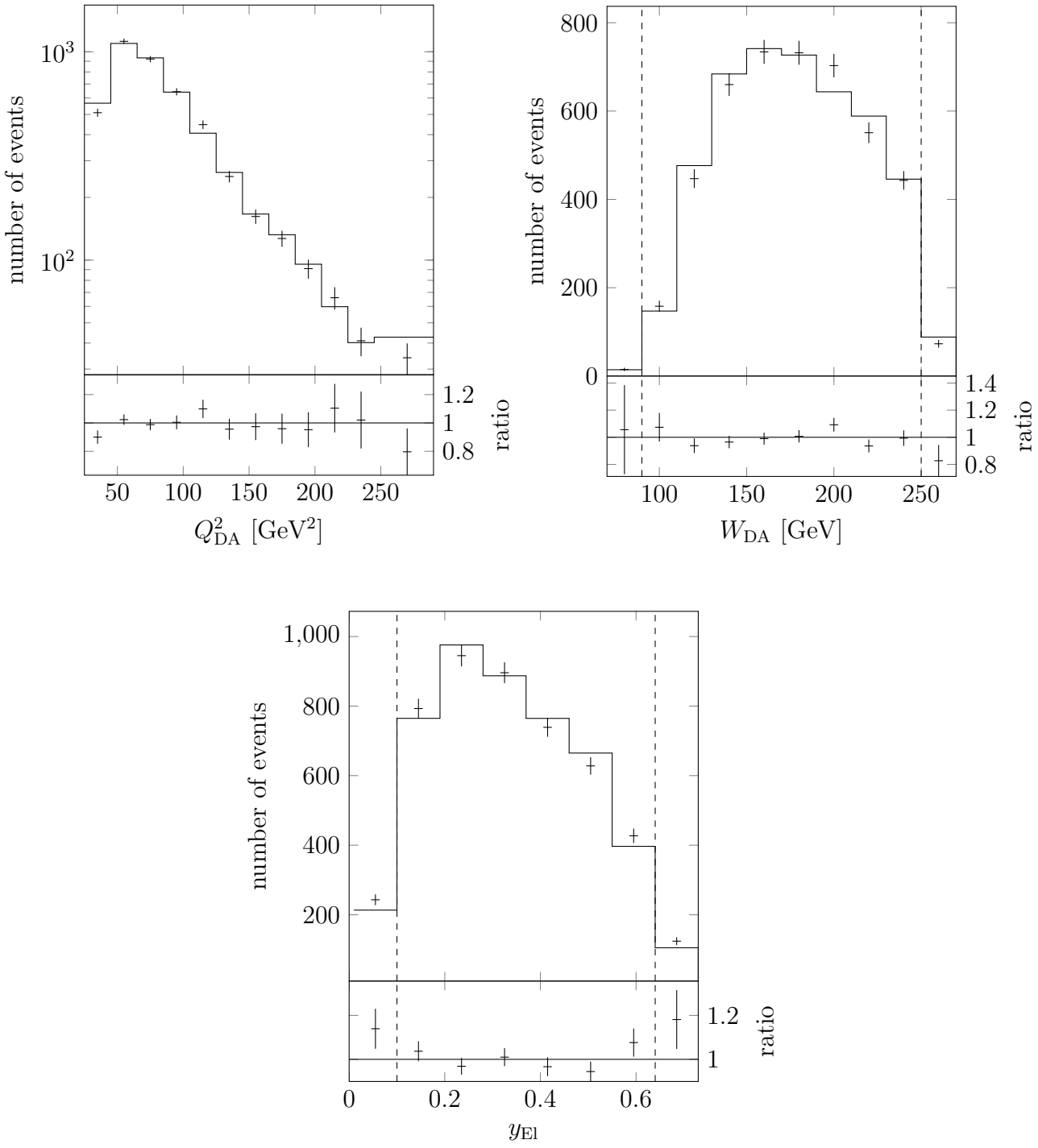

Figure 6.9: Control distributions of photon virtuality reconstructed with double-angle method (on the left) and photon-proton invariant mass reconstructed with double-angle method (on the right) are presented in the upper row. Below, a control distribution of inelasticity reconstructed with electron method is shown. Black points show distribution of data with statistical uncertainties. Black histograms show SATRAP distributions. Dashed lines show cut values.

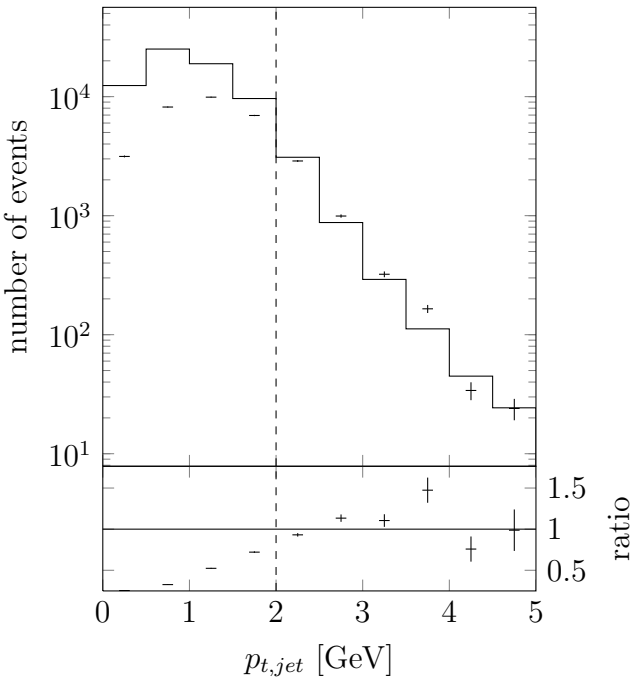

Figure 6.10: Control distribution showing jet transverse momentum in virtual photon-pomeron centre of mass system. Black points show distribution of data with statistical uncertainties. Black histograms show SATRAP distributions. Dashed lines show cut values.

6.8 Background Estimation

Very strict event selection is expected to provide a clean sample. Background studies confirm it.

Background originating from diffractive photoproduction in the studied kinematic region is negligible. It has been investigated with PYTHIA MC generated with $Q^2 < 2$ GeV^2. According to the Monte Carlo contribution from this background is expected to be smaller than 0.1%.

Another source of background that has been investigated is non-diffractive jet production in deep inelastic scattering. Ariadne MC generator was used to estimate the amount of this kind of background. The result is that the contribution is smaller than 1.6%. Requirement of large rapidity gap (> 2.27) and low fraction of incoming proton momentum carried by a pomeron ($x_{I\!P} < 0.01$) ensure small non-diffractive background. In case of shape studies curried out in this analysis, estimated amount of non-diffractive background is trifling. This background is not subtracted from the data.

Background originating from beam-gas interactions and cosmic events, has been estimated using information about empty bunches. No events recorded during empty bunch crossings pass the selection criteria. Out of 220 total bunches there were 30 empty. Thus contribution from this kind of background is negligible.

Significant background is expected from diffractive double dissociation. In this process not only photon, but also proton dissociates. Previous analysis indicate that this background amounts to 16%–19% [80, 81, 82]. However, it is expected that proton dissociation does not affect the lepton-proton interaction and can be factorised. Factorisation hypothesis has been confirmed in lepton-proton collisions at HERA I accelerator by ZEUS [83] and H1 [84] collaborations. by That means that this background does not affect the shapes of the distributions, which are of the interest in this analysis. Only the total cross section is affected by diffractive double dissociation. This background is not subtracted from the data.

Chapter 7

Cross Section Measurement and Discussion

There are two ways of comparing hadron level theoretical predictions with measurement.

One way is to build detector response function and use it to transform hadron level observables to detector level. In practice this is done with the help of computer simulation of the detector. ZEUS detector simulation is described in sec. 4.4 on page 30. The output of the simulation can be used just like real data, thus allowing for direct comparison of measurement with theory. The advantage of this method is that it is stable against small changes in hadron level distributions. The main disadvantage is that it cannot be used to compare results from different experiments with each other. Moreover the need of using the detector simulation with every theoretical prediction is very inconvenient and virtually is not possible in long term perspective.

The other approach of comparing data with theoretical predictions is to correct the data for detector effects. This method, usually referred to as data unfolding, allows of data comparison between experiments. However, it can be unstable against fluctuations in detector level distributions. There are several implementations of the method.

7.1 Unfolding

One of the most basic unfolding technique is called bin-by-bin corrections. Firstly, hadron and detector level distributions of MC samples are calculated. Next, a correction factor for each bin of a distribution is calculated. The correction is ratio of number of events in the corresponding bin on hadron and detector level. Finally, each bin of the measured distribution is multiplied by the factor. This method requires very good description of data by Monte Carlo since event migrations from one bin to another are determined only from the MC.

More advanced procedure determines event migrations based on data. It requires the use of detector response function $A(\overline{x}, x)$. The function determines dependence of distribution $f(x)$ of hadron level variable x on distribution $g(\overline{x})$ of corresponding detector level variable $\overline{x}$

$$g(\overline{x}) = \int A(\overline{x}, x)\, f(x) dx\,. \tag{7.1}$$

In practice, detector level measurement results are not a continues function, but are discrete distribution of numbers of events. Detector response function is also not available, only detector simulation can be used. Thus the above equation is used in matrix notation

$$\overline{\mathrm{x}} = \mathrm{Ax}\,. \tag{7.2}$$

Vectors $\mathrm{x}, \overline{\mathrm{x}}$ correspond to hadron and detector level histograms. Vector element x_i is equal to number of events in bin i of hadron level histogram. A is detector response matrix. The matrix is constructed using detector simulation. Matrix element A_{ij} is equal to the number of events with detector level variable corresponding to vector element $\overline{\mathrm{x}}_i$ and hadron level variable corresponding to vector element x_j.

In principle it is enough to solve eq. 7.2 on the preceding page with respect to detector level distribution x

$$\mathrm{x} = \mathrm{A}^{-1}\overline{\mathrm{x}}\,. \tag{7.3}$$

However distribution measured in experiment x is different from $\overline{\mathrm{x}}$ due to statistical fluctuations. The fluctuations are amplified in unfolding process and result might be unstable. In order to overcome this problem regularisation is introduced.

In this analysis TUnfold [85] package available in ROOT framework [86] is used. TUnfold is based on least square method with Tikhonov regularisation [87, 88]. The function used in minimisation consists of two addends

$$\chi^2 = (\mathrm{x} - \mathrm{Ax})^\intercal\, \mathrm{V}^{-1}\, (\mathrm{x} - \mathrm{Ax}) + \tau^2 ||\mathrm{x}||^2\,. \tag{7.4}$$

The first term is the standard least square formula with V being the covariance matrix of measured distribution. The second summand is regularisation condition with parameter τ defining the strength of the regularisation. It is determined using the L-curve [89] scan. The L-curve is build by plotting logarithm of solution norm $||\mathrm{x}||$ against logarithm of corresponding residual norm $||\mathrm{x} - \mathrm{Ax}||$ for different values of τ. The curve visualises trade off between the quality of the fit and size of the solution. Limitation of the solution size dumps contributions from statistical fluctuations of the data. The best regularisation parameter is the one that maximises curvature of the L-curve. The curvature is defined as

$$C = \frac{\frac{d^2L_y}{dt^2}\frac{dL_x}{dt} - \frac{d^2L_x}{dt^2}\frac{dL_y}{dt}}{\left(\left(\frac{dL_x}{dt}\right)^2 + \left(\frac{dL_y}{dt}\right)^2\right)^{3/2}}\,, \tag{7.5}$$

where

$$L_x = \log\left((\mathrm{x} - \mathrm{Ax})^\intercal\, \mathrm{V}^{-1}\, (\mathrm{x} - \mathrm{Ax})\right)\,, \tag{7.6}$$

$$L_y = \log\left(||\mathrm{x}||^2\right)\,, \tag{7.7}$$

$$t = \log(\tau)\,. \tag{7.8}$$

Derivatives are approximated using cubic spline parametrisation of the scan results.

It is recommended to use finner binning on detector than on hadron level when using unfolding. This ensures non-zero degrees of freedom in least square minimisation and avoid the so called "inverse crime". Numerical methods used to solve the inverse problem tend to state the problem less ill-posed than it really is. This leads to too optimistic results.

In this analysis the unfolding method is used to obtain hadron level distributions in the following kinematic region:

$$90\ \mathrm{GeV} < W < 250\ \mathrm{GeV} \tag{7.9}$$

$$25\ \mathrm{GeV}^2 < Q^2 \tag{7.10}$$

$$x_{\mathbb{P}} < 0.01 \tag{7.11}$$

$$0.5 < \beta < 0.7 \tag{7.12}$$

$$N_{\mathrm{jets}} = 2 \tag{7.13}$$

$$2\ \mathrm{GeV} < p_{t,jet^{\mathrm{had}}}\,. \tag{7.14}$$

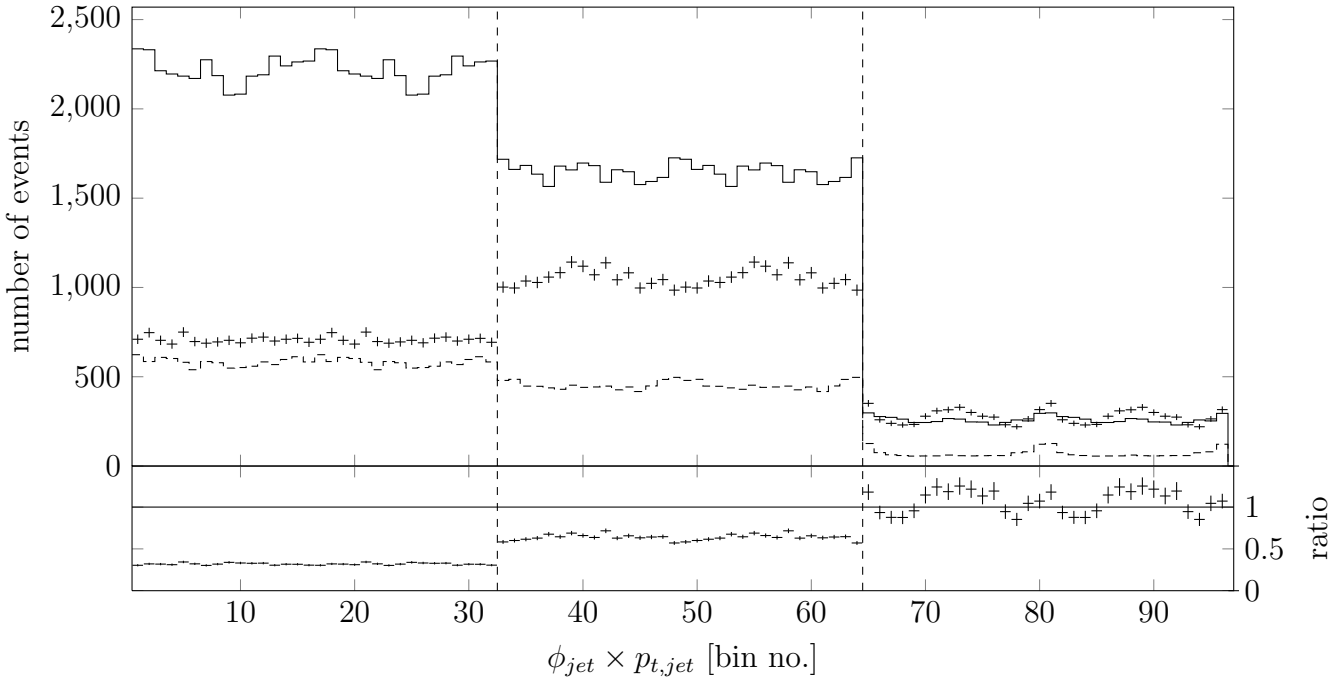

Figure 7.1: Two dimensional distribution of jet azimuthal angle and transverse momentum. Jet azimuthal angular distribution is measured in 32 bins of equal size covering range of $\phi_{jet} \in [-\pi, \pi]$. Vertical dashed lines separate transverse momentum bins. The following edges of transverse momentum bins in GeV are used: 0, 1, 2, 10. This means that the distribution before the first dashed line corresponds to transverse momentum between 0 GeV and 1 GeV, the distribution between the first and second dashed line corresponds to transverse momentum from 1 GeV to 2 GeV and between the second and third dashed line corresponds to transverse momentum from 2 GeV to 10 GeV. Dashed histogram shows contribution from events that lay outside of the studied kinematic region (eq. 7.9 to eq. 7.14 on the facing page).

Contribution from the events that lay outside of this region is subtracted from the data before unfolding. The subtracted distributions are calculated with SATRAP MC (sec. 4.1 on page 29). The unfolded distribution is corrected for detector efficiency.

7.1.1 2D Unfolding

In this analysis two dimensional unfolding, in jet azimuthal angle and jet transverse momentum, is performed. Two dimensional measured distribution is saved as one dimensional histogram of $n_\phi \times n_{p_{t,}}$ bins. First n_ϕ bins are jet azimuthal angular distribution of the first bin of $p_{t,}$, second n_ϕ are jet azimuthal angular distribution of the second bin of $p_{t,}$, etc. On detector level azimuthal angle distribution is measured in range $\phi_{jet} \in [-\pi, \pi]$ divided into 32 bins of equal size. Jet transverse momentum distribution consists of 3 bins (in GeV): [0, 1), [1, 2), [2, 10). Detector level distribution used in unfolding is shown in fig. 7.1. Unfolded hadron level distribution consists of 16 bins in azimuthal angle and 2 bins in transverse momentum (in GeV): [0, 2), [2, 10). In order to obtain unfolded one dimensional distribution of jet azimuthal angle, a projection of bins corresponding to jet transverse momentum greater than 2 GeV is done. In this case it is only the content of the second transverse momentum bin.

The same procedure is used in two dimensional unfolding of virtuality and jet transverse momentum. Photon virtuality distribution is divided into 12 bins (in GeV^2): [25, 45), [45, 65), [65, 85), [85, 105), [105, 125), [125, 145), [145, 165), [165, 185), [185, 205), [205, 225), [225, 245),

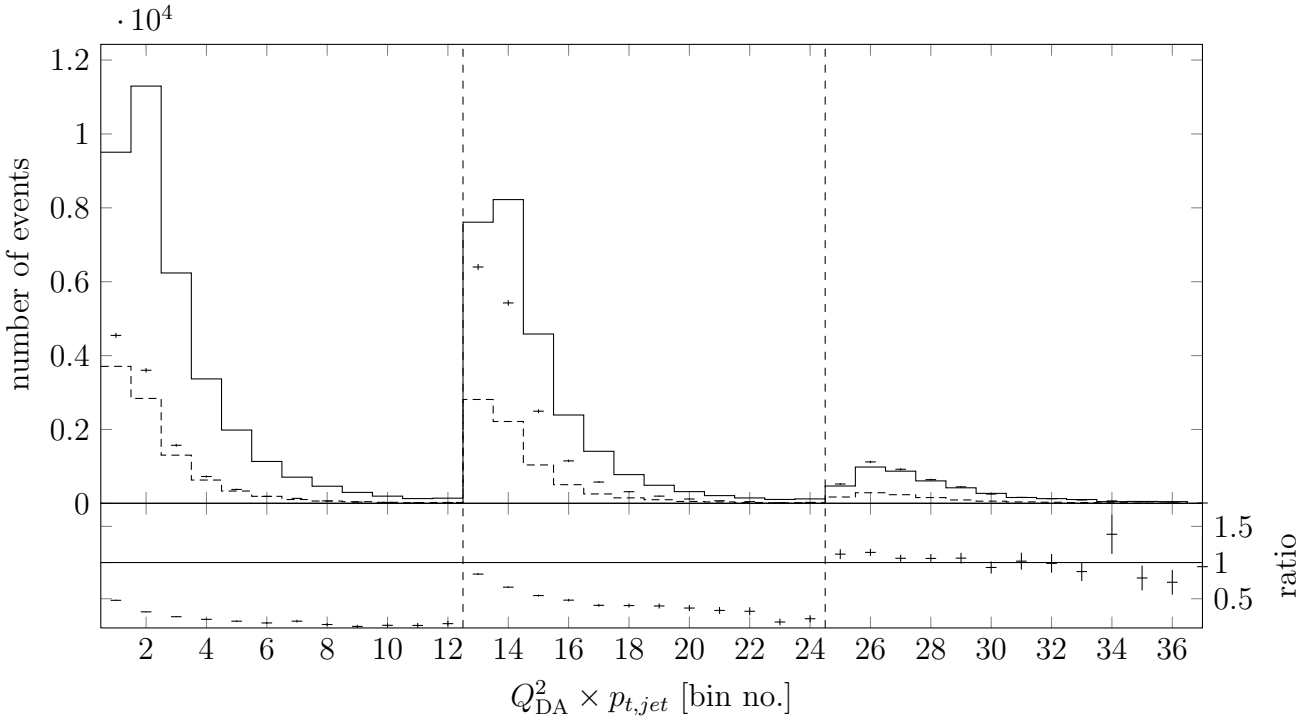

Figure 7.2: Two dimensional distribution of virtuality reconstructed with double-angle method and transverse momentum. Photon virtuality distribution consists of 12 bins corresponding to the following virtualities in GeV^2): [25, 45), [45, 65), [65, 85), [85, 105), [105, 125), [125, 145), [145, 165), [165, 185), [185, 205), [205, 225), [225, 245), [245, 295). Vertical dashed lines separate transverse momentum bins. The following edges of transverse momentum bins in GeV are used: 0, 1, 2, 10. This means that the distribution before the first dashed line corresponds to transverse momentum between 0 GeV and 1 GeV, the distribution between the first and second dashed line corresponds to transverse momentum from 1 GeV to 2 GeV and between the second and third dashed line corresponds to transverse momentum from 2 GeV to 10 GeV. Dashed histogram shows contribution from events that lay outside of the studied kinematic region (eq. 7.9 to eq. 7.14 on page 64).

[245, 295). Jet transverse momentum is also divided into 3 bins (in GeV): [0, 1), [1, 2), [2, 10). Detector level distribution used in unfolding is presented in fig. 7.2. Photon virtuality hadron level distribution consists of 7 bins (in GeV^2): [25, 50), [50, 65), [65, 105), [105, 145), [145, 185), [185, 225), [225, 295), while hadron level jet transverse momentum consists of 2 bins (in GeV): [0, 2), [2, 10).

7.2 Systematic Uncertainties

Apart from statistical uncertainties there are also uncertainties originating from measurement techniques and devices. These systematic uncertainties are estimated by calculating difference between result obtained with standard and varied settings for each bin of the distribution. Systematic uncertainty of a bin equals

$$\Delta_i = \mathrm{n}_i - \mathrm{n}_i^{sys} \,. \tag{7.15}$$

It is assumed that all uncertainties calculated by varying the same parameter are correlated, since they come from one source. Thus a covariance matrix corresponding to a source is a mean covariance obtained by varying a parameter up and down. It is calculated using the vector of

Table 7.1: Cuts variations investigated in systematic uncertainty studies.

cut	nominal value and variation								
photon virtuality	25	$\pm$	1.7	$<$	$Q^2_{\mathrm{DA}}/\mathrm{GeV}^2$				
proton-photon energy	90	$\mp$	7.4	$<$	$W_{\mathrm{DA}}/\mathrm{GeV}$	$<$	250	$\pm$	8.4
inelasticity	0.1	$\mp$	0.039	$<$	y_{El}	$<$	0.64	$\pm$	0.029
mass of diffractive system	5	$\pm$	1.2	$<$	M/GeV				
vertex position					$\lvert Z_{\mathrm{vtx}}\rvert/\mathrm{cm}$	$<$	30	$\pm$	1.5
pomeron					$x_{\mathbb{P}}$	$<$	0.01	$\pm$	0.0009
pseudorapidity gap					η_{max}	$<$	2	$\pm$	0.2
η_{max} energy threshold	0.4	$\pm$	0.1	$<$	E/GeV				

differences Δ

$$\mathrm{V}^{sys} = \left(\Delta_{\mathrm{low}}\Delta^{\intercal}_{\mathrm{low}} + \Delta_{\mathrm{high}}\Delta^{\intercal}_{\mathrm{high}}\right)/2\,. \tag{7.16}$$

The Covariance matrix of total systematic uncertainty is a sum of covariance matrices of each source.

The following sources of systematic uncertainties are considered:

- originating from the detector simulation - these effects are investigated by introducing changes only to MC samples, while data samples are not altered; the following checks are performed:
  1. scattered lepton position is varied by ± 2 mm in each direction according to [90]
  2. energy scale of the calorimeter is varied by 3 % according to results presented in [90, 91]
  3. calorimeter energy resolution is varied so that the χ^2 of the comparison of data to MC in distribution of ratio of diffractive system transverse momentum to scattered lepton transverse momentum is raised by 1
- originating from event selection - criteria used to select events are varied; limits of the selection criteria based on W, Q^2, y, $x_{\mathbb{P}}$, β and M are varied according to the resolution of a variable; the resolution can be different for different values of the variable, thus it has been studied and results are presented in fig. 7.3 on the following page and fig. 7.4 on page 69; additionally the η_{max} selection variation (in value and energy threshold) is based on previous analyses [92, 82, 93] and vertex Z coordinate is varied by 5 % according to [94]; performed checks are listed in tab. 7.1 and results are presented in fig. 7.5 on page 70
- originating from measurement technique:
  1. the ratio of MC events with $q\overline{q}$ system and $q\overline{q}g$ system is varied so that the χ^2 of the comparison of data to MC in distribution of fraction of pomeron momentum carried by the interacting parton (β) is raised by 1

Results of the above investigations considering jet azimuthal angular distribution are presented in fig. 7.5 on page 70 and fig. 7.6 on page 71. Results corresponding to virtuality distribution are shown in fig. 7.7 on page 72 and fig. 7.8 on page 73.

It is worth pointing out that the very large systematic error is associated with the first bin in photon virtuality distribution. The error comes almost exclusively from the shift in mass in event selection. This because mass of diffractive system, photon virtuality and fraction of pomeron momentum carried by the interacting parton (β) are connected with each other. A

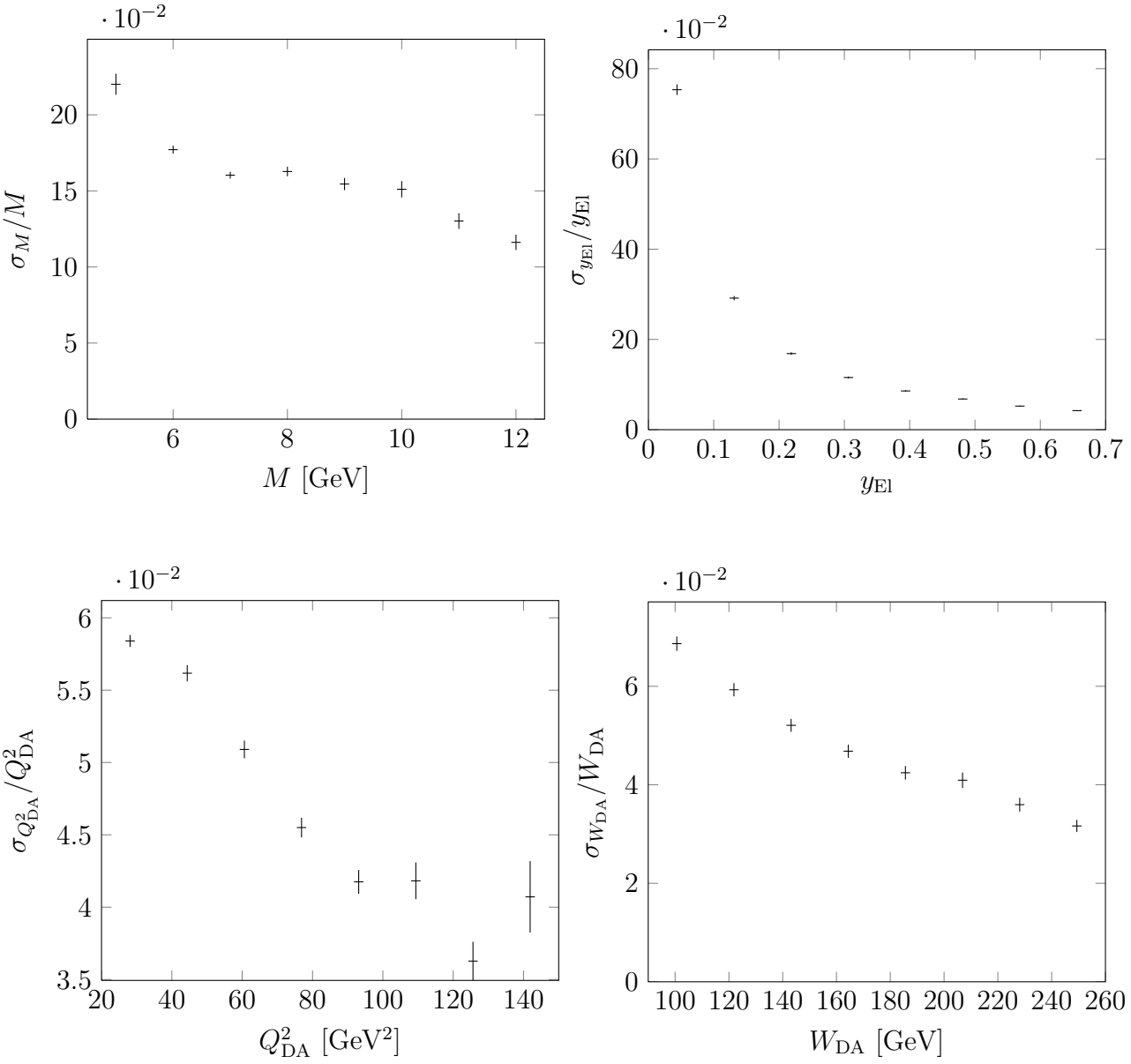

Figure 7.3: Resolutions of kinematic variables estimated with SATRAP as a function of the variables themselves. Resolutions of diffractive system mass (on the left) and inelasticity (on the right) are presented in the upper row. Resolutions of virtuality (on the left) and boson-proton centre of mass energy (on the right) are presented in the lower row.

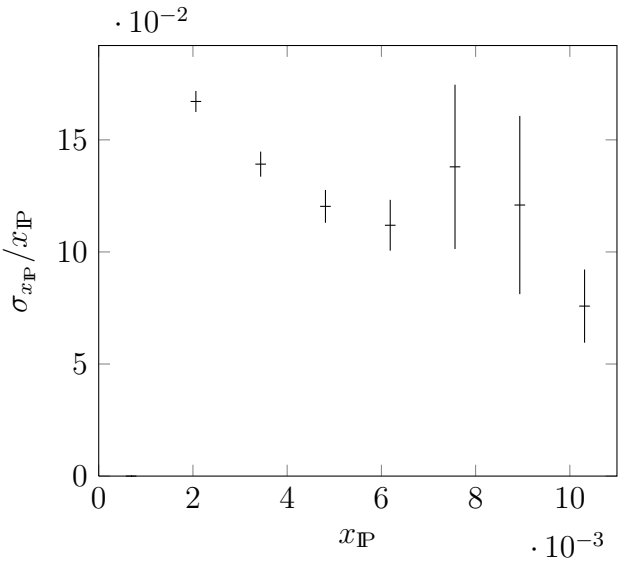

Figure 7.4: Resolution of fraction of incoming proton momentum carried by pomeron as a function of the variable itself estimated with SATRAP.

raise in cut of diffractive mass to $M = 6.2$ GeV is effectively a raise in cut of photon virtuality to $Q^2 = 38$ GeV^2. This significantly lowers number of events in the first bin (from 510 to 92) and introduce large statistical error. Thus this bin is not taken into account in further studies.

The influence of the jet resolution parameter y_{cut} on the result has also been investigated. Obtained shifts are presented in fig. 7.9 on page 74. Jet azimuthal angular distribution is stable with respect to the change in y_{cut}. A shift in overall normalisation is observed in case of photon virtuality distribution. These contributions are not added to systematic uncertainty, because in principle jets with different resolution parameters are different objects.

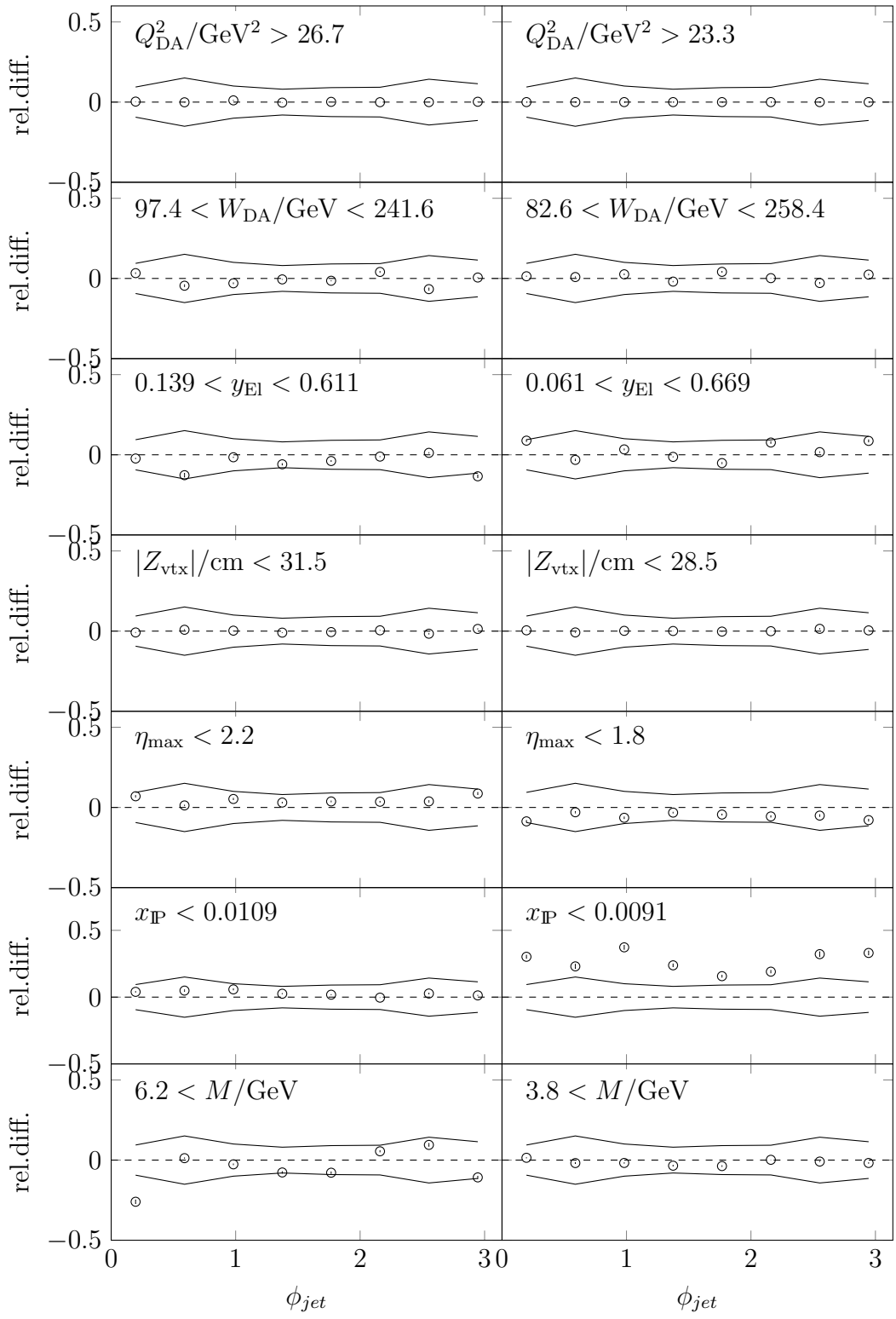

Figure 7.5: Systematic uncertainties of jet azimuthal angular distribution originating from event selection. Markers show relative differences between number of events obtained with nominal and varied measurement. Vertical error bars show statistical uncertainty. In most cases uncertainties are smaller than points and error bars are not visible. Lines show statistical uncertainty of the nominal result.

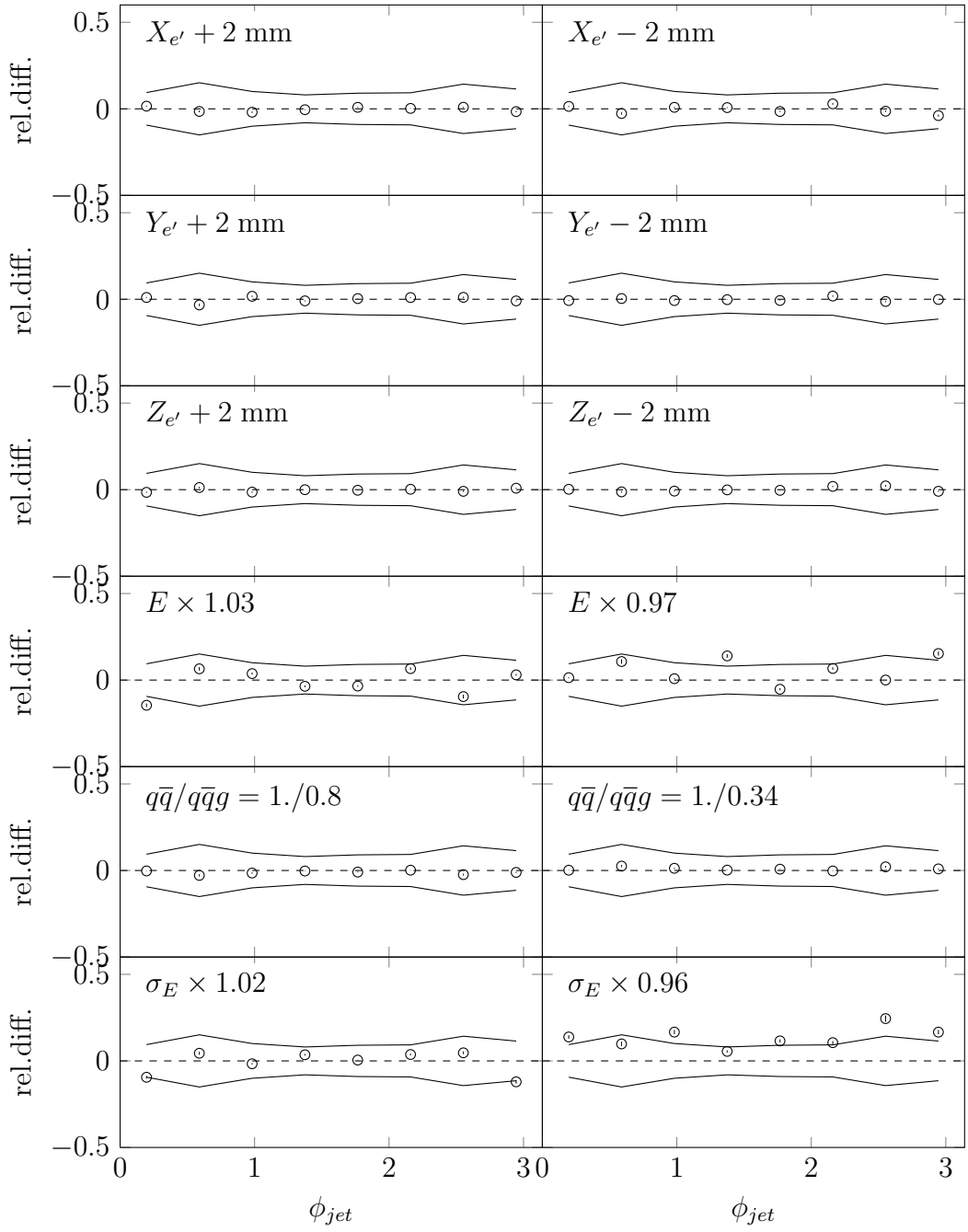

Figure 7.6: Systematic uncertainties of jet azimuthal angular distribution originating from detector simulation and measurement technique. Markers show relative differences between number of events obtained with nominal and varied measurement. Vertical error bars show statistical uncertainty. In most cases uncertainties are smaller than points and error bars are not visible. Lines show statistical uncertainty of the nominal result.

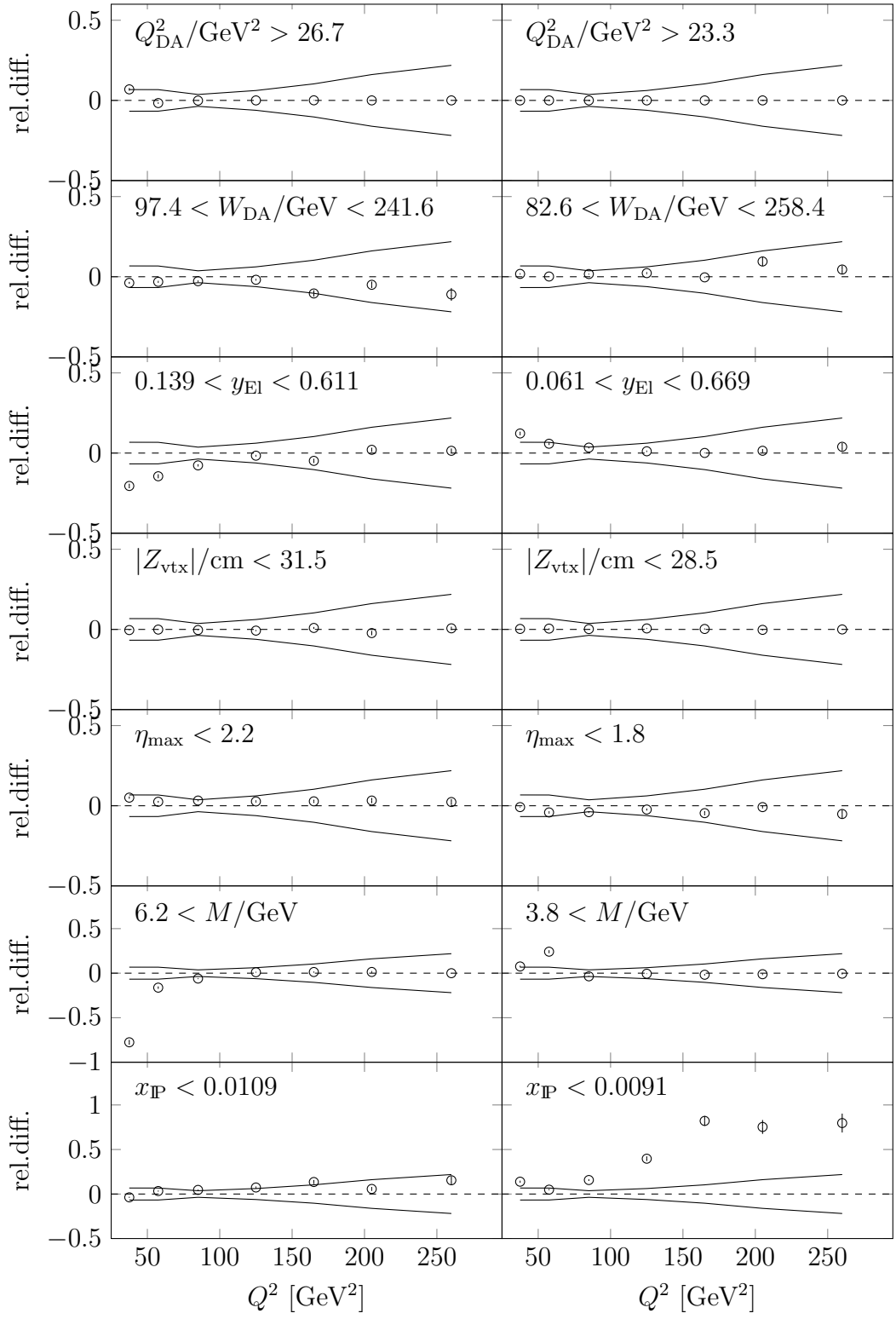

Figure 7.7: Systematic uncertainties of virtuality distribution originating from event selection. Markers show relative differences between number of events obtained with nominal and varied measurement. Vertical error bars show statistical uncertainty. In most cases uncertainties are smaller than points and error bars are not visible. Lines show statistical uncertainty of the nominal result.

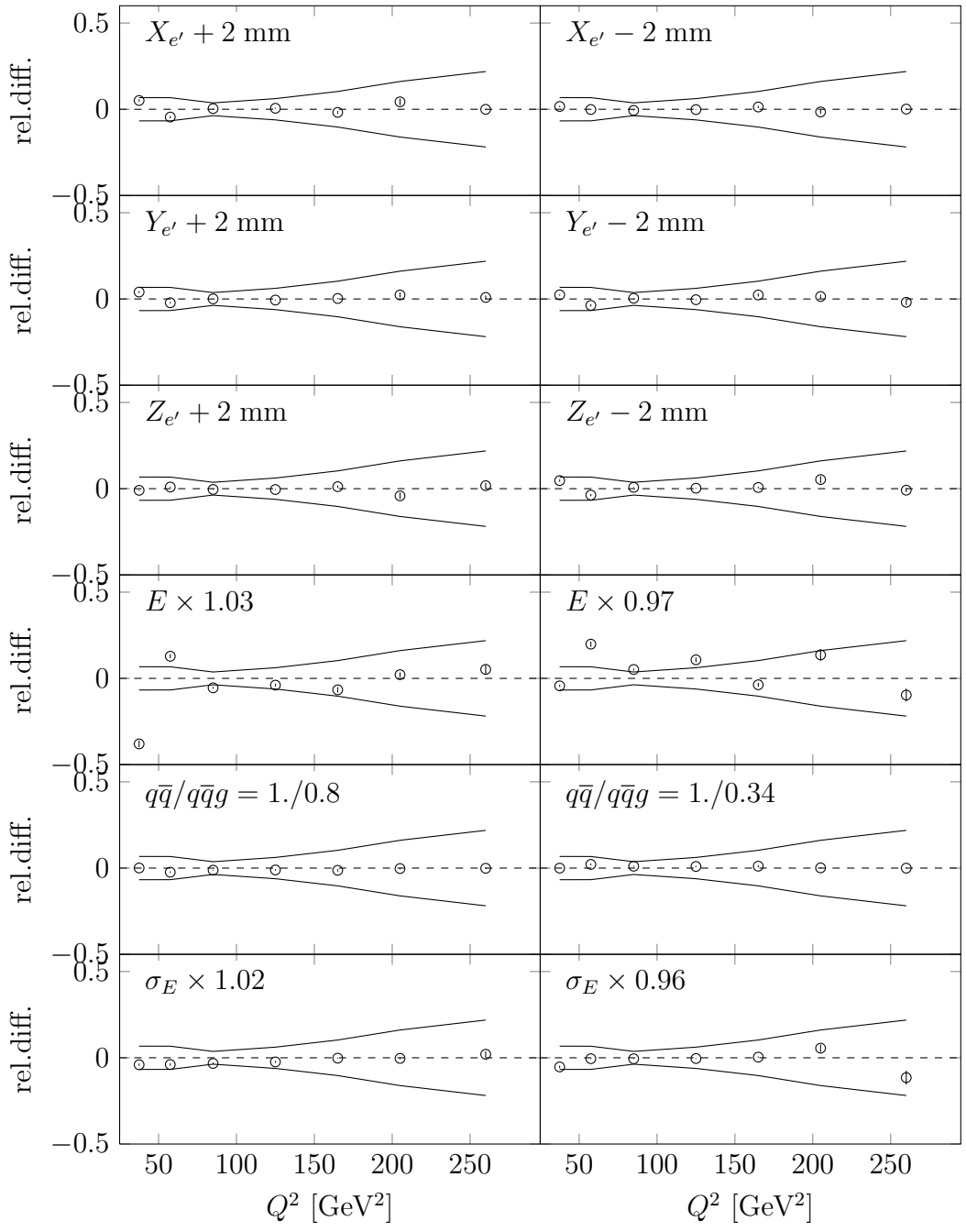

Figure 7.8: Systematic uncertainties of virtuality distribution originating from detector simulation and measurement technique. Markers show relative differences between number of events obtained with nominal and varied measurement. Vertical error bars show statistical uncertainty. In most cases uncertainties are smaller than points and error bars are not visible. Lines show statistical uncertainty of the nominal result.

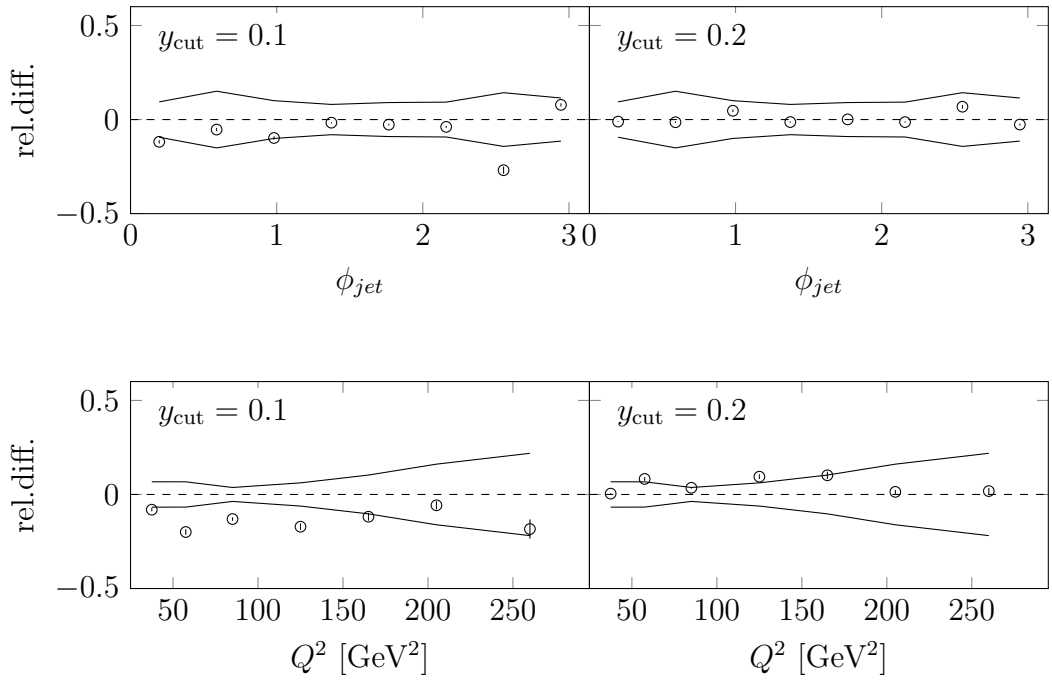

Figure 7.9: Systematic uncertainties originating form the jet resolution parameter. Markers show relative differences between number of events obtained with nominal and varied measurement. Vertical error bars show statistical uncertainty. In most cases uncertainties are smaller than points and error bars are not visible. Lines show statistical uncertainty of the nominal result.

7.3 Hadron Level Distributions

Hadron level distributions of jet azimuthal angle and virtuality are of the interest of this analysis, since these distributions are expected to reveal differences between the considered theoretical models. The unfolded distributions are compared in shape with boson-gluon fusion and 2-gluon exchange models.

Results are presented in fig. 7.10 on the next page. Statistical and full, i.e. systematic and statistical covariance matrices are shown in fig. 7.11 on the facing page.

Larger errors and bigger fluctuations of bins at the edges of the azimuthal angular distribution, i.e. close to 0 and π, are expected, since these are regions of large migrations in transverse momentum. Details are presented in sec. 5.7 on page 43.

Chi-squared test is used to check how well both considered models describe shapes of the distributions. Absolute normalisation of the theoretical predictions is fitted to the data with the least square method. The scaling factor is calculated according to the following formula

$$\alpha = \frac{\left(\mathrm{n}^{\mathrm{th}}\right)^{\intercal} \mathrm{V}^{-1} \mathrm{n}^{\mathrm{meas}}}{\left(\mathrm{n}^{\mathrm{th}}\right)^{\intercal} \mathrm{V}^{-1} \mathrm{n}^{\mathrm{th}}}\,, \tag{7.21}$$

where n^{th} and $\mathrm{n}^{\mathrm{meas}}$ are vectors of theoretical and measured distributions, V is a full (systematic and statistical) covariance matrix of the measured data. Value of the test statistics is calculated using full covariance matrix of the unfolded data

$$\chi^2 = \Delta^{\intercal} \mathrm{V} \Delta\,, \tag{7.22}$$

where V is full covariance matrix and Δ is vector of differences between unfolded and theoretical number of events in a given histogram bin.

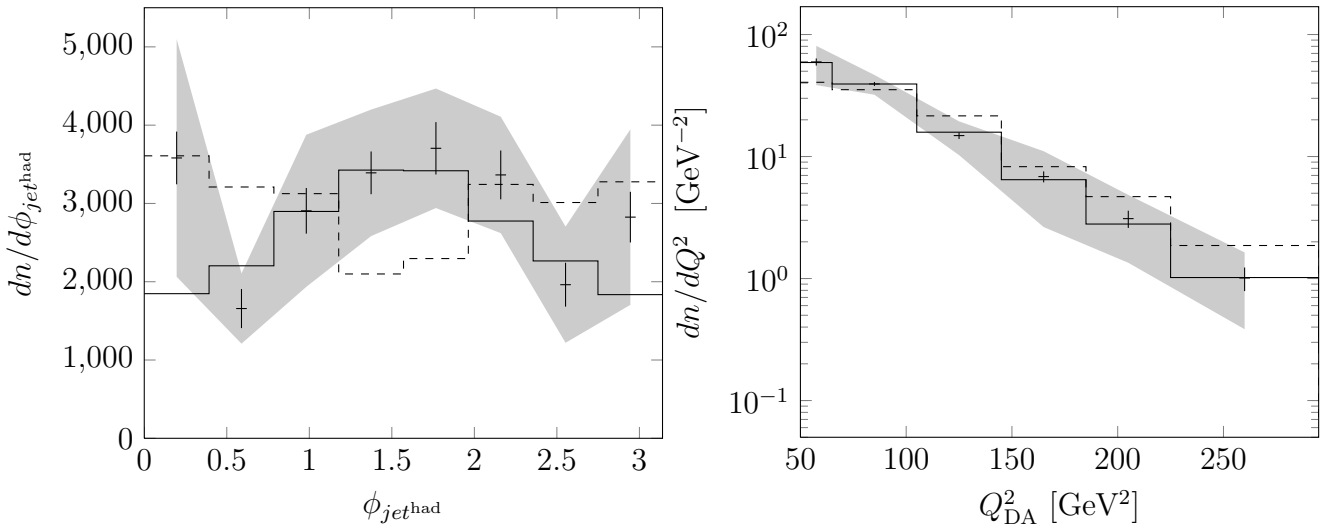

Figure 7.10: Hadron level distributions of jet azimuthal angle and virtuality. Error bars show square root of diagonal elements of statistical covariance matrix. Gray band shows square root of diagonal elements of systematic covariance matrix. Solid line histogram shows distribution shape predicted by 2-gluon exchange model. Dashed line histogram shows distribution shape predicted by boson-gluon fusion model.

$$\begin{pmatrix} 36245.3 \\ 17250.9 \\ 28437.4 \\ 27065.9 \\ 40641.7 \\ 32895.4 \\ 23567.7 \\ 29854.5 \end{pmatrix} \begin{pmatrix} 1 & -0.38 & 0.12 & -0.033 & 0.0026 & -0.0013 & -0.00087 & -0.00092 \\ -0.38 & 1 & -0.42 & 0.13 & -0.041 & 0.0099 & -0.0029 & 0.00024 \\ 0.12 & -0.42 & 1 & -0.4 & 0.12 & -0.035 & 0.0086 & -0.0025 \\ -0.033 & 0.13 & -0.4 & 1 & -0.4 & 0.094 & -0.024 & -0.0023 \\ 0.0026 & -0.041 & 0.12 & -0.4 & 1 & -0.41 & 0.13 & -0.041 \\ -0.0013 & 0.0099 & -0.035 & 0.094 & -0.41 & 1 & -0.44 & 0.13 \\ -0.00087 & -0.0029 & 0.0086 & -0.024 & 0.13 & -0.44 & 1 & -0.39 \\ -0.00092 & 0.00024 & -0.0025 & -0.0023 & -0.041 & 0.13 & -0.39 & 1 \end{pmatrix} \tag{7.17}$$

$$\begin{pmatrix} 355291 \\ 31042.8 \\ 145537 \\ 100660 \\ 89836.4 \\ 85243.5 \\ 84942.8 \\ 193651 \end{pmatrix} \begin{pmatrix} 1 & 0.31 & 0.65 & 0.71 & 0.78 & 0.28 & 0.45 & 0.75 \\ 0.31 & 1 & 0.76 & 0.77 & 0.59 & 0.69 & 0.61 & 0.73 \\ 0.65 & 0.76 & 1 & 0.75 & 0.79 & 0.78 & 0.8 & 0.82 \\ 0.71 & 0.77 & 0.75 & 1 & 0.69 & 0.56 & 0.59 & 0.79 \\ 0.78 & 0.59 & 0.79 & 0.69 & 1 & 0.42 & 0.67 & 0.69 \\ 0.28 & 0.69 & 0.78 & 0.56 & 0.42 & 1 & 0.68 & 0.63 \\ 0.45 & 0.61 & 0.8 & 0.59 & 0.67 & 0.68 & 1 & 0.53 \\ 0.75 & 0.73 & 0.82 & 0.79 & 0.69 & 0.63 & 0.53 & 1 \end{pmatrix} \tag{7.18}$$

Figure 7.11: Vectors of variance and correlation matrices of unfolded hadron level jet azimuthal angular distribution. Upper set is only statistical. Lower is total i.e. statistical and systematic.

$$\begin{pmatrix} 11020.3 \\ 6347.83 \\ 2421.19 \\ 1465.07 \\ 904.96 \\ 585.713 \end{pmatrix} \begin{pmatrix} 1 & -0.2 & 0.03 & -0.0088 & 0.0022 & -0.00066 \\ -0.2 & 1 & -0.2 & 0.038 & -0.0078 & 0.0026 \\ 0.03 & -0.2 & 1 & -0.28 & 0.057 & -0.02 \\ -0.0088 & 0.038 & -0.28 & 1 & -0.37 & 0.12 \\ 0.0022 & -0.0078 & 0.057 & -0.37 & 1 & -0.39 \\ -0.00066 & 0.0026 & -0.02 & 0.12 & -0.39 & 1 \end{pmatrix} \tag{7.19}$$

$$\begin{pmatrix} 100697 \\ 83988.9 \\ 33508.1 \\ 28309 \\ 4902.33 \\ 1918.77 \end{pmatrix} \begin{pmatrix} 1 & 0.38 & 0.19 & 0.096 & 0.14 & 0.12 \\ 0.38 & 1 & 0.77 & 0.72 & 0.64 & 0.61 \\ 0.19 & 0.77 & 1 & 0.94 & 0.95 & 0.87 \\ 0.096 & 0.72 & 0.94 & 1 & 0.92 & 0.94 \\ 0.14 & 0.64 & 0.95 & 0.92 & 1 & 0.88 \\ 0.12 & 0.61 & 0.87 & 0.94 & 0.88 & 1 \end{pmatrix} \tag{7.20}$$

Figure 7.12: Covariance matrices of unfolded hadron level virtuality distribution. Upper matrix is only statistical. Lower is total covariance, i.e. statistical and systematic.

The following values of χ^2 are obtained in comparison of the data with boson-gluon fusion model:

- jet azimuthal angular distribution — $\chi^2/\mathrm{NDF} = 43/7$ equals p-value = $0.2\ 10^{-6}$,
- virtuality distribution — $\chi^2/\mathrm{NDF} = 10/5$ equals p-value = 0.07.

Values of χ^2 corresponding to 2-gluon exchange model are as follows:

- jet azimuthal angular distribution — $\chi^2/\mathrm{NDF} = 7.5/7$ equals p-value = 0.37,
- virtuality distribution — $\chi^2/\mathrm{NDF} = 0.6/5$ equals p-value = 0.99.

Boson gluon fusion model does not describe the jet azimuthal angular distribution. Probability that the above statement is at the level of $0.2\ 10^{-6}$. It also fails to reproduce the data in photon virtuality distribution, however the probability that this conclusion is wrong is at the level of 7%. The resolving power of photon virtuality distribution is significantly reduced by large systematic errors of the smallest measured photon virtualities and starting the distribution of 50 GeV^2.

Based on jet azimuthal angular and photon virtuality distributions there are no reasons to reject the hypothesis that two-gluon exchange model describes the data. Probability that rejection of this model is incorrect equals 37% and 99% for jet azimuthal angular distribution and photon virtuality, respectively.

Additional studies with "pull method" have been performed. With every systematic check a nuisance parameter ξ_i is introduced. Then the minimum, with respect to the introduced parameters, of the following function is found

$$\chi^2 = \left(\Delta - \sum_i \xi_i \Delta_i\right)^{\mathsf{T}} \mathrm{V}^{stat} \left(\Delta - \sum_i \xi_i \Delta_i\right) + \sum_i \xi_i^2 \,, \tag{7.23}$$

where Δ is a vector of differences between the data and theoretical prediction, V^{stat} is a statistical covariance matrix and Δ_i is a vector of differences originating from a systematic check.

Every minimisation has been done twice to check if the result is stable with respect to the initial conditions. First minimisation is done with initial values of all parameters equal 0, while second with 1. The results of obtained from both procedures are exactly the same.

Parameters ξ_i obtained from comparison of the data with two-gluon exchange model are presented in fig. 7.13 on the following page for the jet azimuthal angular distribution and in fig. 7.14 on page 79 for the photon virtuality distribution.

In case of jet azimuthal angular distribution a value of $\chi^2 = 7$ is obtained. Absolute value of only one of the ξ_i parameters exceeds 1. The biggest contributions to the uncertainty comes from the shifts in virtual photon-proton centre of mass energy and inelasticity selection criteria. Significant are also shifts in diffractive selection criteria: maximal pseudorapidity of EFOs with energy greater than 0.4 GeV and fraction of incoming proton momentum carried by the pomeron.

In case of photon virtuality a value of $\chi^2 = 0.7$ is obtained. Absolute values of all the ξ_i parameters are smaller than 0.4. The biggest contribution comes from the shift in diffractive mass and inelasticity selection criteria.

Parameters ξ_i obtained from comparison of the data with boson gluon fusion model are presented in fig. 7.15 on page 80 for the jet azimuthal angular distribution and in fig. 7.16 on page 81 for the photon virtuality distribution.

In case of jet azimuthal angular distribution a value of $\chi^2 = 37$ is obtained. Absolute values of a few ξ_i parameters are larger than 1. The largest ξ_i corresponds to a change in calorimeter energy resolution and equals 2.33.

In case of photon virtuality a value of $\chi^2 = 10$ is obtained. Absolute values of two ξ_i parameters are larger than 1. The largest parameter corresponds to shift in inelasticity selection criteria and equals -1.78.

For comparison, result of the measurement of jet azimuthal angular distribution in small β region is presented in fig. 7.17 on page 82. In this region three parton events are expected to dominate, thus different shape of distributions is expected. The data confirm expectations. A mixture of events with $q\overline{q}$ and $q\overline{q}g$ generated using 2-gluon exchange model describes the data.

7.4 Hadron Level Cross Sections

Single differential cross section is calculated according to the following formula

$$\frac{d\sigma^{\mathrm{had}}}{dx} = \frac{N^{\mathrm{had}}}{\mathcal{L}\Delta x}\,, \tag{7.24}$$

where N is a number of events on hadron level, $\mathcal{L}$ is luminosity and Δx is size of the histogram bin. Cross sections in function of jet azimuthal angle and virtuality are shown in fig. 7.18 on page 82 and in tab. A.49 on page 116, tab. A.50 on page 116.

The single differential cross sections are calculated for completeness. The aim of this thesis is measurement of shapes of distributions. For the topological measurement suffices to draw conclusions.

Absolute cross sections are burdened with large correlated systematic errors.

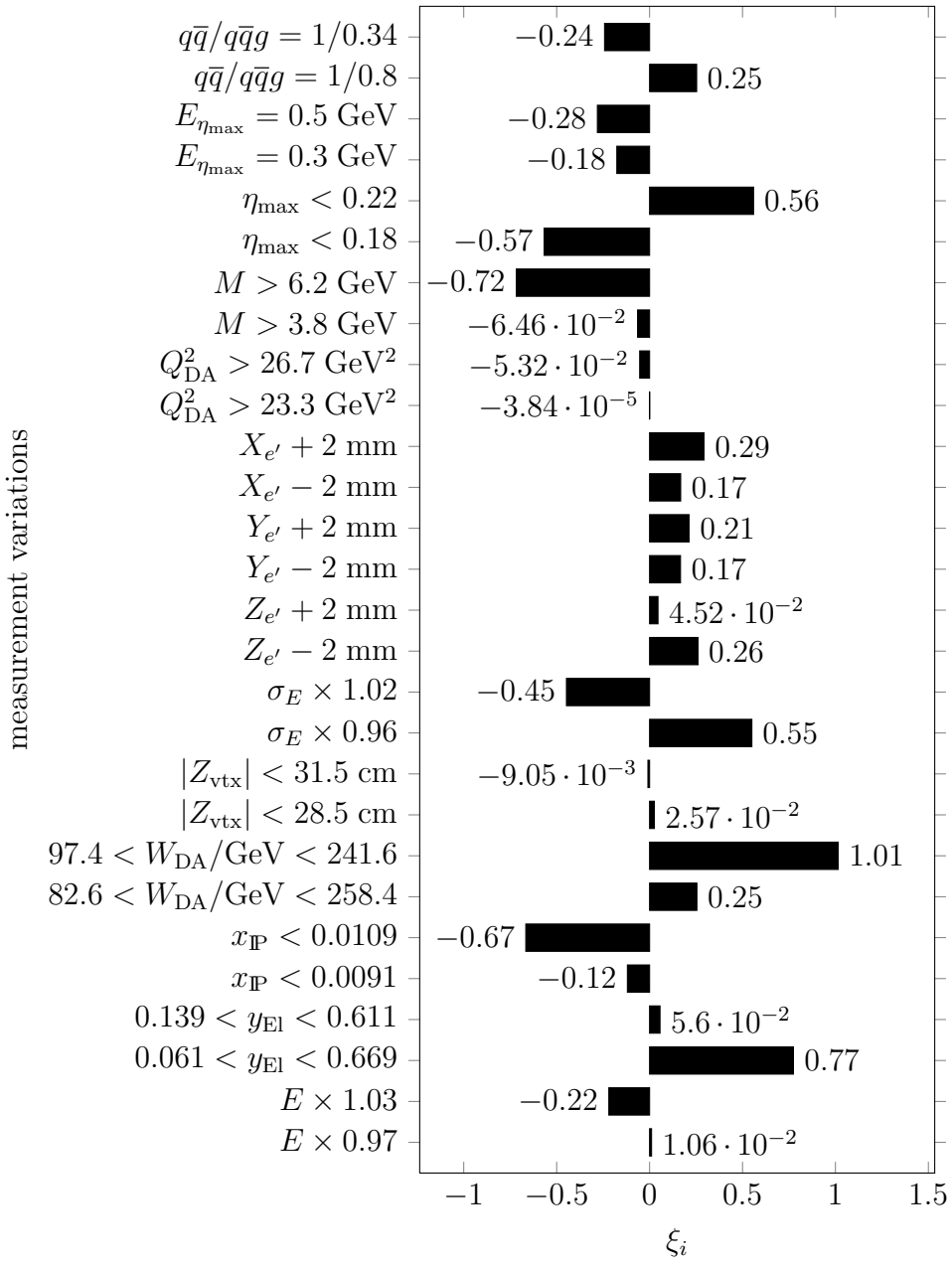

Figure 7.13: Diagram of ξ_i parameters for jet azimuthal angular distribution compared with two-gluon exchange model that minimise pull method χ^2.

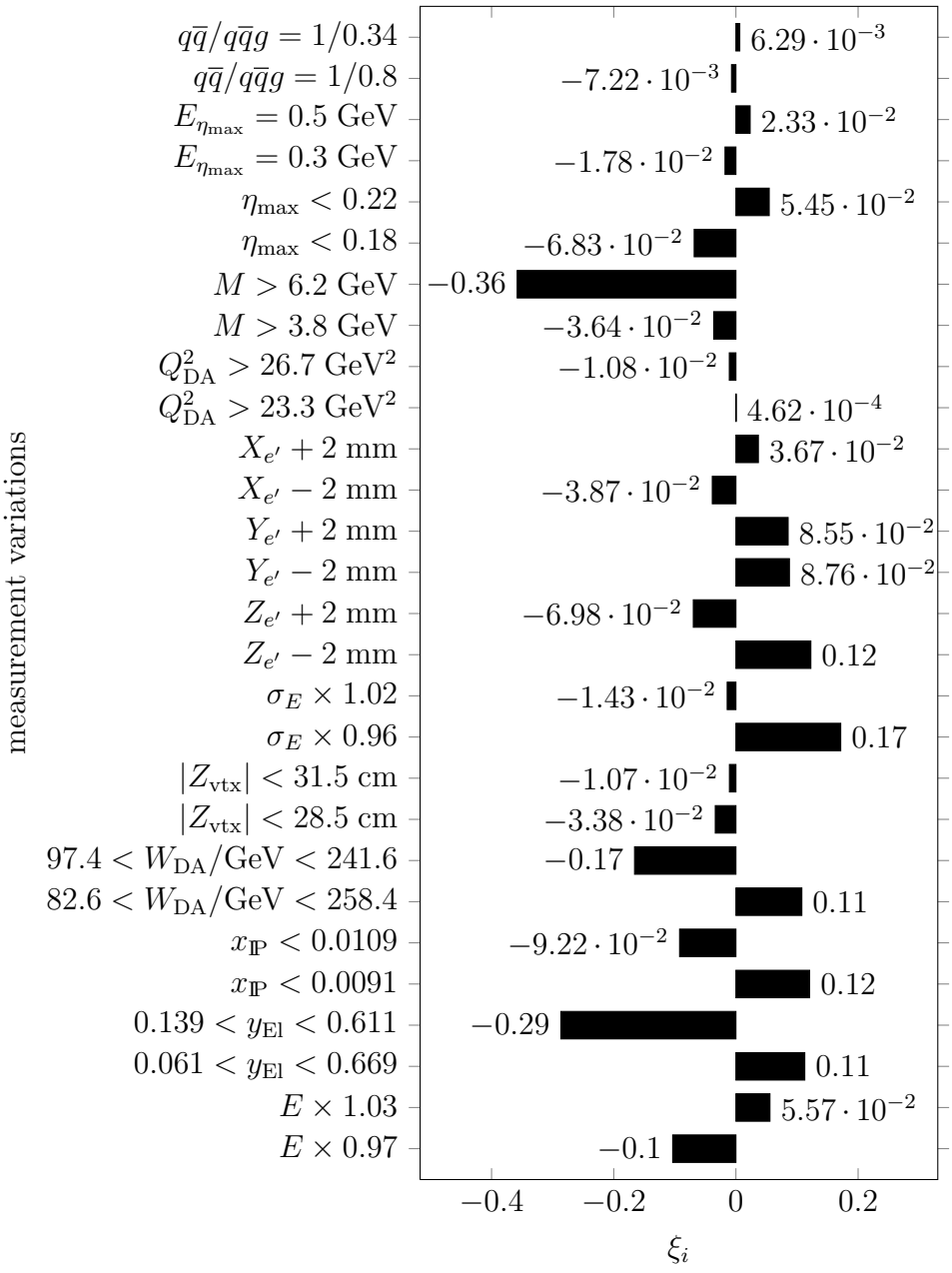

Figure 7.14: Diagram of ξ_i parameters for photon virtuality distribution compared with two-gluon exchange model that minimise pull method χ^2.

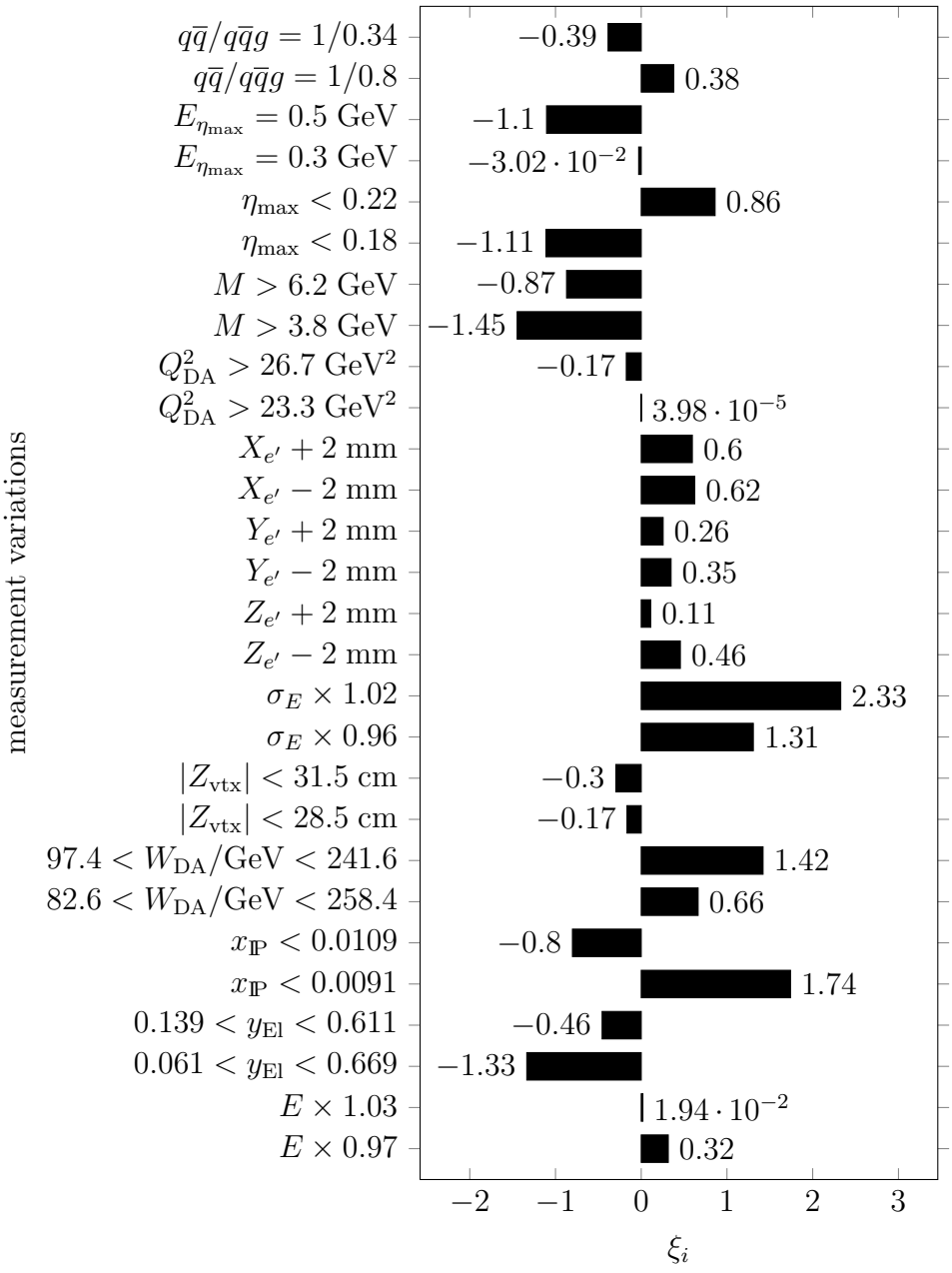

Figure 7.15: Diagram of ξ_i parameters for jet azimuthal angular distribution compared with boson gluon fusion exchange model that minimise pull method χ^2.

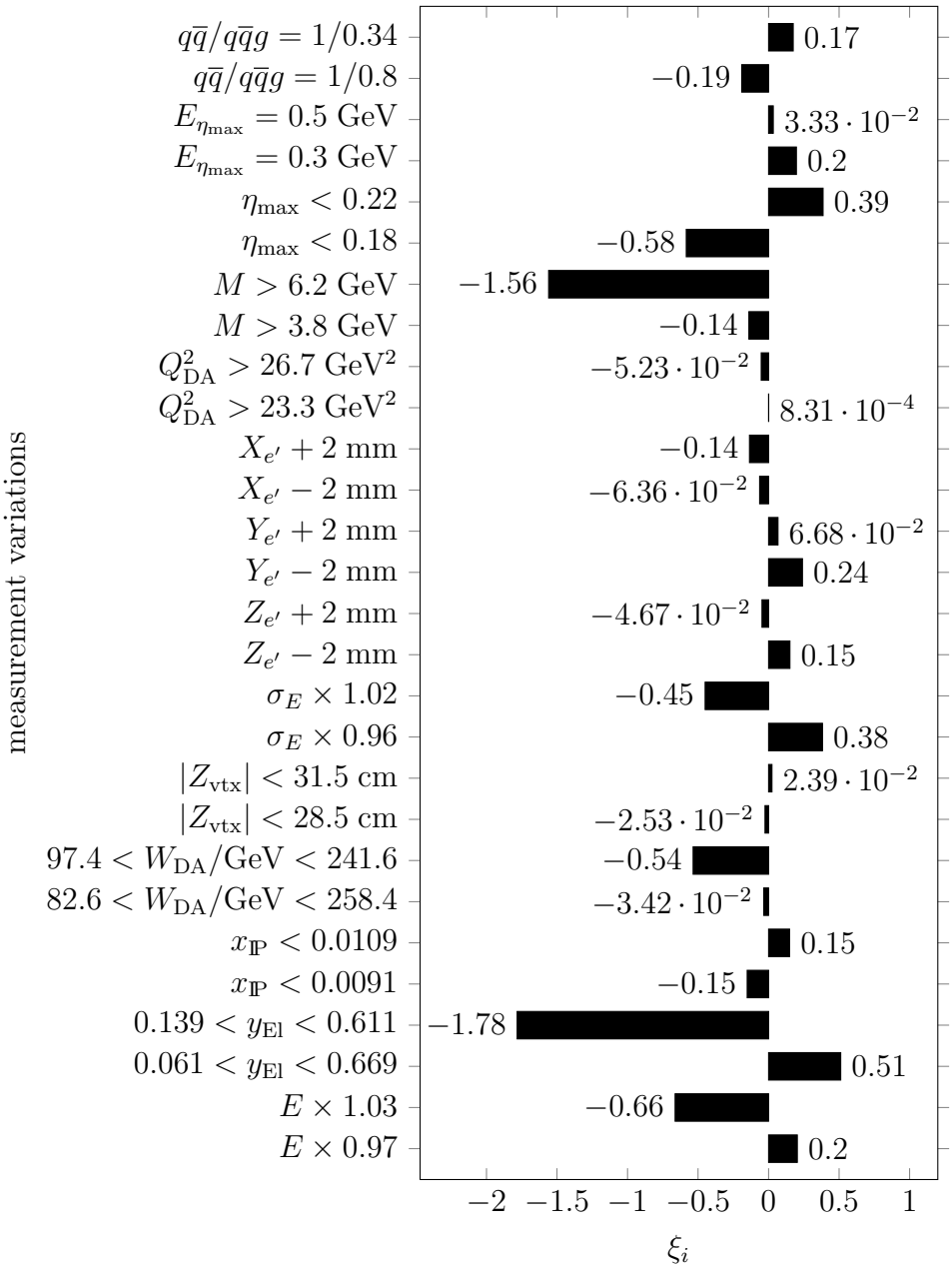

Figure 7.16: Diagram of ξ_i parameters for photon virtuality distribution compared with boson gluon fusion model that minimise pull method χ^2.

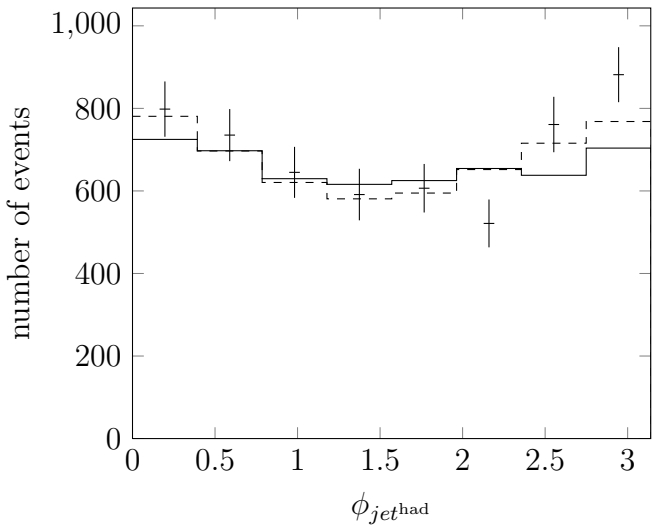

Figure 7.17: Hadron level distributions of jet azimuthal angle in region of $0.05 < \beta < 0.15$. Error bars represent only statistical uncertainty.

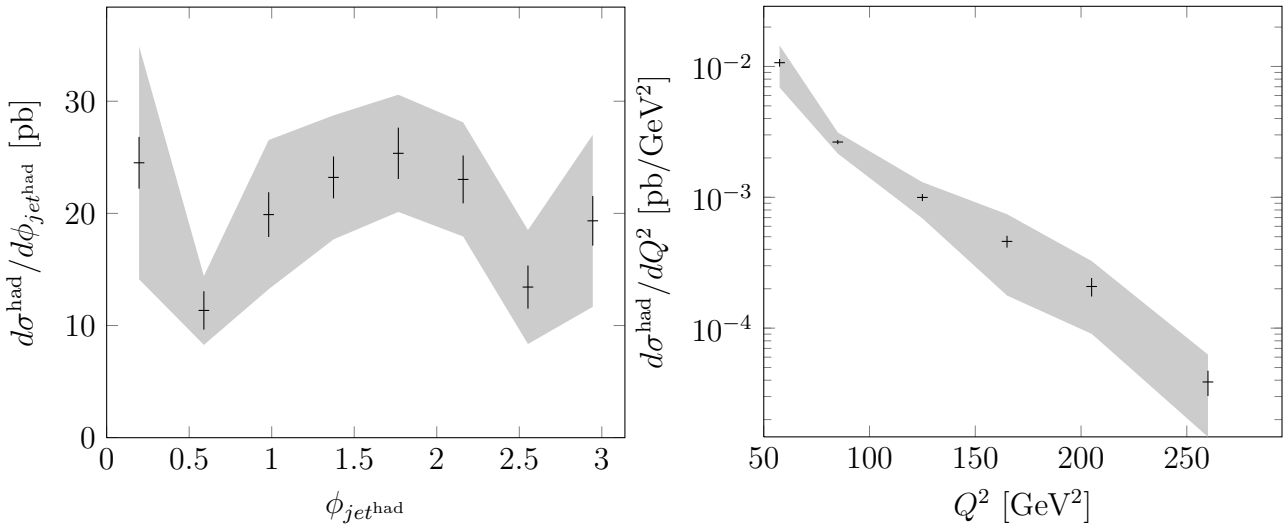

Figure 7.18: Hadron level single differential cross sections as a function of jet azimuthal angle and virtuality. Error bars show square root of diagonal elements of statistical covariance matrix. Gray band shows square root of diagonal elements of systematic covariance matrix.

Chapter 8

Summary and Conclusions

Mechanism of diffractive dijet production in deep inelastic scattering has been investigated in this thesis. Two most popular models has been presented and put to test.

Boson-gluon fusion model assumes that pomeron is a compound object. Pomeron interaction is parametrised with diffractive parton density functions. The functions are determined experimentally. A parton emerging from the pomeron interacts according to QED or QCD. As far as diffractive dijet production in lepton proton interaction is concerned, a gluon originating from the pomeron interacts with virtual photon, producing a pair of quarks. The quarks are preferably produced in the plane spanned by the incoming and scattered lepton.

This phenomenological approach can be used in hard as well as soft interactions, where perturbative calculations are not applicable. It is sometimes referred to as exchange of "soft pomeron". The model is a default one in commonly used Monte Carlo generator RAPGAP.

The other model that has been investigated in the thesis is two-gluon exchange model. Diffractive interaction is mediated by a pair of gluons that form a colour singlet. The gluons interact with colour dipole, which is produced by virtual photon fluctuation. A pair of quarks emerging from this process is preferably produced in a plane perpendicular to the lepton plane.

This model is based solely on perturbative QCD and is valid only in regions where hard scale is present. Thus it is referred to as exchange of "hard pomeron".

Predictions of models mentioned above have been compared with data gathered by the ZEUS detector in years 2003-2007. Integrated data luminosity amounts to almost 350 pb^{-1}. The measurement has been performed in kinematic region of high parton transverse momentum and low masses (high β). The first provides hard scale that justifies the use of perturbative calculations. The latter selects two parton systems.

Shapes of distributions of jet azimuthal angle and photon virtuality have been studied. These distributions reveal differences between the two models. It has been shown that the boson-gluon fusion model does not describe the data in the studied kinematic region. There is a clear discrepancy between the data and the model.

The measured distributions can be explained using two-gluon exchange model. Precision measurement of model parameters, that would allow for further verification, may be very difficult due to the quality and luminosity of the data.

Data measured in the kinematic region of high masses are equally well described by both models. Due to the shortcomings mentioned in the previous paragraph it is impossible to conclude if data favour two-gluon exchange model or a mixture of hard and soft pomeron exchange.

Summarising, the signal with characteristics expected from the exclusive diffractive dijet production via two-gluon exchange has been measured for the first time with data gathered during HERA II operation. It has been proven that the boson-gluon fusion model alone is not capable of explaining the data in high β region. The results are in agreement with analogous

analysis done with data gathered during the first period of HERA accelerator operation [37].

Acknowledgements

At the very beginning, I would like to express my gratitude to my supervisors: prof. Danuta Kisielewska and dr Leszek Adamczyk, for their attention, care and guidance throughout my whole Ph.D. studies.

I would also like to thank all the people I had pleasure to meet and work with at DESY. Achim Geiser and Olaf Behnke for giving me the opportunity to work at such extraordinary place and for their advises. Ewald Paul for consultation and support. Whole "polish group" in ZEUS for their warm welcome and help.

I would also like to convey my honours to two outstanding mathematicians, musicians and physicists: Adam Bzowski and Marcin Guzik for countless stimulating discussions.

Bibliography

[1] J. Bartels, J. R. Ellis, H. Kowalski, and M. Wusthoff, "An Analysis of diffraction in deep inelastic scattering," *Eur.Phys.J.* **C7** (1999) 443–458, arXiv:hep-ph/9803497 [hep-ph].

[2] H. Lotter, "Phenomenology of the BFKL pomeron and unitarity corrections at low x," arXiv:hep-ph/9705288 [hep-ph].

[3] U. Klein, "Zeus luminosity web page." http://zeusdp.desy.de/physics/lumi/lumi03/periods.html.

[4] W. H. Smith *et al.*, "The ZEUS calorimeter first level trigger," *Nucl. Instrum. Meth.* **A355** (1995) 278–294.

[5] L. de Broglie, "Radiations. - ondes et quanta (radiation - waves and quanta)," *Comptes rendus* **177** (1923) 507–510.

[6] L. de Broglie, *Recherches sur la théorie des quanta (Research on the Theory of the Quanta)*. PhD thesis, University of Paris, 1924. english translation of the first chapter: "Phase Waves of Louis deBroglie", Am. J. Phys. vol. 40 no. 9, pp. 1315-1320, September, 1972.

[7] C. Davisson and L. H. Germer, "The scattering of electrons by a single crystal of nickel," *Nature* **119** (1927) no. 2998, 558–560. http://www.nature.com/physics/looking-back/davisson/index.html.

[8] G. P. Thomson and A. Reid, "Diffraction of cathode rays by a thin film," *Nature* **119** (1927) no. 3007, 890.

[9] E. Feinberg and I. Pomerancuk, "High energy inelastic diffraction phenomena," *Il Nuovo Cimento Series 10* **3** (1956) 652–671. http://dx.doi.org/10.1007/BF02746068.

[10] R. Glauber, "Deuteron Stripping Processes at High Energies," *Phys.Rev.* **99** (1955) 1515–1516.

[11] M. Good and W. Walker, "Diffraction disssociation of beam particles," *Phys.Rev.* **120** (1960) 1857–1860.

[12] Y. L. Dokshitzer, V. A. Khoze, A. H. Mueller, and S. Troian, "Basics of perturbative QCD,".

[13] T. Regge, "Bound states, shadow states and Mandelstam representation," *Nuovo Cim.* **18** (1960) 947–956.

[14] T. Regge, "Introduction to complex orbital momenta," *Nuovo Cim.* **14** (1959) 951.

[15] P. Collins, "An Introduction to Regge Theory and High-Energy Physics,".

[16] V. Gribov, "POSSIBLE ASYMPTOTIC BEHAVIOR OF ELASTIC SCATTERING," *JETP Lett.* **41** (1961) 667–669.

[17] A. Donnachie and P. Landshoff, "Total cross-sections," *Phys.Lett.* **B296** (1992) 227–232, arXiv:hep-ph/9209205 [hep-ph].

[18] A. Donnachie and P. Landshoff, "p p and anti-p p Elastic Scattering," *Nucl.Phys.* **B231** (1984) 189.

[19] **UA8 Collaboration** Collaboration, R. Bonino *et al.*, "Evidence for Transverse Jets in High Mass Diffraction," *Phys.Lett.* **B211** (1988) 239.

[20] G. Ingelman and P. Schlein, "Jet Structure in High Mass Diffractive Scattering," *Phys.Lett.* **B152** (1985) 256.

[21] S. J. Brodsky, L. Frankfurt, J. Gunion, A. H. Mueller, and M. Strikman, "Diffractive leptoproduction of vector mesons in QCD," *Phys.Rev.* **D50** (1994) 3134–3144, arXiv:hep-ph/9402283 [hep-ph].

[22] J. Bartels, H. Lotter, and M. Wusthoff, "Quark - anti-quark production in DIS diffractive dissociation," *Phys.Lett.* **B379** (1996) 239–248, arXiv:hep-ph/9602363 [hep-ph].

[23] E. Levin, A. D. Martin, M. Ryskin, and T. Teubner, "Diffractive open charm production at HERA," *Z.Phys.* **C74** (1997) 671–685, arXiv:hep-ph/9606443 [hep-ph].

[24] J. R. Forshaw and M. Ryskin, "Diffractive vector meson production at large momentum transfer," *Z.Phys.* **C68** (1995) 137–148, arXiv:hep-ph/9501376 [hep-ph].

[25] J. Bjorken, "Final state hadrons in deep inelastic processes and colliding beams," *Conf.Proc.* **C710823** (1971) 281–297.

[26] **ZEUS Collaboration** Collaboration, S. Chekanov *et al.*, "Dijet production in neutral current deep inelastic scattering at HERA," *Eur.Phys.J.* **C23** (2002) 13–27, arXiv:hep-ex/0109029 [hep-ex].

[27] J. Bartels, C. Ewerz, H. Lotter, and M. Wusthoff, "Azimuthal distribution of quark - anti-quark jets in DIS diffractive dissociation," *Phys.Lett.* **B386** (1996) 389–396, arXiv:hep-ph/9605356 [hep-ph].

[28] H. Jung, *The Rapgap Monte Carlo for Deep Inelastic Scattering*, 3.1 ed. http://rapgap.hepforge.org/.

[29] G. Ingelman, A. Edin, R. Enberg, J. Rathsman, and N. Timneanu, "Soft color interactions in nonperturbative QCD," *Nucl.Phys.* **A663** (2000) 1007–1010, arXiv:hep-ph/9912537 [hep-ph].

[30] **H1 Collaboration** Collaboration, C. Adloff *et al.*, "Inclusive measurement of diffractive deep inelastic ep scattering," *Z.Phys.* **C76** (1997) 613–629, arXiv:hep-ex/9708016 [hep-ex].

[31] A. Edin, G. Ingelman, and J. Rathsman, "Soft color interactions as the origin of rapidity gaps in DIS," *Phys.Lett.* **B366** (1996) 371–378, arXiv:hep-ph/9508386 [hep-ph].

[32] S. Catani and F. Hautmann, "High-energy factorization and small x deep inelastic scattering beyond leading order," *Nucl.Phys.* **B427** (1994) 475–524, arXiv:hep-ph/9405388 [hep-ph].

[33] V. Braun and D. Y. Ivanov, "Exclusive diffractive electroproduction of dijets in collinear factorization," *Phys.Rev.* **D72** (2005) 034016, arXiv:hep-ph/0505263 [hep-ph].

[34] J. Bartels, H. Jung, and M. Wusthoff, "Quark - anti-quark gluon jets in DIS diffractive dissociation," *Eur.Phys.J.* **C11** (1999) 111–125, arXiv:hep-ph/9903265 [hep-ph].

[35] K. J. Golec-Biernat and M. Wusthoff, "Saturation in diffractive deep inelastic scattering," *Phys.Rev.* **D60** (1999) 114023, arXiv:hep-ph/9903358 [hep-ph].

[36] K. J. Golec-Biernat and M. Wusthoff, "Saturation effects in deep inelastic scattering at low Q**2 and its implications on diffraction," *Phys.Rev.* **D59** (1998) 014017, arXiv:hep-ph/9807513 [hep-ph].

[37] J. Szuba, *Measurement of the photon light cone wave function by diffractive dissociation in the ZEUS experiment at HERA*. PhD thesis, AGH University, Cracow, 2005.

[38] DESY, "Pointing the way, how hera is helping to shape the future of physics." DESY Brochure.

[39] K. Kleinknecht, *Detectors for Particle Radiation*. Cambridge University Press, second ed., 1998.

[40] ZEUS Collaboriation, "Zeus status report." http://www-zeus.desy.de/bluebook/bluebook.html, Luty, 1993.

[41] **ZEUS MVD Group** Collaboration, V. Chiochia, "The ZEUS Micro Vertex Detector," *Nucl.Instrum.Meth.* **A501** (2003) 60–64, arXiv:hep-ex/0111061 [hep-ex].

[42] W. H. Smith, K. Tokushuku, and L. W. Wiggers, "The ZEUS trigger system,". Contributed to 10th International Conference on Computing in High Energy Physics (CHEP 92), Annecy, France, 21-25 Sept 1992, http://ccdb4fs.kek.jp/cgi-bin/img_index?199303065.

[43] G. P. Heath *et al.*, "The ZEUS first level tracking trigger," *Nucl. Instrum. Meth.* **A315** (1992) 431–435.

[44] P. D. Allfrey *et al.*, "The design and performance of the ZEUS global tracking trigger," *Nucl. Instrum. Meth.* **A580** (2007) 1257–1282.

[45] H. J. van der Lugt, *The Data acquisition and second level trigger system for the ZEUS calorimeter*. PhD thesis, University of Amsterdam, april, 1993.

[46] H. A. J. R. Uijterwaal, *The Global second level trigger for ZEUS*. PhD thesis, University of Amsterdam, 1992.

[47] U. Behrens, L. Hagge, and W. O. Vogel, "The Eventbuilder of the ZEUS experiment," *Nucl. Instrum. Meth.* **A332** (1993) 253–262.

[48] H. Kowalski, T. Poser, L. Stanco, and E. Tscheslog, "Investigation of ADAMO performance in the ZEUS calorimeter reconstruction program," *Comput. Phys. Commun.* **57** (1989) 222–224.

[49] J. C. Hart, "Experience with ADAMO in ZEUS,". In *Erice 1990, Proceedings, Data structures for particle physics experiments* 51-57.

[50] D. Bandyopadhyay *et al.*, "Architecture of the ZEUS third level trigger system,". Contributed to 8th Real-Time Computer Applications in Nuclear, Particle and Plasma Physics (RT93), Vancouver, Canada, 8-11 Jun 1993, http://ccdb4fs.kek.jp/cgi-bin/img_index?9308227.

[51] **ZEUS TLT Group** Collaboration, D. Bandhopadhyay *et al.*, "Online selection of physics events in the ZEUS third level trigger,". Contributed to 8th Real-Time Computer Applications in Nuclear, Particle and Plasma Physics (RT93), Vancouver, Canada, 8-11 Jun 1993, http://ccdb4fs.kek.jp/cgi-bin/img_index?9308227.

[52] K. Charchuła, G. Schuler, and H. Spiesberger, "Combined qed and qcd radiative effects in deep inelastic lepton-proton scattering: the monte carlo generator django6," *Computer Physics Communications* **81** (1994) no. 3, 381 – 402. http://www.sciencedirect.com/science/article/pii/0010465594900868.

[53] L. Lönnblad, "Ariadne version 4 — a program for simulation of qdc cascades implementing the colour dipole model," *Computer Physics Communications* **71** (1992) no. 1–2, 15 – 31. http://www.sciencedirect.com/science/article/pii/001046559290068A.

[54] A. Kwiatkowski, H. Spiesberger, and H.-J. Möhring, "Heracles: an event generator for ep interactions at hera energies including radiative processes," *Computer Physics Communications* **69** (1992) no. 1, 155 – 172. http://www.sciencedirect.com/science/article/pii/001046559290136M.

[55] S. Kawabata, "A New version of the multidimensional integration and event generation package BASES/SPRING," *Comp. Phys. Commun.* **88** (1995) 309–326.

[56] **CTEQ Collaboration** Collaboration, H. Lai *et al.*, "Global QCD analysis of parton structure of the nucleon: CTEQ5 parton distributions," *Eur.Phys.J.* **C12** (2000) 375–392, arXiv:hep-ph/9903282 [hep-ph].

[57] T. Sjostrand, "PYTHIA 5.7 and JETSET 7.4: Physics and manual," arXiv:hep-ph/9508391 [hep-ph].

[58] B. Andersson, G. Gustafson, G. Ingelman, and T. Sjostrand, "Parton Fragmentation and String Dynamics," *Phys.Rept.* **97** (1983) 31–145.

[59] T. Sjostrand, L. Lonnblad, and S. Mrenna, "PYTHIA 6.2: Physics and manual," arXiv:hep-ph/0108264 [hep-ph].

[60] B. Andersson, G. Gustafson, L. Lönnblad, and U. Pettersson, "Coherence effects in deep inelastic scattering," *Zeitschrift für Physik C Particles and Fields* **43** (1989) no. 4, 625–632. http://dx.doi.org/10.1007/BF01550942.

[61] G. Gustafson and U. Pettersson, "Dipole formulation of qcd cascades," *Nuclear Physics B* **306** (1988) no. 4, 746 – 758. http://www.sciencedirect.com/science/article/pii/0550321388904415.

[62] G. Gustafson, "Dual description of a confined colour field," *Physics Letters B* **175** (1986) no. 4, 453 – 456. http://www.sciencedirect.com/science/article/pii/0370269386906222.

[63] R. Brun, F. Bruyant, M. Maire, A. C. McPherson, and P. Zanarini, "GEANT3,". CERN-DD/EE/84-1.

[64] E. de Wolf, "Zgana, zeus trigger simulation library,".

[65] G. M. Briskin, *Diffractive dissociation in e p deep inelastic scattering.* PhD thesis, Tel Aviv University, 1998. `http://www-library.desy.de/preparch/desy/thesis/desy-thesis-98-036.pdf`.

[66] N. Tuning, *Proton structure functions at HERA.* PhD thesis, University of Amsterdam, 2001. `http://www.nikhef.nl/pub/services/biblio/theses/N_Tuning.html`.

[67] N. Tuning, "Zufos: Hadronic final state reconstruction with calorimeter, tracking and backsplash correction." ZEUS internal note, `http://inspirehep.net/record/940978/`.

[68] A. Geiser, "Gmuon - a general zeus muon finder." ZEUS internal note, `http://inspirehep.net/record/940866`.

[69] H. Abramowicz, A. Caldwell, and R. Sinkus, "Neural network based electron identification in the ZEUS calorimeter," *Nucl.Instrum.Meth.* **A365** (1995) 508–517, `arXiv:hep-ex/9505004 [hep-ex]`.

[70] H. A. R. Sinkus, "Electron Identification with Neural Networks at ZEUS,".

[71] A. Blondel and F. Jacquet in *Proceedings of the study of an ep facility for Europe*, U. Amaldi, ed., pp. 391–394. 1979.

[72] S. Bentvelsen, J. Engelen, and P. Kooijman, "Reconstruction of (x, Q**2) and extraction of structure functions in neutral current scattering at HERA,".

[73] M. Cacciari, G. P. Salam, and G. Soyez, "FastJet User Manual," *Eur.Phys.J.* **C72** (2012) 1896, `arXiv:1111.6097 [hep-ph]`.

[74] S. Catani, Y. L. Dokshitzer, M. Olsson, G. Turnock, and B. Webber, "New clustering algorithm for multi - jet cross-sections in e+ e- annihilation," *Phys.Lett.* **B269** (1991) 432–438.

[75] J. Frenkel and J. Taylor, "Exponentiation of Leading Infrared Divergences in Massless Yang-Mills Theories," *Nucl.Phys.* **B116** (1976) 185.

[76] Y. L. Dokshitzer, D. Diakonov, and S. Troian, "Hard Processes in Quantum Chromodynamics," *Phys.Rept.* **58** (1980) 269–395.

[77] M. Krasny, "Hard QED radiation at HERA," *J.Phys.* **G19** (1993) 1479–1488.

[78] **ZEUS** Collaboration, "Zeus primer." `http://zeusdp.desy.de/ZEUS_ONLY/analysis/primer/`.

[79] **ZEUS** Collaboration, "Zeus global first level trigger (gflt)." `http://www-zeus.desy.de/components/gflt/`.

[80] A. Bonato, *Diffractive dijet production in deep inelastic scattering at ZEUS.* PhD thesis, Hamburg Univeristy, 2008.

[81] **ZEUS** Collaboration, S. Chekanov *et al.*, "Diffractive photoproduction of dijets in ep collisions at HERA," *Eur.Phys.J.* **C55** (2008) 177–191, `arXiv:0710.1498 [hep-ex]`.

[82] **ZEUS** Collaboration, S. Chekanov *et al.*, "Measurement of the open charm contribution to the diffractive proton structure function," *Nucl.Phys.* **B672** (2003) 3–35, arXiv:hep-ex/0307068 [hep-ex].

[83] **ZEUS Collaboration** Collaboration, J. Breitweg *et al.*, "Elastic and proton dissociative ρ^0 photoproduction at HERA," *Eur.Phys.J.* **C2** (1998) 247–267, arXiv:hep-ex/9712020 [hep-ex].

[84] **H1 Collaboration** Collaboration, C. Adloff *et al.*, "Proton dissociative ρ and elastic ϕ electroproduction at HERA," *Z.Phys.* **C75** (1997) 607–618, arXiv:hep-ex/9705014 [hep-ex].

[85] S. Schmitt, "TUnfold: an algorithm for correcting migration effects in high energy physics," *JINST* **7** (2012) T10003, arXiv:1205.6201 [physics.data-an].

[86] R. Brun and F. Rademakers, "ROOT: An object oriented data analysis framework," *Nucl.Instrum.Meth.* **A389** (1997) 81–86. See also http://root.cern.ch/.

[87] A. N. Tikhonov and V. Y. Arsenin, *Solutions of ill-posed problems*. V. H. Winston & Sons, Washington, D.C.: John Wiley & Sons, New York, 1977. Translated from the Russian, Preface by translation editor Fritz John, Scripta Series in Mathematics.

[88] A. N. Tikhonov, "On the solution of ill-posed problems and the method of regularization," *Dokl. Akad. Nauk SSSR* **151** (1963) 501–504.

[89] P. C. Hansen, "The l-curve and its use in the numerical treatment of inverse problems," in *in Computational Inverse Problems in Electrocardiology, ed. P. Johnston, Advances in Computational Bioengineering*, pp. 119–142. WIT Press, 2000.

[90] **ZEUS Collaboration** Collaboration, M. Derrick *et al.*, "Measurement of the F2 structure function in deep inelastic e+ p scattering using 1994 data from the ZEUS detector at HERA," *Z.Phys.* **C72** (1996) 399–424, arXiv:hep-ex/9607002 [hep-ex].

[91] **ZEUS Collaboration** Collaboration, H. Abramowicz *et al.*, "Inclusive dijet cross sections in neutral current deep inelastic scattering at HERA," *Eur.Phys.J.* **C70** (2010) 965–982, arXiv:1010.6167 [hep-ex].

[92] **ZEUS Collaboration** Collaboration, S. Chekanov *et al.*, "Diffractive photoproduction of D*+-(2010) at HERA," *Eur.Phys.J.* **C51** (2007) 301–315, arXiv:hep-ex/0703046 [hep-ex].

[93] R. Renner, *Dijets in diffractive photoproduction measured with the ZEUS experiment*. PhD thesis, Bonn University, 2006.

[94] J. Behr, *Jets at high Q^2 at HERA and test beam measurements with the EUDET pixel telescope*. PhD thesis, University of Hamburg, 2010.

Appendices

Appendix A

Tables

A.1 Reconstruction

Table A.1: Relative resolution of inelasticity reconstructed with three different methods: electron (El), Jacquet-Blondel (JB) and double-angle (DA).

	number of events		
$\Delta y/y$	El	JB	DA
$(-\infty\ ;\ -0.6]$	0	5	1
$(-0.6\ ;\ -0.525]$	1	9	2
$(-0.525\ ;\ -0.45]$	10	31	1
$(-0.45\ ;\ -0.375]$	21	65	7
$(-0.375\ ;\ -0.3]$	85	155	26
$(-0.3\ ;\ -0.225]$	167	302	88
$(-0.225\ ;\ -0.15]$	449	634	289
$(-0.15\ ;\ -0.075]$	998	1,110	1,031
$(-0.075\ ;\ 0]$	2,081	1,472	2,625
$(0\ ;\ 0.075]$	2,043	1,573	2,434
$(0.075\ ;\ 0.15]$	1,111	1,380	1,063
$(0.15\ ;\ 0.225]$	589	927	547
$(0.225\ ;\ 0.3]$	358	586	384
$(0.3\ ;\ 0.375]$	237	383	218
$(0.375\ ;\ 0.45]$	170	258	192
$(0.45\ ;\ 0.525]$	132	198	129
$(0.525\ ;\ 0.6]$	121	146	80
$(0.6\ ;\ \infty]$	1,159	498	615

Table A.2: Relative resolution of Bjorken scaling variable reconstructed with three different methods: electron (El), Jacquet-Blondel (JB) and double-angle (DA).

	number of events		
$\Delta x/x$	El	JB	DA
$(-\infty\ ;\ -0.6]$	373	163	5
$(-0.6\ ;\ -0.525]$	151	179	19
$(-0.525\ ;\ -0.45]$	201	288	72
$(-0.45\ ;\ -0.375]$	269	405	153
$(-0.375\ ;\ -0.3]$	391	509	289
$(-0.3\ ;\ -0.225]$	618	642	440
$(-0.225\ ;\ -0.15]$	906	754	662
$(-0.15\ ;\ -0.075]$	1,321	866	1,215
$(-0.075\ ;\ 0]$	1,540	938	1,866
$(0\ ;\ 0.075]$	1,405	899	1,890
$(0.075\ ;\ 0.15]$	999	863	1,300
$(0.15\ ;\ 0.225]$	642	701	682
$(0.225\ ;\ 0.3]$	353	547	410
$(0.3\ ;\ 0.375]$	247	408	221
$(0.375\ ;\ 0.45]$	108	343	176
$(0.45\ ;\ 0.525]$	73	251	86
$(0.525\ ;\ 0.6]$	39	212	60
$(0.6\ ;\ \infty]$	96	764	186

Table A.3: Relative resolution of virtuality reconstructed with three different methods: electron (El), Jacquet-Blondel (JB) and double-angle (DA).

	number of events		
$\Delta Q^2/Q^2$	El	JB	DA
$(-\infty\ ;\ -0.6]$	2	205	2
$(-0.6\ ;\ -0.525]$	1	206	0
$(-0.525\ ;\ -0.45]$	0	272	1
$(-0.45\ ;\ -0.375]$	0	408	0
$(-0.375\ ;\ -0.3]$	7	458	4
$(-0.3\ ;\ -0.225]$	25	543	21
$(-0.225\ ;\ -0.15]$	80	683	91
$(-0.15\ ;\ -0.075]$	684	757	504
$(-0.075\ ;\ 0]$	3,239	746	3,259
$(0\ ;\ 0.075]$	3,533	720	3,513
$(0.075\ ;\ 0.15]$	940	698	762
$(0.15\ ;\ 0.225]$	361	599	269
$(0.225\ ;\ 0.3]$	198	546	188
$(0.3\ ;\ 0.375]$	160	438	159
$(0.375\ ;\ 0.45]$	100	359	108
$(0.45\ ;\ 0.525]$	108	317	79
$(0.525\ ;\ 0.6]$	73	262	97
$(0.6\ ;\ \infty]$	221	1,515	675

Table A.4: Relative resolution of boson-proton centre of mass energy reconstructed with three different methods: electron (El), Jacquet-Blondel (JB) and double-angle (DA).

	number of events		
$\Delta W/W$	El	JB	DA
$(-\infty\ ;\ -0.6]$	0	0	0
$(-0.6\ ;\ -0.525]$	0	1	0
$(-0.525\ ;\ -0.45]$	0	1	0
$(-0.45\ ;\ -0.375]$	0	3	0
$(-0.375\ ;\ -0.3]$	1	15	3
$(-0.3\ ;\ -0.225]$	24	63	4
$(-0.225\ ;\ -0.15]$	131	251	42
$(-0.15\ ;\ -0.075]$	620	926	392
$(-0.075\ ;\ 0]$	3,036	2,524	3,631
$(0\ ;\ 0.075]$	3,198	3,052	3,545
$(0.075\ ;\ 0.15]$	974	1,538	954
$(0.15\ ;\ 0.225]$	414	659	419
$(0.225\ ;\ 0.3]$	264	302	207
$(0.3\ ;\ 0.375]$	174	145	150
$(0.375\ ;\ 0.45]$	128	92	73
$(0.45\ ;\ 0.525]$	116	52	60
$(0.525\ ;\ 0.6]$	84	38	51
$(0.6\ ;\ \infty]$	568	70	201

Table A.5: Absolute resolution of fraction of the incoming proton momentum carried by the pomeron reconstructed with DA.

$\Delta x_{\mathbb{P}}$	number of events	error
$(-\infty\ ;\ -0.01]$	1	1
$(-0.01\ ;\ -0.0088]$	1	1
$(-0.0088\ ;\ -0.0075]$	7	2.65
$(-0.0075\ ;\ -0.0063]$	3	1.73
$(-0.0063\ ;\ -0.005]$	14	3.74
$(-0.005\ ;\ -0.0038]$	33	5.74
$(-0.0038\ ;\ -0.0025]$	124	11.14
$(-0.0025\ ;\ -0.0013]$	673	25.94
$(-0.0013\ ;\ 0]$	3,820	61.81
$(0\ ;\ 0.0013]$	4,515	67.19
$(0.0013\ ;\ 0.0025]$	495	22.25
$(0.0025\ ;\ 0.0038]$	43	6.56
$(0.0038\ ;\ 0.005]$	2	1.41
$(0.005\ ;\ 0.0063]$	1	1
$(0.0063\ ;\ 0.0075]$	0	0
$(0.0075\ ;\ 0.0088]$	0	0
$(0.0088\ ;\ 0.01]$	0	0
$(0.01\ ;\ \infty]$	0	0

Table A.6: Relative resolution of fraction of the pomeron momentum carried by the interacting parton reconstructed with DA.

$\Delta\beta/\beta$	number of events	error
$(-\infty\ ;\ -1]$	0	0
$(-1\ ;\ -0.875]$	0	0
$(-0.875\ ;\ -0.75]$	0	0
$(-0.75\ ;\ -0.625]$	0	0
$(-0.625\ ;\ -0.5]$	0	0
$(-0.5\ ;\ -0.375]$	188	13.71
$(-0.375\ ;\ -0.25]$	748	27.35
$(-0.25\ ;\ -0.125]$	1,656	40.69
$(-0.125\ ;\ 0]$	2,574	50.73
$(0\ ;\ 0.125]$	1,996	44.68
$(0.125\ ;\ 0.25]$	1,156	34
$(0.25\ ;\ 0.375]$	601	24.52
$(0.375\ ;\ 0.5]$	343	18.52
$(0.5\ ;\ 0.625]$	174	13.19
$(0.625\ ;\ 0.75]$	115	10.72
$(0.75\ ;\ 0.875]$	66	8.12
$(0.875\ ;\ 1]$	32	5.66
$(1\ ;\ \infty]$	83	9.11

Table A.7: Distribution of separations, in pseudorapidity and azimuthal angle, of EFO with energy smaller than 400 MeV from EFOs with energy greater than 400 MeV for events with well reconstructed jets ($|\Delta p_{t,jet}/p_{t,jet}| < 0.1$).

$\sqrt{\Delta\eta^2_{\mathrm{EFO}} - \Delta\phi^2_{\mathrm{EFO}}}$	number of events	error
$(-\infty\ ;\ 0]$	0	0
$(0\ ;\ 0.4]$	$5.21 \cdot 10^3$	68.5
$(0.4\ ;\ 0.8]$	$3.93 \cdot 10^3$	59.38
$(0.8\ ;\ 1.2]$	$2.05 \cdot 10^3$	42.77
$(1.2\ ;\ 1.6]$	$1.27 \cdot 10^3$	33.97
$(1.6\ ;\ 2]$	685	25.02
$(2\ ;\ 2.4]$	$3.77 \cdot 10^2$	18.68
$(2.4\ ;\ 2.8]$	$1.6 \cdot 10^2$	12.13
$(2.8\ ;\ 3.2]$	$6.43 \cdot 10^1$	7.65
$(3.2\ ;\ 3.6]$	$2.85 \cdot 10^1$	5.05
$(3.6\ ;\ 4]$	$9.6 \cdot 10^0$	2.95
$(4\ ;\ 4.4]$	$2.65 \cdot 10^0$	1.56
$(4.4\ ;\ \infty]$	0	0

Table A.8: Distribution of separations, in pseudorapidity and azimuthal angle, of EFO with energy smaller than 400 MeV from EFOs with energy greater than 400 MeV for events with badly reconstructed jets ($\Delta p_{t,jet}/p_{t,jet} > 0.4$).

$\sqrt{\Delta\eta^2_{\mathrm{EFO}} - \Delta\phi^2_{\mathrm{EFO}}}$	number of events	error
$(-\infty\ ;\ 0]$	0	0
$(0\ ;\ 0.4]$	$5.53 \cdot 10^3$	63.77
$(0.4\ ;\ 0.8]$	$3.29 \cdot 10^3$	49.09
$(0.8\ ;\ 1.2]$	$1.96 \cdot 10^3$	37.93
$(1.2\ ;\ 1.6]$	$1.33 \cdot 10^3$	31.25
$(1.6\ ;\ 2]$	$8.3 \cdot 10^2$	24.8
$(2\ ;\ 2.4]$	$4.19 \cdot 10^2$	17.63
$(2.4\ ;\ 2.8]$	$2.73 \cdot 10^2$	14.26
$(2.8\ ;\ 3.2]$	$1.08 \cdot 10^2$	8.94
$(3.2\ ;\ 3.6]$	$3.7 \cdot 10^1$	5.25
$(3.6\ ;\ 4]$	$1.76 \cdot 10^1$	3.61
$(4\ ;\ 4.4]$	$8.05 \cdot 10^0$	2.44
$(4.4\ ;\ \infty]$	0	0

Table A.9: Resolution of detector jet transverse momentum in function of jet azimuthal angle.

	$(p_{t,jet} - p_{t,jet^{\mathrm{had}}})$ [GeV]	
ϕ_{jet}	μ	σ
$(-\infty\ ;\ -3.1416]$	0	0
$(-3.1416\ ;\ -2.7489]$	0.91	0.92
$(-2.7489\ ;\ -2.3562]$	0.43	0.71
$(-2.3562\ ;\ -1.9635]$	0.41	0.69
$(-1.9635\ ;\ -1.5708]$	0.39	0.63
$(-1.5708\ ;\ -1.1781]$	0.45	0.65
$(-1.1781\ ;\ -0.7854]$	0.41	0.64
$(-0.7854\ ;\ -0.3927]$	0.47	0.71
$(-0.3927\ ;\ 0]$	0.9	0.96
$(0\ ;\ 0.3927]$	0.92	0.9
$(0.3927\ ;\ 0.7854]$	0.44	0.7
$(0.7854\ ;\ 1.1781]$	0.41	0.68
$(1.1781\ ;\ 1.5708]$	0.4	0.62
$(1.5708\ ;\ 1.9635]$	0.46	0.64
$(1.9635\ ;\ 2.3562]$	0.39	0.64
$(2.3562\ ;\ 2.7489]$	0.46	0.73
$(2.7489\ ;\ 3.1416]$	0.9	0.96
$(3.1416\ ;\ \infty]$	0	0

Table A.10: Resolution of detector jet azimuthal angle in function of the angle itself.

	$\phi_{jet} - \phi_{jet^{\text{had}}}$	
ϕ_{jet}	μ	σ
$(-\infty\ ;\ -3.1416]$	0	0
$(-3.1416\ ;\ -2.7489]$	$-4.39 \cdot 10^{-2}$	0.59
$(-2.7489\ ;\ -2.3562]$	$-3.93 \cdot 10^{-2}$	0.37
$(-2.3562\ ;\ -1.9635]$	$9.56 \cdot 10^{-3}$	0.36
$(-1.9635\ ;\ -1.5708]$	$1.36 \cdot 10^{-3}$	0.38
$(-1.5708\ ;\ -1.1781]$	$1.54 \cdot 10^{-2}$	0.4
$(-1.1781\ ;\ -0.7854]$	$1.34 \cdot 10^{-2}$	0.34
$(-0.7854\ ;\ -0.3927]$	$5.7 \cdot 10^{-2}$	0.39
$(-0.3927\ ;\ 0]$	$2.71 \cdot 10^{-2}$	0.59
$(0\ ;\ 0.3927]$	$-3.45 \cdot 10^{-2}$	0.59
$(0.3927\ ;\ 0.7854]$	$-3.14 \cdot 10^{-2}$	0.37
$(0.7854\ ;\ 1.1781]$	$8.24 \cdot 10^{-3}$	0.36
$(1.1781\ ;\ 1.5708]$	$-1.28 \cdot 10^{-2}$	0.37
$(1.5708\ ;\ 1.9635]$	$7.58 \cdot 10^{-3}$	0.41
$(1.9635\ ;\ 2.3562]$	$1.15 \cdot 10^{-2}$	0.34
$(2.3562\ ;\ 2.7489]$	$4.8 \cdot 10^{-2}$	0.39
$(2.7489\ ;\ 3.1416]$	$3.12 \cdot 10^{-2}$	0.59
$(3.1416\ ;\ \infty]$	0	0

Table A.11: Azimuthal angular distirbution of jets reconstructed on hadron level with correct virtual photon. SATRAP 2006 electron sample was used. Events were requiered to pass the following selection criteria: $\beta > 0.45, x_{\mathbb{P}} < 0.01, 100\ \text{GeV} < W < 300\ \text{GeV}, p_{t,jet} > 2\ \text{GeV}$.

ϕ_{jet}	number of events	error
$(-\infty\ ;\ -3.1416]$	0	0
$(-3.1416\ ;\ -2.7489]$	$5.49 \cdot 10^2$	35.68
$(-2.7489\ ;\ -2.3562]$	$4.93 \cdot 10^2$	33.07
$(-2.3562\ ;\ -1.9635]$	$5.17 \cdot 10^2$	33.07
$(-1.9635\ ;\ -1.5708]$	$5.14 \cdot 10^2$	34.77
$(-1.5708\ ;\ -1.1781]$	$5.72 \cdot 10^2$	36.48
$(-1.1781\ ;\ -0.7854]$	$4.99 \cdot 10^2$	33.9
$(-0.7854\ ;\ -0.3927]$	$4.8 \cdot 10^2$	33.03
$(-0.3927\ ;\ 0]$	$5.7 \cdot 10^2$	35.84
$(0\ ;\ 0.3927]$	$5.5 \cdot 10^2$	35.81
$(0.3927\ ;\ 0.7854]$	$4.86 \cdot 10^2$	32.91
$(0.7854\ ;\ 1.1781]$	$5.19 \cdot 10^2$	32.87
$(1.1781\ ;\ 1.5708]$	$5.21 \cdot 10^2$	35.14
$(1.5708\ ;\ 1.9635]$	$5.69 \cdot 10^2$	36.43
$(1.9635\ ;\ 2.3562]$	$5 \cdot 10^2$	33.93
$(2.3562\ ;\ 2.7489]$	$4.82 \cdot 10^2$	33.06
$(2.7489\ ;\ 3.1416]$	$5.69 \cdot 10^2$	35.94
$(3.1416\ ;\ \infty]$	0	0

Table A.12: Azimuthal angular distirbution of jets reconstructed on hadron level with virtual photon four-momentum calculated as the difference between incoming and scattered lepton, which does not take into account ISR and FSR. SATRAP 2006 electron sample was used. Events were requiered to pass the following selection criteria: $\beta > 0.45, x_{\mathbb{P}} < 0.01, 100 \text{ GeV} < W < 300 \text{ GeV}, p_{t,jet} > 2 \text{ GeV}$.

ϕ_{jet}	number of events	error
$(-\infty\ ;\ -3.1416]$	0	0
$(-3.1416\ ;\ -2.7489]$	$1.61 \cdot 10^3$	54.36
$(-2.7489\ ;\ -2.3562]$	$6.67 \cdot 10^2$	35.79
$(-2.3562\ ;\ -1.9635]$	$5.08 \cdot 10^2$	30.99
$(-1.9635\ ;\ -1.5708]$	$4.3 \cdot 10^2$	29.72
$(-1.5708\ ;\ -1.1781]$	$4.91 \cdot 10^2$	31.17
$(-1.1781\ ;\ -0.7854]$	$4.41 \cdot 10^2$	29.4
$(-0.7854\ ;\ -0.3927]$	$6.67 \cdot 10^2$	36.55
$(-0.3927\ ;\ 0]$	$1.68 \cdot 10^3$	54.73
$(0\ ;\ 0.3927]$	1,613	54.41
$(0.3927\ ;\ 0.7854]$	$6.63 \cdot 10^2$	35.73
$(0.7854\ ;\ 1.1781]$	$5.08 \cdot 10^2$	30.81
$(1.1781\ ;\ 1.5708]$	$4.35 \cdot 10^2$	30.01
$(1.5708\ ;\ 1.9635]$	$4.9 \cdot 10^2$	31.14
$(1.9635\ ;\ 2.3562]$	$4.41 \cdot 10^2$	29.4
$(2.3562\ ;\ 2.7489]$	$6.7 \cdot 10^2$	36.59
$(2.7489\ ;\ 3.1416]$	$1.67 \cdot 10^3$	54.75
$(3.1416\ ;\ \infty]$	0	0

Table A.13: Differences in inelasticity reconstructed with electron and Jacquet-Blondel methods. Table shows the differences obtained with SATRAP MC after the standard selection criteria described in ch. 6 on page 49 for events with initial or final state radiation.

$y_{\text{El}} - y_{\text{JB}}$	number of events	error
$(-\infty\ ;\ -0.2]$	$1.59 \cdot 10^1$	4.61
$(-0.2\ ;\ -0.1]$	$3.62 \cdot 10^2$	28.73
$(-0.1\ ;\ 0]$	$3.76 \cdot 10^3$	104.27
$(0\ ;\ 0.1]$	$4.83 \cdot 10^3$	125.13
$(0.1\ ;\ 0.2]$	$1.68 \cdot 10^3$	73.31
$(0.2\ ;\ 0.3]$	$9.67 \cdot 10^2$	52.38
$(0.3\ ;\ 0.4]$	$5.19 \cdot 10^2$	35.56
$(0.4\ ;\ \infty]$	$3.67 \cdot 10^1$	8.08

Table A.14: Differences in inelasticity reconstructed with electron and Jacquet-Blondel methods. Table shows the differences obtained with SATRAP MC after the standard selection criteria described in ch. 6 on page 49 for events without initial or final state radiation.

$y_{\mathrm{El}} - y_{\mathrm{JB}}$	number of events	error
$(-\infty\ ;\ -0.2]$	$5.51 \cdot 10^1$	12.02
$(-0.2\ ;\ -0.1]$	$1.08 \cdot 10^3$	55.8
$(-0.1\ ;\ 0]$	$8.9 \cdot 10^3$	168.32
$(0\ ;\ 0.1]$	$8.84 \cdot 10^3$	178.41
$(0.1\ ;\ 0.2]$	$1.16 \cdot 10^3$	69.72
$(0.2\ ;\ 0.3]$	$1.31 \cdot 10^2$	22.91
$(0.3\ ;\ 0.4]$	$6.78 \cdot 10^0$	4.38
$(0.4\ ;\ \infty]$	0	0

Table A.15: Jet azimuthal angle in virtual photon-pomeron centre of mass system, after the standard selection criteria described in ch. 6 on page 49 and with $y_{\mathrm{El}} - y_{\mathrm{JB}} < 0.005$ i.e. with negligible impact of initial or final state radiation.

ϕ_{jet}	number of events	error
$(-\infty\ ;\ -3.1416]$	0	0
$(-3.1416\ ;\ -2.7489]$	54	7.35
$(-2.7489\ ;\ -2.3562]$	42	6.48
$(-2.3562\ ;\ -1.9635]$	38	6.16
$(-1.9635\ ;\ -1.5708]$	42	6.48
$(-1.5708\ ;\ -1.1781]$	45	6.71
$(-1.1781\ ;\ -0.7854]$	39	6.25
$(-0.7854\ ;\ -0.3927]$	68	8.25
$(-0.3927\ ;\ 0]$	54	7.35
$(0\ ;\ 0.3927]$	54	7.35
$(0.3927\ ;\ 0.7854]$	42	6.48
$(0.7854\ ;\ 1.1781]$	38	6.16
$(1.1781\ ;\ 1.5708]$	42	6.48
$(1.5708\ ;\ 1.9635]$	45	6.71
$(1.9635\ ;\ 2.3562]$	39	6.25
$(2.3562\ ;\ 2.7489]$	68	8.25
$(2.7489\ ;\ 3.1416]$	54	7.35
$(3.1416\ ;\ \infty]$	0	0

Table A.16: Jet azimuthal angle in virtual photon-pomeron centre of mass system, after the standard selection criteria described in ch. 6 on page 49 and with $y_{\mathrm{El}} - y_{\mathrm{JB}} > 0.2$ i.e. with dominating effects of ISR or FSR.

ϕ_{jet}	number of events	error
$(-\infty\ ;\ -3.1416]$	0	0
$(-3.1416\ ;\ -2.7489]$	101	10.05
$(-2.7489\ ;\ -2.3562]$	41	6.4
$(-2.3562\ ;\ -1.9635]$	27	5.2
$(-1.9635\ ;\ -1.5708]$	32	5.66
$(-1.5708\ ;\ -1.1781]$	29	5.39
$(-1.1781\ ;\ -0.7854]$	28	5.29
$(-0.7854\ ;\ -0.3927]$	40	6.32
$(-0.3927\ ;\ 0]$	100	10
$(0\ ;\ 0.3927]$	101	10.05
$(0.3927\ ;\ 0.7854]$	41	6.4
$(0.7854\ ;\ 1.1781]$	27	5.2
$(1.1781\ ;\ 1.5708]$	32	5.66
$(1.5708\ ;\ 1.9635]$	29	5.39
$(1.9635\ ;\ 2.3562]$	28	5.29
$(2.3562\ ;\ 2.7489]$	40	6.32
$(2.7489\ ;\ 3.1416]$	100	10
$(3.1416\ ;\ \infty]$	0	0

A.2 Signal Selection

Table A.17: Sinistra scattered lepton identification probability.

	number of events			
$\mathcal{P}_{e'}$	Data	MC	MC error	Data/MC
$(-\infty\ ;\ 0.5]$	0	0	0	0
$(0.5\ ;\ 0.7]$	3	0.32	0.32	9.28
$(0.7\ ;\ 0.9]$	45	10.48	2.46	4.29
$(0.9\ ;\ 0.99]$	102	47.5	4.51	2.15
$(0.99\ ;\ 0.9925]$	25	15.65	2.67	1.6
$(0.9925\ ;\ 0.995]$	33	37	4.11	0.89
$(0.995\ ;\ 0.9975]$	189	146.53	8.29	1.29
$(0.9975\ ;\ 1]$	4,079	4,207.4	44.95	0.97
$(1\ ;\ \infty]$	0	0	0	0

Table A.18: Scattered lepton energy reconstructed with double-angle method.

	number of events			
$E_{e'}$ [GeV]	Data	MC	MC error	Data/MC
$(-\infty$; 7.5]	1	1.14	0.67	0.88
(7.5 ; 8.75]	3	2.88	1.07	1.04
(8.75 ; 10]	18	19.9	3.01	0.9
(10 ; 11.25]	53	60.61	5.4	0.87
(11.25 ; 12.5]	128	158.57	8.77	0.81
(12.5 ; 13.75]	235	222.74	10.29	1.06
(13.75 ; 15]	260	268.3	11.1	0.97
(15 ; 16.25]	335	324.35	12.33	1.03
(16.25 ; 17.5]	350	370.1	13.13	0.95
(17.5 ; 18.75]	453	403.9	13.7	1.12
(18.75 ; 20]	494	477.98	15.03	1.03
(20 ; 21.25]	526	539.15	16.06	0.98
(21.25 ; 22.5]	577	603.14	17.15	0.96
(22.5 ; 23.75]	566	587.61	17.06	0.96
(23.75 ; 25]	428	433.62	14.81	0.99
(25 ; 26.25]	111	106.04	7.06	1.05
(26.25 ; 27.5]	0	0.44	0.44	0
(27.5 ; ∞]	0	0	0	0

Table A.19: Photon virtuality reconstructed with double-angle method.

	number of events			
Q^2_{DA} [GeV^2]	Data	MC	MC error	Data/MC
$(-\infty$; 25]	0	0	0	0
(25 ; 45]	510	566.49	15.27	0.9
(45 ; 65]	1,122	1,096.34	22.22	1.02
(65 ; 85]	923	934.23	21.14	0.99
(85 ; 105]	643	640.19	17.84	1
(105 ; 125]	447	406.68	14.28	1.1
(125 ; 145]	252	263.51	11.66	0.96
(145 ; 165]	162	166.4	9.42	0.97
(165 ; 185]	127	132.37	8.7	0.96
(185 ; 205]	91	95.56	7.25	0.95
(205 ; 225]	66	59.77	5.64	1.1
(225 ; 245]	41	40.18	4.8	1.02
(245 ; 295]	34	42.69	4.96	0.8
(295 ; ∞]	10	9.67	2.3	1.03

Table A.20: Photon-proton invariant mass reconstructed with double-angle method.

	number of events			
W_{DA} [GeV]	Data	MC	MC error	Data/MC
$(-\infty\ ;\ 70]$	0	0	0	0
$(70\ ;\ 90]$	15	14.2	2.46	1.06
$(90\ ;\ 110]$	158	147.13	8.45	1.07
$(110\ ;\ 130]$	447	476.53	15.4	0.94
$(130\ ;\ 150]$	660	684.03	18.32	0.96
$(150\ ;\ 170]$	734	741.45	18.87	0.99
$(170\ ;\ 190]$	732	726.82	18.49	1.01
$(190\ ;\ 210]$	703	643.62	17.32	1.09
$(210\ ;\ 230]$	551	588.62	16.66	0.94
$(230\ ;\ 250]$	443	445.88	14.62	0.99
$(250\ ;\ 270]$	73	88.27	6.79	0.83
$(270\ ;\ \infty]$	0	0	0	0

Table A.21: Distance separating scattered lepton energy deposit in calorimeter from extrapolated track associated with scattered lepton. Negative values mean that no track was assigned to scattered lepton.

	number of events			
d_{ca} [cm]	Data	MC	MC error	Data/MC
$(-\infty\ ;\ 0]$	448	270.26	10.97	1.66
$(0\ ;\ 2]$	2,060	2,586.64	35.41	0.8
$(2\ ;\ 4]$	950	824.43	19.89	1.15
$(4\ ;\ 6]$	289	255.21	10.95	1.13
$(6\ ;\ 8]$	179	147.73	8.4	1.21
$(8\ ;\ 10]$	133	110.21	7.28	1.21
$(10\ ;\ 12]$	98	88.55	6.37	1.11
$(12\ ;\ 14]$	89	57.44	5.16	1.55
$(14\ ;\ 16]$	74	50.86	4.99	1.45
$(16\ ;\ 18]$	54	32.22	3.72	1.68
$(18\ ;\ 20]$	54	30.53	3.74	1.77
$(20\ ;\ \infty]$	0	0	0	0

Table A.22: Sinistra lepton identification probability.

	number of events			
y_{El}	Data	MC	MC error	Data/MC
$(-\infty\ ;\ 0.01]$	16	4.72	1.41	3.39
$(0.01\ ;\ 0.1]$	243	213.28	10.19	1.14
$(0.1\ ;\ 0.19]$	793	764.76	19.57	1.04
$(0.19\ ;\ 0.28]$	945	975.83	21.86	0.97
$(0.28\ ;\ 0.37]$	896	887.17	20.38	1.01
$(0.37\ ;\ 0.46]$	739	764.64	18.98	0.97
$(0.46\ ;\ 0.55]$	628	664.94	17.6	0.94
$(0.55\ ;\ 0.64]$	427	396.74	13.68	1.08
$(0.64\ ;\ 0.73]$	124	104.99	7.24	1.18
$(0.73\ ;\ 0.82]$	21	9.28	1.95	2.26
$(0.82\ ;\ 0.91]$	1	0.94	0.68	1.07
$(0.91\ ;\ \infty]$	0	0	0	0

Table A.23: Vertex position along the beam pipe.

	number of events			
Z_{vtx} [cm]	Data	MC	MC error	Data/MC
$(-\infty\ ;\ -50]$	107	79.9	5.3	1.34
$(-50\ ;\ -40]$	11	10.34	2.12	1.06
$(-40\ ;\ -30]$	27	20.91	3.17	1.29
$(-30\ ;\ -20]$	115	110.1	7.33	1.04
$(-20\ ;\ -10]$	644	643.54	17.5	1
$(-10\ ;\ 0]$	1,606	1,573.12	27.37	1.02
$(0\ ;\ 10]$	1,487	1,515.46	27.01	0.98
$(10\ ;\ 20]$	501	534.17	16.06	0.94
$(20\ ;\ 30]$	75	77.69	6.11	0.97
$(30\ ;\ 40]$	14	25.81	3.57	0.54
$(40\ ;\ 50]$	12	12.28	2.59	0.98
$(50\ ;\ \infty]$	58	41.31	4.4	1.4

Table A.24: Number of tracks associated with vertex.

	number of events			
N_{trk}	Data	MC	MC error	Data/MC
$(-\infty\ ;\ -0.5]$	0	0	0	0
$(-0.5\ ;\ 0.5]$	0	2.23	0.98	0
$(0.5\ ;\ 1.5]$	24	13.82	2.22	1.74
$(1.5\ ;\ 2.5]$	120	105.13	6.58	1.14
$(2.5\ ;\ 3.5]$	319	336.55	12.21	0.95
$(3.5\ ;\ 4.5]$	456	458.13	14.52	1
$(4.5\ ;\ 5.5]$	768	729.4	18.58	1.05
$(5.5\ ;\ 6.5]$	730	724.32	18.83	1.01
$(6.5\ ;\ 7.5]$	723	744.45	19.03	0.97
$(7.5\ ;\ 8.5]$	502	498.5	15.67	1.01
$(8.5\ ;\ 9.5]$	341	403.13	14.32	0.85
$(9.5\ ;\ 10.5]$	219	209.95	10.08	1.04
$(10.5\ ;\ 11.5]$	116	119.78	7.73	0.97
$(11.5\ ;\ 12.5]$	62	64.42	5.56	0.96
$(12.5\ ;\ 13.5]$	31	29.1	3.66	1.07
$(13.5\ ;\ 14.5]$	14	9.44	2.02	1.48
$(14.5\ ;\ 15.5]$	1	6.42	1.59	0.16
$(15.5\ ;\ \infty]$	2	1.55	0.73	1.29

Table A.25: Number of particles in hadronic final state.

	number of events			
N_{EFO}	Data	MC	MC error	Data/MC
$(-\infty\ ;\ -0.5]$	0	0	0	0
$(-0.5\ ;\ 1.5]$	0	0	0	0
$(1.5\ ;\ 3.5]$	0	0	0	0
$(3.5\ ;\ 5.5]$	54	30.08	3.25	1.8
$(5.5\ ;\ 7.5]$	145	166.47	8.47	0.87
$(7.5\ ;\ 9.5]$	374	426.51	13.8	0.88
$(9.5\ ;\ 11.5]$	677	700	18.05	0.97
$(11.5\ ;\ 13.5]$	867	844.01	20.13	1.03
$(13.5\ ;\ 15.5]$	877	808.4	19.84	1.08
$(15.5\ ;\ 17.5]$	662	630.62	17.71	1.05
$(17.5\ ;\ 19.5]$	410	436.37	14.75	0.94
$(19.5\ ;\ 21.5]$	205	219.47	10.43	0.93
$(21.5\ ;\ 23.5]$	84	122.68	7.96	0.68
$(23.5\ ;\ 25.5]$	49	47.06	4.88	1.04
$(25.5\ ;\ 27.5]$	12	15.64	2.59	0.77
$(27.5\ ;\ 29.5]$	8	4.6	1.33	1.74
$(29.5\ ;\ \infty]$	4	2.17	0.83	1.85

Table A.26: Fraction of total energy deposited in hadronic calorimeter.

	number of events			
$E_{\text{had}}/E_{\text{tot}}$	Data	MC	MC error	Data/MC
$(-\infty\ ;\ 0]$	0	0	0	0
$(0\ ;\ 0.06]$	499	386.03	13.41	1.29
$(0.06\ ;\ 0.12]$	540	482.32	15.06	1.12
$(0.12\ ;\ 0.18]$	610	619.11	17.31	0.99
$(0.18\ ;\ 0.24]$	606	652.58	17.68	0.93
$(0.24\ ;\ 0.3]$	613	641.22	17.55	0.96
$(0.3\ ;\ 0.36]$	538	574.78	16.62	0.94
$(0.36\ ;\ 0.42]$	452	460.66	14.89	0.98
$(0.42\ ;\ 0.48]$	341	351.1	12.96	0.97
$(0.48\ ;\ 0.54]$	241	256.43	11.03	0.94
$(0.54\ ;\ 0.6]$	209	172.19	9.12	1.21
$(0.6\ ;\ 0.66]$	141	121.14	7.57	1.16
$(0.66\ ;\ 0.72]$	67	69.53	5.78	0.96
$(0.72\ ;\ 0.78]$	40	34.26	4.05	1.17
$(0.78\ ;\ 0.84]$	17	13.97	2.52	1.22
$(0.84\ ;\ 0.9]$	12	3.92	1.34	3.06
$(0.9\ ;\ \infty]$	1	0.87	0.57	1.14

Table A.27: Energy-momentum along the beam pipe balance.

	number of events			
$E_{\text{tot}} - p_{z,\text{tot}}$ [GeV]	Data	MC	MC error	Data/MC
$(-\infty\ ;\ 40]$	3	1.35	0.67	2.22
$(40\ ;\ 42.5]$	5	5.61	1.64	0.89
$(42.5\ ;\ 45]$	23	15.4	2.85	1.49
$(45\ ;\ 47.5]$	57	50.32	4.58	1.13
$(47.5\ ;\ 50]$	211	184.55	9.36	1.14
$(50\ ;\ 52.5]$	528	510.8	15.59	1.03
$(52.5\ ;\ 55]$	1,369	1,323.57	25.44	1.03
$(55\ ;\ 57.5]$	1,476	1,518.76	27.14	0.97
$(57.5\ ;\ 60]$	530	601.7	16.73	0.88
$(60\ ;\ 62.5]$	172	187.74	9.2	0.92
$(62.5\ ;\ 65]$	61	56.39	4.9	1.08
$(65\ ;\ 67.5]$	19	15.33	2.67	1.24
$(67.5\ ;\ 70]$	5	4.92	1.49	1.02
$(70\ ;\ 72.5]$	2	0.19	0.19	10.4
$(72.5\ ;\ 75]$	1	0.88	0.64	1.14
$(75\ ;\ \infty]$	0	0.9	0.52	0

Table A.28: Maximum pseudorapidity of particles with energy greater than 400 MeV in an event.

	number of events			
$\eta_{\max}$	Data	MC	MC error	Data/MC
$(-\infty\ ;\ -1.5]$	0	0.35	0.35	0
$(-1.5\ ;\ -1]$	48	47.57	4.31	1.01
$(-1\ ;\ -0.5]$	468	388.49	12.66	1.2
$(-0.5\ ;\ 0]$	983	951.5	20.45	1.03
$(0\ ;\ 0.5]$	1,235	1,203.44	23.92	1.03
$(0.5\ ;\ 1]$	1,084	1,066.49	23.31	1.02
$(1\ ;\ 1.5]$	429	552.75	17.16	0.78
$(1.5\ ;\ 2]$	181	243.49	11.25	0.74
$(2\ ;\ 2.5]$	80	104.39	7.82	0.77
$(2.5\ ;\ \infty]$	111	70.88	6.27	1.57

Table A.29: Reconstructed fraction of incoming proton momentum carried by pomeron.

	number of events			
$\log_{10}(x_{\mathbb{P}})$	Data	MC	MC error	Data/MC
$(-\infty\ ;\ -3]$	0	0.57	0.42	0
$(-3\ ;\ -2.8]$	71	82.12	5.59	0.86
$(-2.8\ ;\ -2.6]$	453	443.22	13.39	1.02
$(-2.6\ ;\ -2.4]$	1,045	1,027.22	21.2	1.02
$(-2.4\ ;\ -2.2]$	1,441	1,462.44	26.53	0.99
$(-2.2\ ;\ -2]$	1,418	1,438.51	27.75	0.99
$(-2\ ;\ -1.8]$	959	967.34	23.84	0.99
$(-1.8\ ;\ -1.6]$	414	359.19	15.34	1.15
$(-1.6\ ;\ -1.4]$	104	97.31	8.11	1.07
$(-1.4\ ;\ \infty]$	20	8.3	2.38	2.41

Table A.30: Invariant mass of hadronic system.

	number of events			
M [GeV]	Data	MC	MC error	Data/MC
$(-\infty\ ;\ 4]$	0	0	0	0
$(4\ ;\ 5]$	68	66.44	5	1.02
$(5\ ;\ 6]$	573	653.7	16.38	0.88
$(6\ ;\ 7]$	1,135	1,064.93	21.97	1.07
$(7\ ;\ 8]$	982	1,013.27	22.04	0.97
$(8\ ;\ 9]$	722	706.51	18.81	1.02
$(9\ ;\ 10]$	441	407.1	14.36	1.08
$(10\ ;\ 11]$	243	265.92	11.9	0.91
$(11\ ;\ 12]$	160	154.09	9.2	1.04
$(12\ ;\ 13]$	100	107.28	7.98	0.93
$(13\ ;\ 14]$	39	53.92	5.64	0.72
$(14\ ;\ 15]$	23	17.94	3.01	1.28
$(15\ ;\ 16]$	8	8.13	2.19	0.98
$(16\ ;\ \infty]$	2	1.28	0.78	1.57

Table A.31: Fraction of pomeron momentum carried by the interacting parton.

	number of events				
β	Data	MC	QQ	QQG	Data/MC
$(-\infty\ ;\ 0]$	0	0	0	0	0
$(0\ ;\ 0.0714]$	426	7.85	7.27	0.58	54.29
$(0.0714\ ;\ 0.1429]$	5,118	249.44	184.61	64.83	20.52
$(0.1429\ ;\ 0.2143]$	7,225	2,247.41	1,290.97	956.45	3.21
$(0.2143\ ;\ 0.2857]$	7,248	5,442.35	3,107.41	2,334.94	1.33
$(0.2857\ ;\ 0.3571]$	6,815	6,334.98	4,100.26	2,234.72	1.08
$(0.3571\ ;\ 0.4286]$	5,464	5,448.07	3,967.81	1,480.26	1
$(0.4286\ ;\ 0.5]$	3,865	3,984.46	3,225.57	758.89	0.97
$(0.5\ ;\ 0.5714]$	2,436	2,450.66	2,100.36	350.3	0.99
$(0.5714\ ;\ 0.6429]$	1,368	1,387.46	1,246.27	141.2	0.99
$(0.6429\ ;\ 0.7143]$	750	706.16	657.29	48.86	1.06
$(0.7143\ ;\ 0.7857]$	241	273.21	261.48	11.73	0.88
$(0.7857\ ;\ 0.8571]$	74	75.35	73.62	1.73	0.98
$(0.8571\ ;\ 0.9286]$	7	7.08	7.08	0	0.99
$(0.9286\ ;\ 1]$	0	0	0	0	0
$(1\ ;\ \infty]$	0	0	0	0	0

Table A.32: Jet transverse momentum in virtual photon-pomeron centre of mass system.

	number of events			
$p_{t,jet}$ [GeV]	Data	MC	MC error	Data/MC
$(-\infty\ ;\ 0]$	0	0	0	0
$(0\ ;\ 0.5]$	3,145	12,395	79.24	0.25
$(0.5\ ;\ 1]$	8,179	25,107.7	111.6	0.33
$(1\ ;\ 1.5]$	9,902	18,904.4	95.21	0.52
$(1.5\ ;\ 2]$	6,946	9,640.09	67.23	0.72
$(2\ ;\ 2.5]$	2,881	3,095.09	38.24	0.93
$(2.5\ ;\ 3]$	993	875.71	20.61	1.13
$(3\ ;\ 3.5]$	322	291.46	12.07	1.1
$(3.5\ ;\ 4]$	165	111.95	7.69	1.47
$(4\ ;\ 4.5]$	34	44.86	4.77	0.76
$(4.5\ ;\ 5]$	24	24.31	3.73	0.99
$(5\ ;\ 5.5]$	6	7.85	1.92	0.76
$(5.5\ ;\ 6]$	3	2.67	1.16	1.12
$(6\ ;\ \infty]$	0	0.19	0.19	0

A.3 Systematic Uncertainties

Table A.33: Differences in unfolded distribution of jet azimuthal angle obtained with standard and varied parameters after normalisation.

ϕ_{jet}	$Q^2_{\mathrm{DA}} > 26.7\ \mathrm{GeV}^2$	$Q^2_{\mathrm{DA}} > 23.3\ \mathrm{GeV}^2$	$\eta_{\max} < 0.22$	$\eta_{\max} < 0.18$
$(0\ ;\ 0.3927]$	$3.21 \cdot 10^{-3}$	0	$6.97 \cdot 10^{-2}$	$-8.68 \cdot 10^{-2}$
$(0.3927\ ;\ 0.7854]$	$-1.24 \cdot 10^{-3}$	0	$1.26 \cdot 10^{-2}$	$-3.01 \cdot 10^{-2}$
$(0.7854\ ;\ 1.1781]$	$1.09 \cdot 10^{-2}$	0	$5.28 \cdot 10^{-2}$	$-6.45 \cdot 10^{-2}$
$(1.1781\ ;\ 1.5708]$	$-3.13 \cdot 10^{-3}$	0	$3.05 \cdot 10^{-2}$	$-3.22 \cdot 10^{-2}$
$(1.5708\ ;\ 1.9635]$	$1.63 \cdot 10^{-3}$	0	$3.75 \cdot 10^{-2}$	$-4.43 \cdot 10^{-2}$
$(1.9635\ ;\ 2.3562]$	$-5.97 \cdot 10^{-4}$	0	$3.56 \cdot 10^{-2}$	$-5.61 \cdot 10^{-2}$
$(2.3562\ ;\ 2.7489]$	$-9.05 \cdot 10^{-5}$	0	$3.79 \cdot 10^{-2}$	$-5.08 \cdot 10^{-2}$
$(2.7489\ ;\ 3.1416]$	$2.16 \cdot 10^{-3}$	0	$8.68 \cdot 10^{-2}$	$-7.91 \cdot 10^{-2}$

Table A.34: Differences in unfolded distribution of jet azimuthal angle obtained with standard and varied parameters after normalisation.

ϕ_{jet}	$97.4 < W_{\mathrm{DA}}/\mathrm{GeV} < 241.6$	$82.6 < W_{\mathrm{DA}}/\mathrm{GeV} < 258.4$
$(0\ ;\ 0.3927]$	$3.3 \cdot 10^{-2}$	$1.36 \cdot 10^{-2}$
$(0.3927\ ;\ 0.7854]$	$-4.53 \cdot 10^{-2}$	$8.69 \cdot 10^{-3}$
$(0.7854\ ;\ 1.1781]$	$-3.02 \cdot 10^{-2}$	$2.58 \cdot 10^{-2}$
$(1.1781\ ;\ 1.5708]$	$-5.97 \cdot 10^{-3}$	$-1.98 \cdot 10^{-2}$
$(1.5708\ ;\ 1.9635]$	$-1.45 \cdot 10^{-2}$	$4.11 \cdot 10^{-2}$
$(1.9635\ ;\ 2.3562]$	$4.06 \cdot 10^{-2}$	$1.84 \cdot 10^{-3}$
$(2.3562\ ;\ 2.7489]$	$-6.68 \cdot 10^{-2}$	$-2.85 \cdot 10^{-2}$
$(2.7489\ ;\ 3.1416]$	$5.73 \cdot 10^{-3}$	$2.4 \cdot 10^{-2}$

Table A.35: Differences in unfolded distribution of jet azimuthal angle obtained with standard and varied parameters after normalisation.

ϕ_{jet}	$M > 6.2$ GeV	$M > 3.8$ GeV	$q\bar{q}/q\bar{q}g = 1/0.8$	$q\bar{q}/q\bar{q}g = 1/0.34$
(0 ; 0.3927]	$-2.6 \cdot 10^{-1}$	$1.44 \cdot 10^{-2}$	$-2.46 \cdot 10^{-3}$	$1.72 \cdot 10^{-3}$
(0.3927 ; 0.7854]	$1.2 \cdot 10^{-2}$	$-1.86 \cdot 10^{-2}$	$-2.84 \cdot 10^{-2}$	$2.54 \cdot 10^{-2}$
(0.7854 ; 1.1781]	$-2.65 \cdot 10^{-2}$	$-1.79 \cdot 10^{-2}$	$-1.47 \cdot 10^{-2}$	$1.27 \cdot 10^{-2}$
(1.1781 ; 1.5708]	$-7.72 \cdot 10^{-2}$	$-3.5 \cdot 10^{-2}$	$-2.94 \cdot 10^{-3}$	$2.17 \cdot 10^{-3}$
(1.5708 ; 1.9635]	$-7.87 \cdot 10^{-2}$	$-3.74 \cdot 10^{-2}$	$-9.28 \cdot 10^{-3}$	$7.54 \cdot 10^{-3}$
(1.9635 ; 2.3562]	$5.48 \cdot 10^{-2}$	$1.79 \cdot 10^{-3}$	$1.78 \cdot 10^{-3}$	$-2.62 \cdot 10^{-3}$
(2.3562 ; 2.7489]	$9.47 \cdot 10^{-2}$	$-9.24 \cdot 10^{-3}$	$-2.38 \cdot 10^{-2}$	$2.11 \cdot 10^{-2}$
(2.7489 ; 3.1416]	$-1.08 \cdot 10^{-1}$	$-1.81 \cdot 10^{-2}$	$-1.11 \cdot 10^{-2}$	$9.26 \cdot 10^{-3}$

Table A.36: Differences in unfolded distribution of jet azimuthal angle obtained with standard and varied parameters after normalisation.

ϕ_{jet}	$x_{\mathbb{P}} < 0.0109$	$x_{\mathbb{P}} < 0.0091$	$\lvert Z_{\text{vtx}}\rvert < 28.5$ cm	$\lvert Z_{\text{vtx}}\rvert < 31.5$ cm
(0 ; 0.3927]	$3.95 \cdot 10^{-2}$	$3.02 \cdot 10^{-1}$	$4.96 \cdot 10^{-3}$	$-8.37 \cdot 10^{-3}$
(0.3927 ; 0.7854]	$4.88 \cdot 10^{-2}$	$2.3 \cdot 10^{-1}$	$-8.25 \cdot 10^{-3}$	$8.44 \cdot 10^{-3}$
(0.7854 ; 1.1781]	$5.79 \cdot 10^{-2}$	$3.73 \cdot 10^{-1}$	$1.69 \cdot 10^{-3}$	$2.84 \cdot 10^{-3}$
(1.1781 ; 1.5708]	$2.54 \cdot 10^{-2}$	$2.38 \cdot 10^{-1}$	$7.85 \cdot 10^{-4}$	$-9.48 \cdot 10^{-3}$
(1.5708 ; 1.9635]	$1.81 \cdot 10^{-2}$	$1.57 \cdot 10^{-1}$	$-2.93 \cdot 10^{-3}$	$-5.98 \cdot 10^{-3}$
(1.9635 ; 2.3562]	$-3.95 \cdot 10^{-3}$	$1.91 \cdot 10^{-1}$	$-5.64 \cdot 10^{-4}$	$4.96 \cdot 10^{-3}$
(2.3562 ; 2.7489]	$2.69 \cdot 10^{-2}$	$3.22 \cdot 10^{-1}$	$1.42 \cdot 10^{-2}$	$-1.62 \cdot 10^{-2}$
(2.7489 ; 3.1416]	$1.3 \cdot 10^{-2}$	$3.31 \cdot 10^{-1}$	$4.49 \cdot 10^{-3}$	$1.36 \cdot 10^{-2}$

Table A.37: Differences in unfolded distribution of jet azimuthal angle obtained with standard and varied parameters after normalisation.

ϕ_{jet}	$0.139 < y_{\text{El}} < 0.611$	$0.061 < y_{\text{El}} < 0.669$	$\sigma_E \times 1.02$	$\sigma_E \times 0.96$
(0 ; 0.3927]	$-2.32 \cdot 10^{-2}$	$8.82 \cdot 10^{-2}$	$-9.45 \cdot 10^{-2}$	$1.38 \cdot 10^{-1}$
(0.3927 ; 0.7854]	$-1.27 \cdot 10^{-1}$	$-3.19 \cdot 10^{-2}$	$4.41 \cdot 10^{-2}$	$9.81 \cdot 10^{-2}$
(0.7854 ; 1.1781]	$-1.55 \cdot 10^{-2}$	$3.36 \cdot 10^{-2}$	$-1.67 \cdot 10^{-2}$	$1.66 \cdot 10^{-1}$
(1.1781 ; 1.5708]	$-5.94 \cdot 10^{-2}$	$-1.31 \cdot 10^{-2}$	$3.53 \cdot 10^{-2}$	$5.5 \cdot 10^{-2}$
(1.5708 ; 1.9635]	$-3.89 \cdot 10^{-2}$	$-5.19 \cdot 10^{-2}$	$4.68 \cdot 10^{-3}$	$1.16 \cdot 10^{-1}$
(1.9635 ; 2.3562]	$-1.13 \cdot 10^{-2}$	$7.64 \cdot 10^{-2}$	$3.68 \cdot 10^{-2}$	$1.05 \cdot 10^{-1}$
(2.3562 ; 2.7489]	$1.21 \cdot 10^{-2}$	$1.65 \cdot 10^{-2}$	$4.67 \cdot 10^{-2}$	$2.44 \cdot 10^{-1}$
(2.7489 ; 3.1416]	$-1.34 \cdot 10^{-1}$	$8.65 \cdot 10^{-2}$	$-1.21 \cdot 10^{-1}$	$1.66 \cdot 10^{-1}$

Table A.38: Differences in unfolded distribution of jet azimuthal angle obtained with standard and varied parameters after normalisation.

ϕ_{jet}	$X_{e'} + 2$ mm	$X_{e'} - 2$ mm	$Y_{e'} + 2$ mm	$Y_{e'} - 2$ mm
(0 ; 0.3927]	$1.54 \cdot 10^{-2}$	$1.41 \cdot 10^{-2}$	$1.02 \cdot 10^{-2}$	$-7.53 \cdot 10^{-3}$
(0.3927 ; 0.7854]	$-1.49 \cdot 10^{-2}$	$-2.69 \cdot 10^{-2}$	$-3.3 \cdot 10^{-2}$	$4.08 \cdot 10^{-3}$
(0.7854 ; 1.1781]	$-1.96 \cdot 10^{-2}$	$8.68 \cdot 10^{-3}$	$1.71 \cdot 10^{-2}$	$-7.61 \cdot 10^{-3}$
(1.1781 ; 1.5708]	$-5.07 \cdot 10^{-3}$	$6.97 \cdot 10^{-3}$	$-9.42 \cdot 10^{-3}$	$-2.38 \cdot 10^{-3}$
(1.5708 ; 1.9635]	$8.65 \cdot 10^{-3}$	$-1.53 \cdot 10^{-2}$	$3.79 \cdot 10^{-3}$	$-7.13 \cdot 10^{-3}$
(1.9635 ; 2.3562]	$2.45 \cdot 10^{-3}$	$2.87 \cdot 10^{-2}$	$9.83 \cdot 10^{-3}$	$1.85 \cdot 10^{-2}$
(2.3562 ; 2.7489]	$9.22 \cdot 10^{-3}$	$-1.39 \cdot 10^{-2}$	$1.1 \cdot 10^{-2}$	$-1.28 \cdot 10^{-2}$
(2.7489 ; 3.1416]	$-1.59 \cdot 10^{-2}$	$-3.91 \cdot 10^{-2}$	$-9.69 \cdot 10^{-3}$	$-1.32 \cdot 10^{-3}$

Table A.39: Differences in unfolded distribution of jet azimuthal angle obtained with standard and varied parameters after normalisation.

ϕ_{jet}	$Z_{e'} + 2$ mm	$Z_{e'} - 2$ mm	$E \times 1.03$	$E \times 0.97$
(0 ; 0.3927]	$-1.55 \cdot 10^{-2}$	$2.1 \cdot 10^{-3}$	$-1.46 \cdot 10^{-1}$	$1.39 \cdot 10^{-2}$
(0.3927 ; 0.7854]	$1.24 \cdot 10^{-2}$	$-1.26 \cdot 10^{-2}$	$6.49 \cdot 10^{-2}$	$1.07 \cdot 10^{-1}$
(0.7854 ; 1.1781]	$-1.4 \cdot 10^{-2}$	$-8.3 \cdot 10^{-3}$	$3.73 \cdot 10^{-2}$	$7.99 \cdot 10^{-3}$
(1.1781 ; 1.5708]	$-1.18 \cdot 10^{-4}$	$-1.31 \cdot 10^{-3}$	$-3.59 \cdot 10^{-2}$	$1.4 \cdot 10^{-1}$
(1.5708 ; 1.9635]	$-3.39 \cdot 10^{-3}$	$-3.84 \cdot 10^{-3}$	$-3.43 \cdot 10^{-2}$	$-5.3 \cdot 10^{-2}$
(1.9635 ; 2.3562]	$2.24 \cdot 10^{-3}$	$1.89 \cdot 10^{-2}$	$6.62 \cdot 10^{-2}$	$6.7 \cdot 10^{-2}$
(2.3562 ; 2.7489]	$-9.61 \cdot 10^{-3}$	$2.16 \cdot 10^{-2}$	$-9.54 \cdot 10^{-2}$	$8.94 \cdot 10^{-5}$
(2.7489 ; 3.1416]	$8.42 \cdot 10^{-3}$	$-9.4 \cdot 10^{-3}$	$3.02 \cdot 10^{-2}$	$1.53 \cdot 10^{-1}$

Table A.40: Differences in unfolded distribution of photon virtuality obtained with standard and varied parameters after normalisation.

Q^2_{DA} [GeV^2]	$Q^2_{\mathrm{DA}} > 26.7$ GeV^2	$Q^2_{\mathrm{DA}} > 23.3$ GeV^2	$\eta_{\max} < 0.22$	$\eta_{\max} < 0.18$
(25 ; 50]	$6.89 \cdot 10^{-2}$	0	$5.07 \cdot 10^{-2}$	$-8.49 \cdot 10^{-3}$
(50 ; 65]	$-1.66 \cdot 10^{-2}$	0	$2.5 \cdot 10^{-2}$	$-4.17 \cdot 10^{-2}$
(65 ; 105]	$-1.01 \cdot 10^{-3}$	0	$3.24 \cdot 10^{-2}$	$-4.01 \cdot 10^{-2}$
(105 ; 145]	$1.14 \cdot 10^{-5}$	0	$2.7 \cdot 10^{-2}$	$-2.37 \cdot 10^{-2}$
(145 ; 185]	$5.61 \cdot 10^{-4}$	0	$2.75 \cdot 10^{-2}$	$-4.61 \cdot 10^{-2}$
(185 ; 225]	$7.87 \cdot 10^{-5}$	0	$3.24 \cdot 10^{-2}$	$-8.53 \cdot 10^{-3}$
(225 ; 295]	$9.05 \cdot 10^{-5}$	0	$2.32 \cdot 10^{-2}$	$-5.15 \cdot 10^{-2}$

Table A.41: Differences in unfolded distribution of photon virtuality obtained with standard and varied parameters after normalisation.

Q^2_{DA} [GeV^2]	$97.4 < W_{\mathrm{DA}}/\mathrm{GeV} < 241.6$	$82.6 < W_{\mathrm{DA}}/\mathrm{GeV} < 258.4$
(25 ; 50]	$-3.84 \cdot 10^{-2}$	$1.77 \cdot 10^{-2}$
(50 ; 65]	$-3.17 \cdot 10^{-2}$	$1.44 \cdot 10^{-3}$
(65 ; 105]	$-2.78 \cdot 10^{-2}$	$1.69 \cdot 10^{-2}$
(105 ; 145]	$-1.89 \cdot 10^{-2}$	$2.26 \cdot 10^{-2}$
(145 ; 185]	$-1.04 \cdot 10^{-1}$	$-3.81 \cdot 10^{-3}$
(185 ; 225]	$-5.02 \cdot 10^{-2}$	$9.52 \cdot 10^{-2}$
(225 ; 295]	$-1.1 \cdot 10^{-1}$	$4.49 \cdot 10^{-2}$

Table A.42: Differences in unfolded distribution of photon virtuality obtained with standard and varied parameters after normalisation.

Q^2_{DA} [GeV^2]	$M > 6.2$ GeV	$M > 3.8$ GeV	$q\bar{q}/q\bar{q}g = 1/0.8$	$q\bar{q}/q\bar{q}g = 1/0.34$
(25 ; 50]	$-7.76 \cdot 10^{-1}$	$7.54 \cdot 10^{-2}$	$5.17 \cdot 10^{-4}$	$-2.34 \cdot 10^{-4}$
(50 ; 65]	$-1.63 \cdot 10^{-1}$	$2.41 \cdot 10^{-1}$	$-2.38 \cdot 10^{-2}$	$2.14 \cdot 10^{-2}$
(65 ; 105]	$-6.05 \cdot 10^{-2}$	$-3.54 \cdot 10^{-2}$	$-1.21 \cdot 10^{-2}$	$1.08 \cdot 10^{-2}$
(105 ; 145]	$1.06 \cdot 10^{-2}$	$-6.08 \cdot 10^{-3}$	$-1.09 \cdot 10^{-2}$	$9.4 \cdot 10^{-3}$
(145 ; 185]	$1.29 \cdot 10^{-2}$	$-1.76 \cdot 10^{-2}$	$-1.31 \cdot 10^{-2}$	$1.1 \cdot 10^{-2}$
(185 ; 225]	$1.34 \cdot 10^{-2}$	$-1.18 \cdot 10^{-2}$	$-2.84 \cdot 10^{-3}$	$1.34 \cdot 10^{-3}$
(225 ; 295]	$-2.07 \cdot 10^{-4}$	$-5.63 \cdot 10^{-3}$	$-1.18 \cdot 10^{-3}$	$-3.91 \cdot 10^{-4}$

Table A.43: Differences in unfolded distribution of photon virtuality obtained with standard and varied parameters after normalisation.

Q^2_{DA} [GeV^2]	$x_{\mathbb{P}} < 0.0109$	$x_{\mathbb{P}} < 0.0091$	$\lvert Z_{\mathrm{vtx}}\rvert < 28.5$ cm	$\lvert Z_{\mathrm{vtx}}\rvert < 31.5$ cm
(25 ; 50]	$-3.73 \cdot 10^{-2}$	$1.38 \cdot 10^{-1}$	$3.07 \cdot 10^{-3}$	$-4.13 \cdot 10^{-3}$
(50 ; 65]	$3.35 \cdot 10^{-2}$	$4.89 \cdot 10^{-2}$	$5.07 \cdot 10^{-3}$	$-1.03 \cdot 10^{-3}$
(65 ; 105]	$4.62 \cdot 10^{-2}$	$1.57 \cdot 10^{-1}$	$2.05 \cdot 10^{-3}$	$-3.86 \cdot 10^{-3}$
(105 ; 145]	$7.33 \cdot 10^{-2}$	$3.97 \cdot 10^{-1}$	$6.13 \cdot 10^{-3}$	$-7.53 \cdot 10^{-3}$
(145 ; 185]	$1.35 \cdot 10^{-1}$	$8.21 \cdot 10^{-1}$	$2.77 \cdot 10^{-3}$	$9.22 \cdot 10^{-3}$
(185 ; 225]	$5.7 \cdot 10^{-2}$	$7.53 \cdot 10^{-1}$	$-2.75 \cdot 10^{-3}$	$-2.28 \cdot 10^{-2}$
(225 ; 295]	$1.54 \cdot 10^{-1}$	$7.97 \cdot 10^{-1}$	$-2.06 \cdot 10^{-4}$	$6.77 \cdot 10^{-3}$

Table A.44: Differences in unfolded distribution of photon virtuality obtained with standard and varied parameters after normalisation.

Q^2_{DA} [GeV^2]	$0.139 < y_{\mathrm{El}} < 0.611$	$0.061 < y_{\mathrm{El}} < 0.669$	$\sigma_E \times 1.02$	$\sigma_E \times 0.96$
(25 ; 50]	$-2.05 \cdot 10^{-1}$	$1.22 \cdot 10^{-1}$	$-4.02 \cdot 10^{-2}$	$-5.3 \cdot 10^{-2}$
(50 ; 65]	$-1.45 \cdot 10^{-1}$	$5.83 \cdot 10^{-2}$	$-3.9 \cdot 10^{-2}$	$-5.31 \cdot 10^{-3}$
(65 ; 105]	$-7.68 \cdot 10^{-2}$	$3.41 \cdot 10^{-2}$	$-3.27 \cdot 10^{-2}$	$-5.89 \cdot 10^{-3}$
(105 ; 145]	$-1.63 \cdot 10^{-2}$	$1.12 \cdot 10^{-2}$	$-2.39 \cdot 10^{-2}$	$-4.29 \cdot 10^{-3}$
(145 ; 185]	$-4.86 \cdot 10^{-2}$	$8.26 \cdot 10^{-4}$	$-2.19 \cdot 10^{-3}$	$3.8 \cdot 10^{-3}$
(185 ; 225]	$2.04 \cdot 10^{-2}$	$1.44 \cdot 10^{-2}$	$-3.48 \cdot 10^{-3}$	$5.57 \cdot 10^{-2}$
(225 ; 295]	$1.43 \cdot 10^{-2}$	$3.92 \cdot 10^{-2}$	$2.05 \cdot 10^{-2}$	$-1.15 \cdot 10^{-1}$

Table A.45: Differences in unfolded distribution of photon virtuality obtained with standard and varied parameters after normalisation.

Q^2_{DA} [GeV^2]	$X_{e'} + 2$ mm	$X_{e'} - 2$ mm	$Y_{e'} + 2$ mm	$Y_{e'} - 2$ mm
(25 ; 50]	$5.08 \cdot 10^{-2}$	$1.63 \cdot 10^{-2}$	$4.02 \cdot 10^{-2}$	$2.4 \cdot 10^{-2}$
(50 ; 65]	$-4.52 \cdot 10^{-2}$	$-1.53 \cdot 10^{-3}$	$-2.22 \cdot 10^{-2}$	$-3.72 \cdot 10^{-2}$
(65 ; 105]	$3.88 \cdot 10^{-3}$	$-6.76 \cdot 10^{-3}$	$6.53 \cdot 10^{-4}$	$3.95 \cdot 10^{-3}$
(105 ; 145]	$5.67 \cdot 10^{-3}$	$-1.92 \cdot 10^{-3}$	$-6.43 \cdot 10^{-3}$	$-4.43 \cdot 10^{-3}$
(145 ; 185]	$-1.81 \cdot 10^{-2}$	$1.33 \cdot 10^{-2}$	$2.69 \cdot 10^{-3}$	$2.3 \cdot 10^{-2}$
(185 ; 225]	$4.31 \cdot 10^{-2}$	$-1.55 \cdot 10^{-2}$	$2.33 \cdot 10^{-2}$	$1.42 \cdot 10^{-2}$
(225 ; 295]	$-6.88 \cdot 10^{-4}$	$1.04 \cdot 10^{-3}$	$8.82 \cdot 10^{-3}$	$-1.92 \cdot 10^{-2}$

Table A.46: Differences in unfolded distribution of photon virtuality obtained with standard and varied parameters after normalisation.

Q^2_{DA} [GeV^2]	$Z_{e'} + 2$ mm	$Z_{e'} - 2$ mm	$E \times 1.03$	$E \times 0.97$
(25 ; 50]	$-9.7 \cdot 10^{-3}$	$4.68 \cdot 10^{-2}$	$-3.8 \cdot 10^{-1}$	$-4.33 \cdot 10^{-2}$
(50 ; 65]	$9.54 \cdot 10^{-3}$	$-3.7 \cdot 10^{-2}$	$1.28 \cdot 10^{-1}$	$1.98 \cdot 10^{-1}$
(65 ; 105]	$-4.54 \cdot 10^{-3}$	$7.67 \cdot 10^{-3}$	$-5.49 \cdot 10^{-2}$	$5.15 \cdot 10^{-2}$
(105 ; 145]	$-4.97 \cdot 10^{-3}$	$2.63 \cdot 10^{-3}$	$-3.92 \cdot 10^{-2}$	$1.08 \cdot 10^{-1}$
(145 ; 185]	$1.15 \cdot 10^{-2}$	$6.89 \cdot 10^{-3}$	$-6.63 \cdot 10^{-2}$	$-3.71 \cdot 10^{-2}$
(185 ; 225]	$-4.16 \cdot 10^{-2}$	$5.29 \cdot 10^{-2}$	$2.14 \cdot 10^{-2}$	$1.36 \cdot 10^{-1}$
(225 ; 295]	$1.73 \cdot 10^{-2}$	$-8.76 \cdot 10^{-3}$	$5.2 \cdot 10^{-2}$	$-9.68 \cdot 10^{-2}$

A.4 Hadron Level Distributions

Table A.47: Hadron level distribution of jet azimuthal angle.

$\phi_{jet^{\text{had}}}$	$dn/d\phi_{jet^{\text{had}}}$	error
(0 ; 0.3927]	24.51	2.3
(0.3927 ; 0.7854]	11.35	1.71
(0.7854 ; 1.1781]	19.89	2
(1.1781 ; 1.5708]	23.21	1.87
(1.5708 ; 1.9635]	25.36	2.29
(1.9635 ; 2.3562]	23.03	2.13
(2.3562 ; 2.7489]	13.43	1.92
(2.7489 ; 3.1416]	19.34	2.21
(3.1416 ; 3.5343]	0	0

Table A.48: Hadron level distribution of photon virtuality.

Q^2 [GeV^2]	dn/dQ^2 [GeV^{-2}]	error
(50 ; 65]	$1.07 \cdot 10^{-2}$	$7.18 \cdot 10^{-4}$
(65 ; 105]	$2.64 \cdot 10^{-3}$	$9.79 \cdot 10^{-5}$
(105 ; 145]	$9.98 \cdot 10^{-4}$	$6.15 \cdot 10^{-5}$
(145 ; 185]	$4.6 \cdot 10^{-4}$	$4.74 \cdot 10^{-5}$
(185 ; 225]	$2.08 \cdot 10^{-4}$	$3.35 \cdot 10^{-5}$
(225 ; 295]	$3.88 \cdot 10^{-5}$	$8.49 \cdot 10^{-6}$
(295 ; 333.571]	0	0

A.5 Hadron Level Cross Sections

Table A.49: Hadron level cross section as a function of jet azimuthal angle.

$\phi_{jet^{\text{had}}}$	$d\sigma^{\text{had}}/d\phi_{jet^{\text{had}}}$ [pb]	error
(0 ; 0.3927]	24.51	2.3
(0.3927 ; 0.7854]	11.35	1.71
(0.7854 ; 1.1781]	19.89	2
(1.1781 ; 1.5708]	23.21	1.87
(1.5708 ; 1.9635]	25.36	2.29
(1.9635 ; 2.3562]	23.03	2.13
(2.3562 ; 2.7489]	13.43	1.92
(2.7489 ; 3.1416]	19.34	2.21
(3.1416 ; 3.5343]	0	0

Table A.50: Hadron level cross section as a function of virtuality.

Q^2 [GeV^2]	$d\sigma^{\text{had}}/dQ^2$ [pb/GeV^2]	error
(50 ; 65]	$1.07 \cdot 10^{-2}$	$7.18 \cdot 10^{-4}$
(65 ; 105]	$2.64 \cdot 10^{-3}$	$9.79 \cdot 10^{-5}$
(105 ; 145]	$9.98 \cdot 10^{-4}$	$6.15 \cdot 10^{-5}$
(145 ; 185]	$4.6 \cdot 10^{-4}$	$4.74 \cdot 10^{-5}$
(185 ; 225]	$2.08 \cdot 10^{-4}$	$3.35 \cdot 10^{-5}$
(225 ; 295]	$3.88 \cdot 10^{-5}$	$8.49 \cdot 10^{-6}$
(295 ; 333.571]	0	0

Appendix B

Nomenclature

B.1 General

a	italics denote numbers
$\mathbf{A} = (E_\mathbf{A}, p_{x,\mathbf{A}}, p_{y,\mathbf{A}}, p_{z,\mathbf{A}})$	bold symbols denote four-vectors with energy $E_\mathbf{A}$, x-momentum $p_{x,\mathbf{A}}$, y-momentum $p_{y,\mathbf{A}}$ and z-momentum $E_\mathbf{A}$
$p_{t,A} = \sqrt{p_{x,\mathbf{A}}^2 + p_{y,\mathbf{A}}^2}$	denotes transverse momentum of four-vector $\mathbf{A}$
$p_{l,A}$	denotes longitudinal momentum of four-vector $\mathbf{A}$; usually $p_{l,A} = p_{z,A}$
$\vec{\mathbf{A}} = (p_{x,\mathbf{A}}, p_{y,\mathbf{A}}, p_{z,\mathbf{A}})$	arrow over bold symbol denotes momentum component of four-vector
$\vec{\mathbf{A}}\vec{\mathbf{B}} = p_{x,\mathbf{A}}p_{x,\mathbf{B}} + p_{y,\mathbf{A}}p_{y,\mathbf{B}} + p_{z,\mathbf{A}}p_{z,\mathbf{B}}$	two momentum vectors next to each other denote scalar product
$\mathbf{AB} = E_\mathbf{A}E_\mathbf{B} - \vec{\mathbf{A}}\vec{\mathbf{B}}$	four-momentum product
$\vec{\mathbf{A}}^2 = p_{x,\mathbf{A}}^2 + p_{y,\mathbf{A}}^2 + p_{z,\mathbf{A}}^2$	square of momentum vector
$\mathbf{A}^2 = E_\mathbf{A}^2 - \vec{\mathbf{A}}^2$	square of four-momentum vector; usually interpreted as squared invariant mass
$\theta_\mathbf{A}$	polar angle of four-momentum $\mathbf{A}$
$\phi_\mathbf{A}$	azimuthal angle of four-momentum $\mathbf{A}$
$\vec{A} = (X_A, Y_A, Z_A)$	arrow over a particle symbol denotes vector of position in space of the particle with X_A, Y_A, Z_A being respective coordinates
$\lambda_\mathbf{A}$	Length of a Compton wave associated with four-momentum $\mathbf{A}$
$\mathcal{P}$	probability

B.2 Particles

p	incoming proton
p'	scattered proton
e	incoming lepton (electron or positron)
e'	scattered lepton (electron or positron)
γ^*	virtual photon
$\mathbb{P}$	pomeron
h	hadronic system
γ^{isr}	photon emitted by the incoming lepton before interaction (ISR)

γ^{fsr} photon emitted by the scattered lepton after interaction (FSR)

B.3 Four-momenta

$\mathbf{P}$	incoming proton four-momentum; usually: $\mathbf{P} = (E_p, 0, 0, E_p)$
$\mathbf{P}'$	scattered proton four-momentum
$\mathbf{k}$	incoming lepton (electron or positron) four-momentum; usually: $\mathbf{k} = (E_e, 0, 0, -E_e)$
$\mathbf{k}'$	scattered lepton (electron or positron) four-momentum
$\mathbf{q}$	virtual photon (γ^*) four-momentum
$\mathbf{H}$	hadronic system (h) four-momentum
$\mathbf{\Xi}$	incoming parton (ξ) four-momentum
$\mathbf{\Xi}'$	scattered parton (ξ') four-momentum
$\mathbf{q^{isr}}$	initial state radiation (γ^{isr}) four-momentum
$\mathbf{q^{fsr}}$	final state radiation (γ^{fsr}) four-momentum

B.4 Variables

$E_p = 920$ GeV	proton beam energy - energy of incoming proton (p)
$E_e = 27.6$ GeV	lepton beam energy - energy of incoming electron or positron (e)
$Q^2 := -\mathbf{q}^2$	virtuality - squared negative mass of virtual photon (γ^*)
$W := (\mathbf{P} + \mathbf{q})^2$	incoming proton (p) - virtual photon (γ^*) centre of mass energy
$t := (\mathbf{P} - \mathbf{P}')^2$	squared four-momentum transferred at proton vertex
$s := (\mathbf{P} + \mathbf{k})^2$	incoming proton (p) - incoming lepton (e) centre of mass energy
$x := \frac{Q^2}{2\mathbf{Pq}}$	Bjorken scaling variable; in massless parton approximation it can be interpreted as fraction of incoming proton (p) longitudinal momentum carried by struck parton (ξ); details see sec 2.1.1 on page 3
$y := \frac{\mathbf{Pq}}{\mathbf{Pk}}$	inelasticity - fraction of lepton energy taken by exchanged boson
d, d_{h}, d_{e}	angular separation i.e. angle between two vectors
a, a_{h}, a_{e}	cell islands combination probability
d_{ca}	distance of the closest approach between track associated with scattered lepton and calorimeter energy deposit
$\beta := \frac{Q^2}{2\mathbf{q}(\mathbf{P}-\mathbf{P}')}$	fraction of pomeron momentum carried by the interacting parton
$x_{\mathbb{P}} := \frac{\mathbf{q}(\mathbf{P}-\mathbf{P}')}{\mathbf{qP}}$	fraction of proton momentum carried by the pomeron
$M := \sqrt{\mathbf{H}^2}$	invariant mass of hadronic final state
$E_h = \sum_{i\in h} E_i$	hadronic system energy
$(p_{x,h}, p_{y,h}, p_{z,h}) = \sum_{i\in h} (p_{x,i}, p_{y,i}, p_{z,i})$	hadronic system momentum
N_{trk}	number of tracks associated with vertex
N_{EFO}	number of particles in hadronic final state
E_{had}	energy deposited in hadronic calorimeter
E_{tot}	total energy deposited in calorimeter
y_{cut}	jet algorithm resolution parameter see sec. 5.5 on page 41
N_{jets}	number of jets reconstructed in an event
θ_0	polar angle measured from the nominal interaction point

B.5 Constants

h	Planck constant $h = 6.626068\ 10^{34}$ m^{2}kg/s
α	fine-structure constant $\alpha = e^2/4\pi\hbar c \approx 1/137$
m_p	proton rest mass $m_p = 0.938$ GeV

B.6 Acronyms

BCAL	barrel calorimeter
BEMC	barrel electromagnetic calorimeter
BGF	boson gluon fusion
BHAC1	barrel hadronic calorimeter section 1
BHAC2	barrel hadronic calorimeter section 2
CTD	central tracking detector
CN	common ntuples
DA	double angle method
DAQ	Data Acquisition
DDIS	Diffractive Deep Inelastic Scattering
DIS	Deep Inelastic Scattering
DQM	Data Quality Monitoring
EFO	energy flow object
EMC	electromagnetic calorimeter
FC	fast clear
FCAL	forward calorimeter
FEMC	forward electromagnetic calorimeter
FHAC1	forward hadronic calorimeter section 1
FHAC2	forward hadronic calorimeter section 2
FLT	First Level Trigger
FSR	final state radiation
GFLT	Global First Level Trigger
GSLT	Global Second Level Trigger
GTLT	Global Third Level Trigger
HAC	Hadronic Calorimeter
ISR	Initial State Radiation
LRG	Large Rapidity Gap
MC	Monte Carlo
MVD	Microvertex Detector
NC	Neutral Current Interaction
PMT	Photomultiplier Tube
pQCD	Perturbative Quantum Chromodynamics
QCD	Quantum Chromodynamics
QED	Quantum Electrodynamics
QPM	Quark Parton Model
RCAL	rear calorimeter
REMC	rear electromagnetic calorimeter
RHAC	rear hadronic calorimeter
SLT	Second Level Trigger
TLT	Third Level Trigger

B.7 Miscellaneous

$q\overline{q}$	events with two parton system (quark-antiquark)
$q\overline{q}g$	events with three parton system (quark-antiquark-gluon)